

AD-A189 428

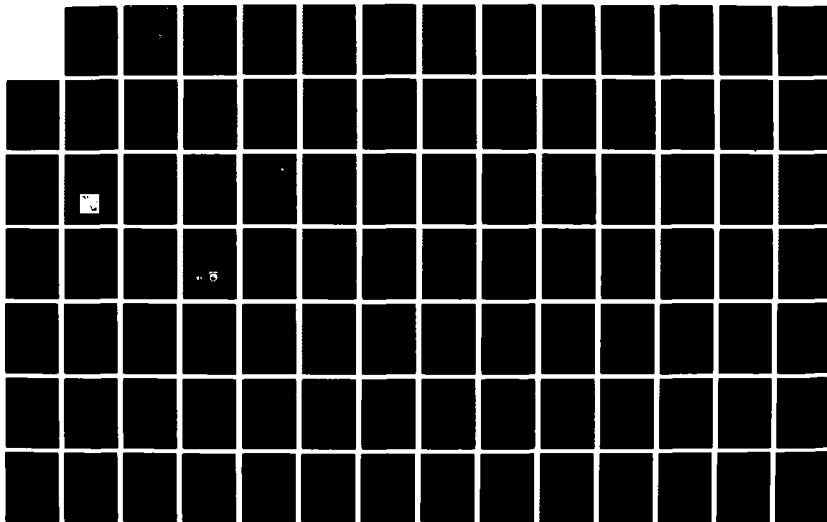
PHASE PRESERVATION CLEANUP IN A DOUBLE-PASS RAMAN
AMPLIFIER SRS (STIMULAT. (U) HUGHES RESEARCH LABS
MALIBU CA S M JENSEN ET AL. 10 DEC 87 HAC-REF-00031
N00014-85-C-0039

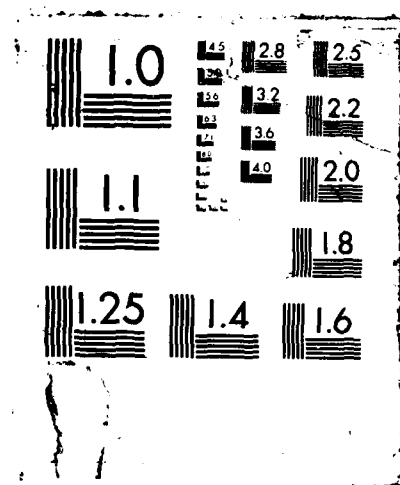
1/2

UNCLASSIFIED

F/G 9/3

NL





(2)

144

AD-A189 428

PHASE PRESERVATION CLEANUP IN A DOUBLE-PASS RAMAN AMPLIFIER SBS CONJUGATOR

S.M. Jensen, M.L. Minden, C.D. Jones, S.M. Wandzura, W.P. Brown, and R.C. Lind

Hughes Research Laboratories
3011 Malibu Canyon Road
Malibu, CA 90265

December 1987

Final Report

Contract N00014-85-C-0839

1 October 1985 - 31 May 1987

OFFICE OF NAVAL RESEARCH
800 N. Quincy Street
Arlington, VA 22217-5000

DTIC
ELECTE
DEC 29 1987
S **D**

DISTRIBUTION STATEMENT A
Approved for public release;
Distribution Unlimited

UNCLASSIFIED

SECURITY CLASSIFICATION OF THIS PAGE

A104428

REPORT DOCUMENTATION PAGE

Form Approved
OMB No. 0704-0188

1a. REPORT SECURITY CLASSIFICATION

Unclassified

1b. RESTRICTIVE MARKINGS

N/A

2a. SECURITY CLASSIFICATION AUTHORITY

N/A

3. DISTRIBUTION / AVAILABILITY OF REPORT

2b. DECLASSIFICATION / DOWNGRADING SCHEDULE

N/A

4. PERFORMING ORGANIZATION REPORT NUMBER(S)

5. MONITORING ORGANIZATION REPORT NUMBER(S)

6a. NAME OF PERFORMING ORGANIZATION

Hughes Research Laboratories

6b. OFFICE SYMBOL
(If applicable)

HRL

7a. NAME OF MONITORING ORGANIZATION

Office of Naval Research

6c. ADDRESS (City, State, and ZIP Code)

3011 Malibu Canyon Road
Malibu, CA 90265

7b. ADDRESS (City, State, and ZIP Code)

800 N. Quincy Street
Arlington, VA 222178a. NAME OF FUNDING / SPONSORING
ORGANIZATION

Office of Naval Research

8b. OFFICE SYMBOL
(If applicable)

ONR

9. PROCUREMENT INSTRUMENT IDENTIFICATION NUMBER

N00014-85-C-0839

8c. ADDRESS (City, State, and ZIP Code)

800 N. Quincy Street
Arlington, VA 22217

10. SOURCE OF FUNDING NUMBERS

PROGRAM
ELEMENT NO.PROJECT
NO.TASK
NO.WORK UNIT
ACCESSION NO.

11. TITLE (Include Security Classification)

Phase Preservation Cleanup in a Double-Pass Raman Amplifier SBS Conjugator (Uncl)

12. PERSONAL AUTHOR(S)

S.M. Jensen, R.C. Lind

13a. TYPE OF REPORT

Final

13b. TIME COVERED

FROM 10/85 TO 5/87

14. DATE OF REPORT (Year, Month, Day)

1987, December, 10

15. PAGE COUNT

127

16. SUPPLEMENTARY NOTATION

17. COSATI CODES

FIELD

GROUP

SUB-GROUP

18. SUBJECT TERMS (Continue on reverse if necessary and identify by block number)

Raman amplifiers, stimulated Brillouin scattering,
Phase conjugation, nonreciprocal aberrations,
High energy lasers

19. ABSTRACT (Continue on reverse if necessary and identify by block number)

This report describes a one-year program to investigate phase-preservation and cleanup in a double-pass Raman amplifier (RA) by a stimulated Brillouin scattering (SBS) conjugator. The goal of this program was to determine the physical processes that limit the compensation of RA phase aberration by SBS conjugators. Departures from this ideal performance are caused by nonreciprocal aberrations and/or imperfect performance of the SBS conjugator. The purpose of this work was to quantify the distortions caused by nonreciprocal aberrations in the RA process for uniform as well as distorted pump and seed waves.

20. DISTRIBUTION / AVAILABILITY OF ABSTRACT

☒ UNCLASSIFIED/UNLIMITED ☐ SAME AS RPT ☐ DTIC USERS

21. ABSTRACT SECURITY CLASSIFICATION

Unclassified

22a. NAME OF RESPONSIBLE INDIVIDUAL

22b. TELEPHONE (Include Area Code)

22c. OFFICE SYMBOL

TABLE OF CONTENTS

SECTION	PAGE
1 INTRODUCTION AND SUMMARY.....	1
2 THEORY OF PHASE CONJUGATION AND APPLICATION TO RAMAN AMPLIFIERS.....	7
2.1 Theory of Raman Amplifiers and SBS Phase Conjugation.....	7
2.2 Sources of Nonreciprocal Aberrations.....	11
2.3 Nonreciprocal Phase Error Discriminators....	17
3 NUMERICAL SIMULATIONS.....	19
3.1 The Computer Model.....	19
3.2 Goals of the Modeling Program/ Modeling Technique.....	28
3.3 Results.....	32
4 EXPERIMENTAL RESULTS.....	53
4.1 Goals of the Experimental Program.....	53
4.2 Data Reduction and Interpretation of Results.....	53
4.3 Multimode Laser Results.....	60
4.4 Single-Mode Laser Experiments.....	88
4.5 Experimental Results.....	94
5 SUMMARY AND RECOMMENDATIONS FOR FUTURE WORK.....	105
5.1 Comparison of Simulations with Single- Mode Laser Results.....	105
5.2 Recommendations for Future Work.....	108
REFERENCES.....	109
APPENDIX A.....	113
APPENDIX B.....	119

LIST OF ILLUSTRATIONS

FIGURE		PAGE
1	Common Elements for SBS Conjugation Scheme.....	1
2	The Stokes Scattering Process, in which an Input Pump Photon at Frequency ω_p Is Absorbed and a Stokes Photon at Frequency $\omega_s = \omega_p - \omega_\nu$ Is Emitted.....	7
3	Plot of the Index Perturbation around a Typical Gain Line.....	12
4	Four-Wave Mixing with Multi-Transverse Mode Pump and Stokes Waves.....	13
5	The Optical Configuration Used in the Simulation Code to Model the Characteristics of the Double-Pass RA/SBS Conjugator System.....	20
6	Pseudo-Color Plot of a Typical Phase Screen Used to Distort the Pump and Stokes Waves.....	21
7	Focal Plane Pattern with Uncompensated Aberrations for Several Values of the Convergence Parameter α	24
8	Near-Field Conjugation Fidelity Plotted as a Function of the Far-Field Strehl Ratio for an Assortment of Geometries.....	26
9	Far Field Energy-in-a-Bucket Measurement for a Typical Aberrated Beam for Conjugated and Unconjugated Geometries.....	27
10	The Effect of Phase Aberration on the Strehl Ratio of the Seed Beam.....	33
11	The Effect of Raman gain on the Strehl Ratio of the Seed Beam.....	34
12	The Effect of Varying the Injection Ratio on the Strehl Ratio of the Seed Beam as a Function of the Photon Conversion Efficiency....	35
13	Photon Conversion Efficiency for Flat-Top and Gaussian Beams.....	36



per 10/0

Availability Codes
1.000000
2.000000
3.000000
4.000000
5.000000
6.000000
7.000000
8.000000
9.000000
10.000000

A-1

LIST OF ILLUSTRATIONS (continued)

SECTION		PAGE
14	The Effects of Nonuniform Gain and Saturation for an Unaberrated Seed Beam, a Pump Beam Aberrated with $\Delta\phi_{RMS} = 3.8$ rad, and a Small-Signal Gain Parameter $g_{IL} = 8.0$	37
15	The Effect of Pump Aberration on the Strehl Ratio of the Seed Beam.....	38
16	The Effect of RIVED on the Strehl Ratio of the Seed Beam.....	39
17	The Effect of Nonlinear Dispersion on the Strehl Ratio of the Seed Beam.....	40
18	Schematic of the Laser Intensity Profiling System Used to Evaluate Near- and Far-Field Intensity Patterns.....	54
19	Contour Plot of a Typical Far-Field Beam Shape.....	56
20	Profile of the Beam Shown in Figure 19, Taken from a Cut through the Center of the Beam along a Horizontal Axis.....	56
21	Bullet Plot of the Profile Index for the Beams Analyzed during this Program.....	57
22	Schematic of the Experiment Used to Observe the Effect of Nonreciprocal Aberrations Using a Multimode Laser.....	61
23	Energy Contained in an SRS Generated Seed Pulse.....	64
24	Energy Contained in an SRS Generated Seed Pulse.....	65
25	Energy Contained in a BSRS Generated Seed Pulse.....	66
26	Energy Contained in the BSRS Generated Seed Pulse.....	67
27	Estimated Reflectivity of CH_4 SBS Cell at a Pressure of 2000 psi for Narrow Bandwidth (~ 7 GHz) Radiation at a Wavelength of 683 nm.....	70

LIST OF ILLUSTRATIONS (continued)

SECTION		PAGE
28	Pump Beam Radius as a Function of the Energy of the Pump Pulse.....	71
29	Pump Beam XDL as a Function of the Energy of the Pump Pulse.....	72
30	Pump Beam Strehl as a Function of the Energy of the Pump Pulse.....	73
31	Measured Gain in the RA as a Function of the Pump Energy.....	78
32	Seed Beam Radius as a Function of the Pump Energy.....	79
33	XDL of the Amplified Conjugated Seed Beam as a Function of the Pump Pulse Energy.....	80
34	Strehl Ratio of the Amplified-Conjugated Seed Beam as a Function of the Pump Energy.....	82
35	Measured Gain in the RA as a Function of Seed Energy Entering the Amplifier on the Second Pass.....	83
36	Seed Beam Radius as a Function of the Seed Energy.....	85
37	XDL of the Amplified-Conjugated Seed Beam as a Function of the Seed Pulse Energy.....	86
38	Strehl Ratio of the Amplified-Conjugated Seed Beam as a Function of the Seed Energy.....	87
39	Low Energy Nd:YAG Pump Laser Schematic.....	89
40	Single-Longitudinal, Single-Transverse Mode Oscillator.....	89
41	Temporal Pulse Shape of the Single Mode Pump Laser, the Horizontal Scale Is 10 nsec/div.....	90
42	Average Intensity vs Radial Position of the Single-Mode Pump Laser Near-Field.....	90

LIST OF ILLUSTRATIONS (continued)

SECTION		PAGE
43	Experiment Used to Demonstrate Nonreciprocal Aberrations Using the Single-Mode Laser.....	92
44	Temporal Pulse Shape of the Stokes Seed.....	93
45	Raman Gain as a Function of the Pump Energy and Beam Aberration Using the Single-Mode Laser System.....	96
46	Conjugate Beam Fidelity as a Function of Pump Energy for the Single-Mode RA/SBS System.....	98
47	Conjugate Beam Fidelity as a Function of Pump Energy for the Single-Mode RA/SBS System...	99
48	Raman Gain as a Function of the RA Cell Pressure Using the Single-Mode RA/SBS System....	100
49	Conjugate Beam Fidelity as a Function of Raman Cell Pressure for the Single-Mode RA/SBS System.....	102
50	Conjugate Beam Fidelity as a Function of RA Pressure for the Single-Mode RA/SBS System.....	103
51	Comparison of Simulated and Experimental Conjugate Beam Fidelity as a Function of RA Gain.....	106
52	Comparison of Experimental Results with the Simulation of RIVED.....	107

LIST OF TABLES

TABLE		PAGE
1	Characteristics of Multimode Pump Beam.....	74
2	Characteristics of Multimode Seed Beam.....	75
3	Characteristics of Aberrated/Unconjugated Multimode Seed Beam.....	76
4	Characteristics of Aberrated/Conjugated Multimode Seed Beam.....	77
5	Characteristics of Single-Mode Pump Beam.....	94
6	Characteristics of Single-Mode Seed Beam.....	95

SECTION 1

INTRODUCTION AND SUMMARY

This report describes the results of a one-year program to investigate phase-preservation and cleanup in a double-pass Raman amplifier (RA) by a stimulated Brillouin scattering (SBS) conjugator. High power RA systems are natural candidates for employing SBS conjugation. These amplifiers have inhomogeneities, mirror distortions, and other aberrations that can be readily compensated by a double-pass/conjugator system. Features of the SBS process are well-matched to high power excimer laser pulses. First, beam quality requirements are severe in these systems, and nonlinear phase conjugation has a demonstrated capability to correct large amplitude, small spatial scale aberrations. Second, some aberrations vary rapidly in time and SBS has a correction bandwidth greater than 100 MHz. Third, a system employing SBS for optical train and amplifier cleanup has low complexity. Fourth, the high threshold power of the SBS process is well-matched to the energy of high power excimer laser pulses.

Figure 1 shows the common elements of a double-pass RA/SBS conjugator system. In this figure a seed laser beam, incident from the left, passes through the RA. During this initial pass the seed beam picks up phase aberrations from the optics and inhomogeneities from the RA. The SBS conjugator produces a return wave with reversed phase aberrations (a phase conjugate

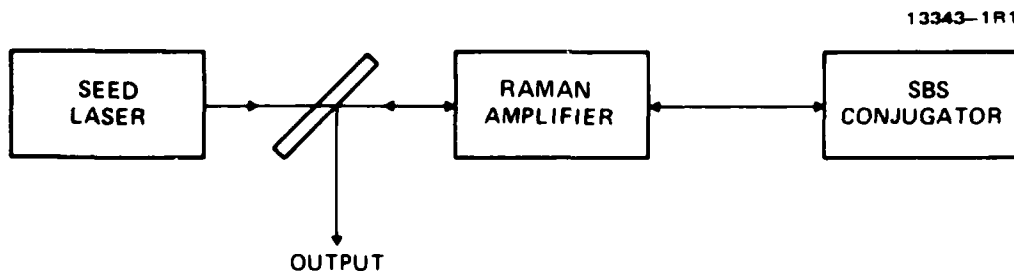


Figure 1. Common elements for SBS conjugation scheme.

reflection). On the return path, the aberrations in the amplifier are compensated for by the conjugate beam produced by the SBS conjugator. Ideally, the result is an amplified, unaberrated output beam.

Even though the SBS conjugator can produce a high quality conjugate wavefront, there are limitations on the compensation of the RA: (1) possible temporal limitations due to the finite response time of the SBS conjugation process (<10 ns), (2) spatial limitations due to diffraction and clipping in the RA, and (3) inability to compensate for aberrations that are different on the initial and return passes through the RA (nonreciprocal aberrations). (Long pulse issues characteristic of excimer systems were not investigated on this program.)

Fluctuations faster than 100 MHz appear unlikely in RA systems and were not investigated during this program. The limits on correction of small-scale fluctuations from diffraction and clipping have been extensively evaluated at Hughes Research Laboratories for both amplifiers and oscillators.^{1,2,3} From these studies we conclude that SBS provides excellent correction for aberrations whose rms phase is $<2\pi$ rad, provided that the Fresnel number (radius squared divided by length times wavelength) is >1 . In a well-designed system, aberrations from diffraction and clipping will be minimized; their effects were not reinvestigated during this program.

The goal of this program was to determine the physical processes that limit the compensation of RA phase aberration by SBS conjugators. If all RA aberrations are reciprocal and if the conjugation fidelity of the SBS process is sufficiently good, the wavefront of the amplified output should be very nearly the phase conjugate of the input reference. Departures from this ideal performance are caused by nonreciprocal aberrations and/or imperfect performance of the SBS conjugator. Nonreciprocal aberrations include direct nonreciprocal phase aberrations, as well as all amplitude aberrations due to nonuniform gain.

The purpose of this work was to quantify the distortions caused by nonreciprocal aberrations in the RA process for uniform and distorted pump and seed waves. Deleterious effects arise from poor replication of either the amplitude or phase of the input seed. Poor phase replication leads directly to phase errors in the output, while poor amplitude replication leads to phase errors only after propagation. It is the coupling of amplitude and phase aberration, by diffraction, that leads to the variety of possible effects. Nonuniform gain caused by pump aberration and pump saturation gives rise to a distorted amplitude profile. Because the gain in the RA is distributed, the effect depends on the scale size of the gain nonuniformity relative to diffraction (pump and/or seed). When the scale size of the gain nonuniformity is very large compared with diffraction (uniform gain), the RA/SBS system works very well. As the gain nonuniformity scale size decreases, its effect becomes much more important. In the limit of very short scale size, the output beam fidelity improves because diffraction tends to average over the gain nonuniformity.

A perfect conjugator system can compensate for phase aberrations that are reciprocal, such as thermal blooming and refraction by an inhomogeneous vibrational excitation density (RIVED). These aberrations are correctible if the resulting changes in refractive index occur slowly compared to the round trip transit time of the wavefronts. The conjugator can never be expected to compensate for nonreciprocal aberrations (i.e., aberrations such as gain saturation).

The concern addressed under this program was that nonreciprocal aberrations could impair the ability of the conjugator to compensate for the reciprocal aberrations. We examined this question by comparing beam fidelity in the presence of nonreciprocal aberrations with, and without, the addition of fixed reciprocal aberrations. Fixed reciprocal aberrations will always exist within the amplifier as a result of thermal effects and of

distortions in optical components. These aberrations, however, are difficult to quantify and are generally too small to produce measurable effects in our experiments. To produce large effects and to demonstrate the ability of the conjugator to compensate for large reciprocal aberrations, we included a fixed aberration plate in front of the amplifier. This plate is used to simulate atmospheric effects as well as aberrations in external optics and reciprocal aberrations in the amplifier.

To quantify the results of this study, we compare the beam quality of the aberrated system to an identical system where the aberrator is removed. This second unaberrated system measures the effect of the nonreciprocal phase errors; comparison with the aberrated system allows evaluation of the ability of the conjugator to compensate for the reciprocal errors.

The results of this program can be summarized as follows:

- Identified five sources of nonreciprocal aberrations in RA, namely, dispersion, transverse mode four-wave mixing (pump replication), longitudinal mode four-wave mixing, pump saturation, and RIVED.
- Estimated the conditions under which each effect can become important.
- Modified an existing propagation code to include the effects of nonreciprocal aberrations and used the code to model the RA/SBS conjugator system.
- Using the code, we found that the conjugator can compensate for reciprocal phase errors in almost all situations.
- A few situations were found where the aberrated system beam fidelity dropped by a factor of ~ 3 from that of the unaberrated system. In these cases, however, we were modeling such highly aberrated systems that the beam fidelities would have been ~ 3 orders of magnitude lower if the system had no conjugator.
- Experimental investigations were carried out using a hydrogen Raman amplifier and the second harmonic of a Nd:YAG laser as the pump beam. These experiments were carried out with both single-mode and highly multimode laser sources.

- Using both the multimode and single-mode laser sources we observed a steady decrease in conjugate beam fidelity with increasing pump energy. We believe this results from nonreciprocal aberrations due to nonuniform gain and pump saturation.
- Single-mode laser results were compared to estimates from the numerical simulation. The two results were found to be consistent.

This report consists of five sections. The first section provides a brief introduction and description of the program. Section 2 contains an analytical task aimed at determining the processes leading to nonreciprocal aberrations in RAs, their relative strengths, and the means to minimize their effects. Section 3 describes numerical modeling performed using a three-dimensional (3-D) wave optics simulation on the double-pass RA/SBS system. These results show the behavior of these systems under a variety of operating conditions, in addition to providing results for comparison with experiments. Experiments to demonstrate the nonreciprocal phase errors and to compare beam fidelities with the numerical model are described in Section 4. In Section 5, we compare the numerical and experimental results, draw conclusions, and indicate directions for future work.

SECTION 2

THEORY OF PHASE CONJUGATION AND APPLICATION TO RAMAN AMPLIFIERS

2.1 THEORY OF RAMAN AMPLIFIERS AND SBS PHASE CONJUGATION

Ordinary Raman scattering is a useful tool for studying the vibrational energy levels of molecules and optical-branch lattice vibrations in crystals. At high optical power, the scattering process becomes stimulated and a significant portion of the incident radiation can be scattered. Spectral analysis of the scattered radiation reveals the existence of frequencies that are shifted down from the incident frequency by amounts equal to the vibrational frequencies of the material being irradiated. This scattering process is referred to as "Stokes scattering." The scattering event is illustrated in Figure 2. In the figure, the molecule is initially in the ground state ($\nu = 0$). An incident photon at frequency ω_p is absorbed, and a Stokes photon is emitted at a lower frequency ω_s . The frequency mismatch $\omega_\nu = \omega_p - \omega_s$ is equal to the vibrational frequency of the molecule. To conserve energy, the molecule is transferred to an excited vibrational level ($\nu = 1$).

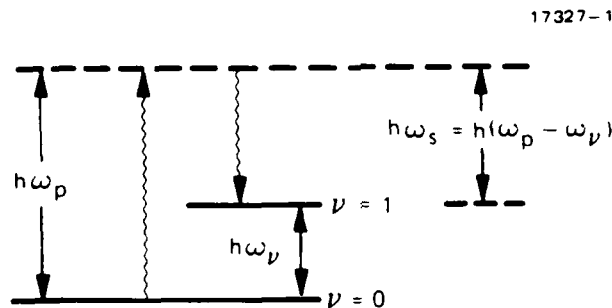


Figure 2. The Stokes scattering process, in which an input pump photon at frequency ω_p is absorbed and a Stokes photon at frequency $\omega_s = \omega_p - \omega_\nu$ is emitted. The excess energy is taken up by exciting the molecule to its first vibrational level ($\nu = 1$).

Our concern in this section is the process by which energy is transferred from pump photons to Stokes photons, and the way in which this process affects the fidelity of the Stokes (seed) wavefront. The effects of interest to this program can be described using the heuristic model of Raman scattering. In this model, the induced dipole moment of the molecule is given by:

$$\mu = \epsilon_0 \alpha E \quad , \quad (1)$$

where E is the applied electric field and α is the polarizability of the molecule. Clearly, the polarizability of the molecule depends on the intramolecular spacing and therefore will be modulated as the molecule vibrates. Assuming that a single vibrational mode of the molecule is important, the dipole moment can be expressed as

$$\mu = \epsilon_0 \left(\frac{\partial \alpha}{\partial Q} \right) Q E \quad , \quad (2)$$

where Q is the vibrational coordinate of the dominant mode. The equation of motion for the normal mode coordinate Q is

$$\frac{\partial^2 Q}{\partial t^2} = \frac{1}{2M_\nu} \epsilon_0 \left(\frac{\partial \alpha}{\partial Q} \right) E^2 - \gamma_\nu \frac{\partial Q}{\partial t} - \omega_\nu^2 Q \quad , \quad (3)$$

where M_ν is the effective mass of the vibrational mode, γ_ν is a phenomenological damping constant, and ω_ν is the normal oscillation frequency of the mode. E^2 in the equation above contains terms that oscillate at the sum and difference frequencies of the pump and Stokes waves. Only the difference frequency terms oscillate near the normal mode frequency and are able to drive the normal mode vibration. The amplitude of this vibration is given by:

$$Q_\nu = \frac{i\epsilon_0}{M_\nu \omega_\nu \gamma_\nu} \left(\frac{\partial \alpha}{\partial Q} \right) E_p E_s^* \quad , \quad (4)$$

where Q_ν , E_p , and E_s are the Fourier coefficients of the normal modes and the applied fields [i.e., $Q = Q_\nu \exp(-i\omega_\nu t) + Q_\nu^* \exp(i\omega_\nu t)$, etc.]. As discussed above, this vibrational mode drives the molecular polarizability which, as a result of the applied electric field, drives the induced dipole moment of the molecule. Using the result of Eqs. (2) and (4), we find dipole moments oscillating at both the Stokes and pump frequencies. This gives rise to a macroscopic polarization density at the Stokes frequency given by:

$$P_s = -i \frac{\rho \epsilon_0^2}{M_\nu \omega_\nu \gamma_\nu} \left(\frac{\partial \alpha}{\partial Q} \right)^2 E_p E_p^* E_s \quad (5)$$

This macroscopic polarization P_s drives the Stokes wave, giving rise to the optical gain in the Raman amplification process.

From Eq. (5) the following conclusions can be drawn:

- The Raman gain depends only on the pump intensity ($I \propto |E_p|^2$), and not its phase. It follows that pump phase aberration has no effect unless the effects of diffraction cause the phase aberration to manifest an intensity aberration.
- The Raman-driven polarization (P_s) has the spatial profile of the seed wave (i.e., $P_s \propto E_s$). Therefore, the amplified seed wave can be a high fidelity replication of the input seed wave if the pump profile is flat ($E_p E_p^*$).

In this manner, as is known, the Raman process can be made to transfer energy from an aberrated (phase) pump beam to an unaberrated seed beam.

This simple model predicts high fidelity amplification. In real systems, however, other effects must be taken into account. These include diffraction, pump depletion (gain saturation), saturation of the Raman medium, and dispersion. Diffraction leads to intensity aberrations on the pump beam and therefore to nonuniform gain, giving rise to a poorly replicated seed beam.

In regions where the seed beam is intense, the pump becomes more highly depleted, also giving rise to a nonuniform gain. This is especially important for high gain and conversion efficiency. In addition to gain saturation, the medium can be saturated, which occurs if a significant fraction of the molecules are left in their excited state ($\nu = 1$). Finally, dispersion effects from nonuniform gain and/or saturation of the medium can distort the amplified seed beam. In reality, all of these effects are present simultaneously, and it is their mutual interaction that distorts the amplified seed. The purpose of this program is to determine the important effects, the conditions under which they seriously degrade the amplified beam, and the extent to which phase conjugation can improve the output beam quality.

SBS production of a phase conjugate wave can be understood by considering three properties of SBS:

- SBS grows from noise.
- The total SBS gain is large ($>e^{25}$).
- The local gain coefficient in any thin layer of the medium is proportional to the pump intensity.

Starting at an infinitesimal layer at the back of the SBS cell, the noise radiation that matches the pump intensity undergoes the largest gain. Of course, this radiation is not phase conjugate to the pump and does not have a coherent phase front. However, if the SBS interaction length is long enough and if the decorrelation length of the pump intensity in the direction of propagation is small enough, this radiation diffracts as it propagates to a new infinitesimal layer closer to the entrance of the cell. At this layer, the amplified noise undergoes another amplification/filtration process. Only the portion of the noise with the proper phase front to diffract into the pump intensity profile in the next layer will be amplified. As this process continues through a large interaction length, the phase conjugate field has a gain coefficient approximately twice that of the nonconjugate component, dominating the nonconjugate component.

2.2 SOURCES OF NONRECIPROCAL ABERRATIONS

At least five sources of nonreciprocal aberrations exist in RA systems, including dispersion, four-wave mixing, pump replication, amplifier saturation, and self-focusing. These mechanisms depend on details of the pump, the Stokes seed, and the amplification geometry. While these mechanisms have been studied in past work, the ability of a double-pass conjugation system to compensate for their aberrations has not.

Dispersion in a RA is analogous to anomalous dispersion near a two-level gain or absorption line, and can lead to phase perturbations if the pump and Stokes are not tuned exactly to the Raman transition.^{4,5,6} If the pump intensity is uniform, the effect gives rise to a uniform shift of the seed phase and does not reduce the beam fidelity. A nonuniform pump beam introduces a nonuniform phase shift, giving rise to a direct phase aberration of the seed beam. This aberration occurs for multimode pump and Stokes seed, or a single-mode Stokes seed that is off-line center (because of incomplete compensation of the SBS shift). The magnitude of the effect can be evaluated from the Kramers-Kronig relationship, which shows that the gain and the refractive index are intimately related. As shown in Figure 3, the refractive index is decreased on the low frequency side of the gain and increased on the high frequency side. The phase aberration produced depends on the spatial nonuniformity of the Raman gain coefficient, which is proportional to the pump intensity. Because the pump and seed waves are crosspolarized on the first pass through the amplifier, little Raman gain is experienced, as based on a calculation⁷ of H_2 polarizability as a function of internuclear separation. From this, we estimate that the crosspolarized Raman gain is <0.1 of the copolarized gain. Hence, the nonlinear dispersion aberration is nonreciprocal, occurring only during the second pass through the amplifier. If, in addition, the Raman transition saturates, the phase shift from dispersion also saturates, depending on the pump intensity in a highly nonlinear manner.⁸

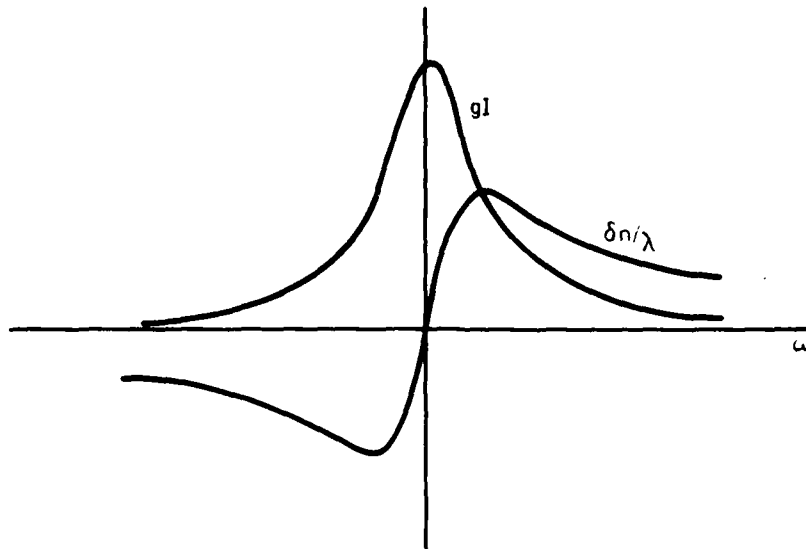


Figure 3. Plot of the index perturbation around a typical gain line.

The maximum index perturbation occurs where the gain has fallen off by a factor of 2. At this point, the index perturbation is $\sim (gIL)\lambda/2L$, where gIL is the peak small signal Raman gain coefficient. It follows that the maximum integrated phase error for propagation across the amplifier is $\sim \pi(gIL)$. At typical gains, several waves of phase shift could result; however, it is only the spatial nonuniformity of the phase shift (gain) that leads to aberration. In cases where this dispersion effect would be significant, the effect of the nonuniform gain on the intensity profile is much more severe, masking that from dispersion. Because of its nonreciprocal nature, this dispersion effect cannot be compensated by the phase conjugate mirror. The effect of this in the RA/SBS conjugator system is, however, not clear.

Four-wave mixing of multiple spatial (transverse) modes⁹ or multiple longitudinal modes¹⁰ can lead to nonreciprocal aberrations on the Stokes beam. Consider, first, four-wave mixing of spatial modes. This mixing process is generally described using the nonlinear susceptibility tensor $\chi^{(3)}$. The nonlinear polarization oscillating at the Stokes frequency is given by:

$$P_{s2}^{n1} = 6\chi^{(3)} E_{p1} E_{p2}^* E_{s1} \exp[(k_{p1} - k_{p2} + k_{s1} - k_{s2}) \cdot x] \quad , \quad (6)$$

where the subscripts s and p represent Stokes and pump, respectively. When a large number of spatial modes (off-axis k vectors) are present, phase matching of the pump and Stokes can occur in two ways: (1) A pump mode (E_{p1}) combines with its complex conjugate ($E_{p2}^* = E_{p1}^*$, $k_{p2} = k_{p1}$) and a Stokes mode to produce gain for that mode ($k_{s2} = k_{s1}$), as shown by the wave-vector diagram in Figure 4(a). When pump modes combine in this manner, no aberration is produced. (2) Two different pump modes ($E_{p2}^* \neq E_{p1}^*$, $k_{p2} \neq k_{p1}$) combine to generate an off-axis Stokes mode ($k_{s2} \neq k_{s1}$), as shown in Figure 4(b). With this latter occurrence, the one Stokes mode is mixed with another, giving rise to an aberration in the intensity and phase of the seed wave. From a simple analysis¹¹ that neglects depletion of the pump wave, transverse mode four-wave mixing is expected to significantly aberrate the Stokes wave if

$$2\pi(gIL)F \ll (XDL)^2 \ll e^{gIL} \quad , \quad (7)$$

12637-22R2

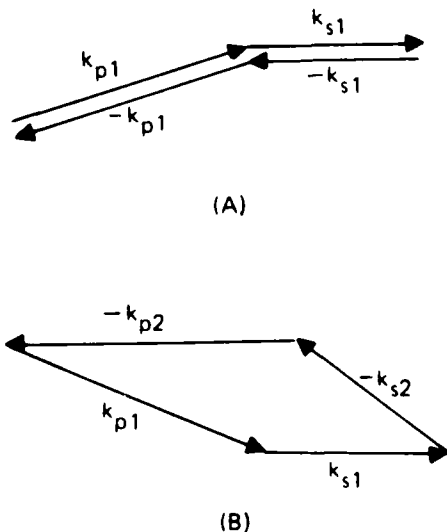


Figure 4. Four-wave mixing with multi-transverse mode pump and Stokes waves.

where g_{IL} is the small signal (log) gain in the RA, F is the Fresnel number of the pump beam ($F = D^2/4\lambda L$, with D the pump beam diameter, λ the wavelength, L the interaction length), and XDL is the times diffraction limited ($XDL \simeq D/a$, where a is the transverse coherence length, or $XDL \simeq D\Delta\theta/\lambda$, where $\Delta\theta$ is the beam divergence). The lower limit on XDL simply states that an unaberrated pump beam will not aberrate the Stokes wave. The upper limit expresses the fact that the inhomogeneities of a sufficiently aberrated pump beam will "average out."

If the pump and Stokes consist of a single spatial mode but multiple longitudinal modes, then the n^{th} pump and p^{th} Stokes modes can combine with the m^{th} pump mode to amplify the q^{th} Stokes mode. If the n^{th} and m^{th} pump modes have different phases, the phase difference $\Delta\phi_{nm} = \phi_n - \phi_m$ is transferred to the q^{th} Stokes mode and an aberration is produced. If the pump phase difference ($\Delta\phi_{nm}$) is spatially uniform, there is no reduction in beam fidelity. If, however, the phase difference depends on the transverse direction, an aberration is produced.^{12,13} It has been suggested that ϕ_n and ϕ_m are likely to be the same for multi-longitudinal mode radiation from excimer lasers¹⁴ and that therefore four-wave mixing of longitudinal modes may not be an important source of aberrations.

Pump replication is another name for transverse mode four-wave mixing, referring to a process by which the amplitude and phase of the Stokes field tend to replicate the pump amplitude and phase. Replication results because the Stokes gain is proportional to the pump amplitude, and hence the Stokes wave becomes intense in the same regions that the pump is intense. If this process is accompanied by diffraction, the pump amplitude and phase can be transferred to the Stokes wave.^{15,16,17} Pump replication for the forward stimulated scattering processes is analogous to phase conjugation in backward stimulated scattering. This means the gain coefficient for replication of the pump intensity and phase is about a factor of 2 larger than the gain

coefficient of a plane or image-bearing wave. This process is one of the ultimate limits on the injection level of a RA. For example, if the amplifier gain is 10^3 for the seed wave, the gain for noise (which matches the pump amplitude and phase) could approach 10^6 , and noise at levels of 10^{-3} of the seed competes with the seed.

While a double-pass phase conjugation system cannot compensate for pump replication, it can, in an alternative system, eliminate the problem. This objective can be accomplished by finding a means to introduce aberrators in the amplifier that affect only the Stokes wavelength, or that are highly dispersive so they affect the Stokes wave and the pump wave quite differently. The effect of these aberrators on the injected seed is completely compensated by the conjugator (assuming that the beams are not clipped by the system aperture). The pump and replication waves, however, remain uncompensated. It follows that the gain length for the replication mode is limited by the aberrator spacing rather than the amplifier length. Because the gain length appears in the exponent, small reductions in the gain length can lead to large reductions in the replication wave gain.

A related effect is pump saturation,¹⁸ which limits the gain in regions where most of the pump energy has already been converted to the Stokes wavelength. As a result, the amplitude profile of the Stokes wave tends to match the pump, rather than the amplitude of the seed wave. Subsequent propagation converts this amplitude aberration into a phase aberration. Pump saturation differs from pump replication because the pump energy is depleted, causing the Stokes and pump profiles to match at a single point within the amplifier. That is, the saturation effect is localized and cannot couple with diffraction to produce pump replication.

Refraction by an inhomogeneous vibrational excitation density (RIVED) refers to a process by which the Raman amplification process changes the Raman active medium. We consider here the

three ways the system is affected by promoting significant numbers of molecules to the excited vibrational state:

- Promotion of molecules to the excited state means that they are no longer available for the Raman process, leading to a saturation of the gain medium. If the saturation is nonuniform, the intensity of the amplified seed will be aberrated.
- Molecules in the excited vibrational state have a different polarizability from those in the ground state, leading to an index perturbation and therefore a phase aberration of the seed.
- The Raman process deposits significant vibrational energy into the medium. As this energy thermalizes, strong blooming and beam breakup can occur.

The latter two lead to phase aberrations that are generally reciprocal. Only in the short pulse regime, where transit time is important, will the effects be nonreciprocal.

Saturation of the gain medium is nonreciprocal and can lead to large intensity aberrations. In a hydrogen Raman cell with a gas density of 100 amagats, the molecular density is $\sim 10^{21} \text{ cm}^{-3}$. Assuming a typical interaction length of 100 cm, it would take $\sim 10^{23}$ photons/cm² to saturate the medium. This corresponds to roughly 10^5 J/cm^2 for visible radiation. Clearly, other damage mechanisms become important long before these levels are attained.

Other nonlinearities in the Raman cell can be important sources of nonreciprocal phase errors. These include self-focusing,^{19,20,21} higher order Stokes generation, and other self-induced aberrations of the seed beam. Self-focusing is the process by which an optical beam induces a change of refractive index in the surrounding media, altering its propagation characteristics. If the induced index change is positive, the beam "self-focuses." Because the seed beam is much more intense after amplification, the process is nonreciprocal. In gases, the dominate nonlinear mechanism for this effect is electrostriction.

For hydrogen at ~ 100 amagats, the critical power for self-focusing (self-trapping) is $\sim 1 \text{ MW/cm}^2$. Fortunately, the response time for the effect is limited to the transverse beam dimension divided by the phonon velocity, or about $5 \mu\text{s}$ for our experiments, and even longer in high Fresnel number excimer laser systems. Our experimental pulse lengths are less than 20 ns, and self-focusing should not be important. Higher order Stokes generation is only important for high intensity Stokes beams. In fact, it is only important for Stokes energies approaching or exceeding the pump energy (due to shorter interaction length in well-designed systems). Higher order Stokes generation can lead to a large nonlinear loss for the seed wave, depleting the seed where it is most intense. We do not, however, believe it could have been important in our experiments.

2.3 NONRECIPROCAL PHASE ERROR DISCRIMINATORS

It is the mutual interaction of diffraction and the effects mentioned above that gives rise to nonreciprocal aberrations and distortion of the seed beam. For example, pump replication requires that phase aberration and diffraction of the pump, spatially nonuniform gain, and intensity aberration and diffraction of the seed all occur simultaneously. Because of this mutual interaction, the identification of a single effect or process is difficult, if not impossible. In numerical simulations, the effects described above can be inserted independently; in this manner such processes as pump replication can be analyzed without competition from such other processes as pump depletion. In experimental investigations, the situation is much more complicated. The initial conditions (such as beam profile) cannot be arbitrarily set and the various material parameters cannot be arbitrarily adjusted. To identify the important effects and processes, we need to find the system dependence on the adjustable parameters. These include:

- Raman gain.
- Dispersion.
- RIVED.
- Pump intensity.
- Seed intensity.
- Injection ratio.
- Internal phase aberrators.
- External phase aberrators.
- Raman medium.
- Polarization.
- Temporal overlap.
- Compensation of SBS frequency shift.

The first three of these can be arbitrarily set only during numerical simulations. The effect of these parameters on the system performance will be discussed in the following sections.

SECTION 3

NUMERICAL SIMULATIONS

For this program, we modified an existing computer simulation of a RA/adaptive optics configuration in which the adaptive optics "look" through the RA. The techniques used in this modeling are described in detail in Appendix A. In this section of the report, we summarize the salient features of the modified program, indicate how we used it for these studies, and describe the results.

3.1 THE COMPUTER MODEL

Our computer model has been implemented for 3-D propagation; that is, there is the propagation direction and two dimensions transverse to the propagation direction. The code does not inherently include time-dependent phenomena. We have, however, simulated time-dependent phenomena, such as RIVED, in an approximate manner. The simulation solves the coupled nonlinear differential equations satisfied by the pump and first Stokes wave. A converging coordinate formulation that allows us to model both focused and collimated wave propagation is used in the simulation.

The optics configuration of our model is shown in Figure 5. It consists of a RA, a phase conjugate mirror, phase aberration screens, and the optical beams. The incoming Stokes seed is assumed to be uniform (flat top or truncated Gaussian, as discussed below). When this beam passes through the aberration screen, it acquires an aberrated phase, which, depending on the degree of aberration, can manifest an intensity aberration caused by diffraction. The phase screen is used to model possible atmospheric aberrations and, more importantly, to impose an adjustable reciprocal aberration on the seed wave. The seed wave is linearly propagated through the RA cell to the phase conjugate mirror. After conjugation or reflection, the Stokes seed

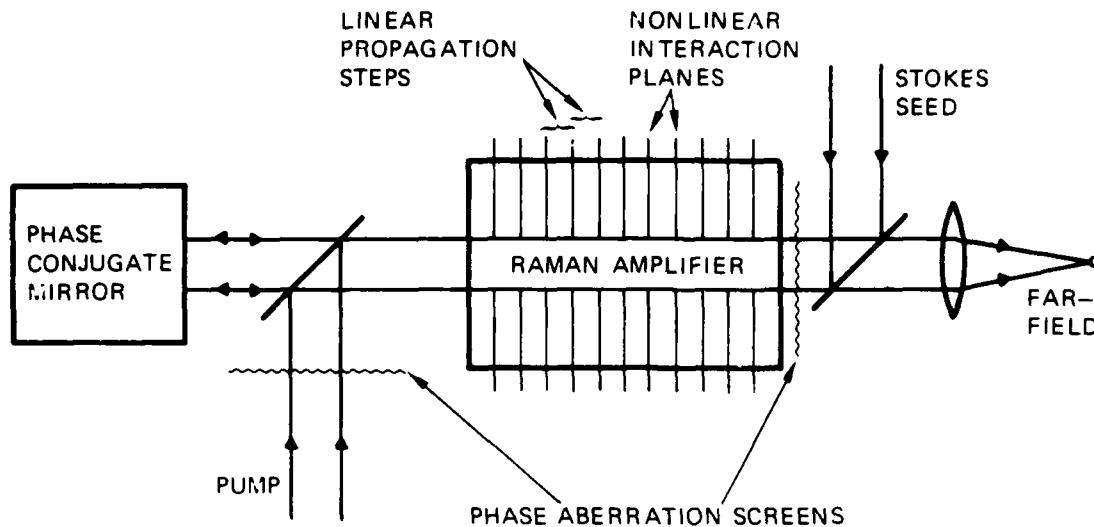


Figure 5. The optical configuration used in the simulation code to model the characteristics of the double-pass RA/SBS conjugator system.

retraces its path through the RA, this time undergoing gain (non-linear propagation) from the copropagating pump wave. After retraversing the phase aberration screen, the Stokes seed is examined in the far-field. The pump beam, incident from the bottom of the figure, passes through an independent aberration screen before entering the RA. Because of diffraction, the propagation distance between the pump aberrator and the RA allows intensity aberrations to develop on the pump. This development is important because the Raman gain process is automatically phase matched, and phase-only aberrations of the pump do not aberrate the seed wave.

The phase distortion plates are obtained by a discrete Fourier transform process. We use the fact that the Fourier transform of the square root of the power spectrum, multiplied by a delta-correlated random function, yields a distribution with the desired correlation properties. A 2-D array containing Gaussian random numbers (with zero mean and unit variance) is multiplied by a spatial frequency envelope described by a modified Von Karman spectrum of the form

$$\frac{0.367 \langle (\Delta\Phi)^2 \rangle^{1/2} L_0 / L_M}{[1 + (K_x^2 + K_y^2) / K_0^2]^{11/6}} \quad (8)$$

where K is the spatial frequency, $K_0 = 2\pi/L_0$, L_0 is the outer scale of the turbulence, and L_M is the width of the mesh. This gives a wave with the characteristics of atmospheric turbulence in the Kolmogorov model.²² We use an outer scale of twice the beam diameter. Figure 6 shows a typical phase aberration profile that is multiplied by the desired RMS phase error. For the pump wave, the phase screen is used with propagation to produce an intensity aberration before the RA. For the seed wave, the phase screen is used to simulate all reciprocal phase errors the seed beam encounters.

These errors include those originating from atmospheric turbulence and optics, as well as those arising from reciprocal aberrations within the Raman cell. More importantly, the seed phase screen is used to impose an adjustable reciprocal aberration to demonstrate the ability of the conjugator to compensate for reciprocal aberrations in the RA system.

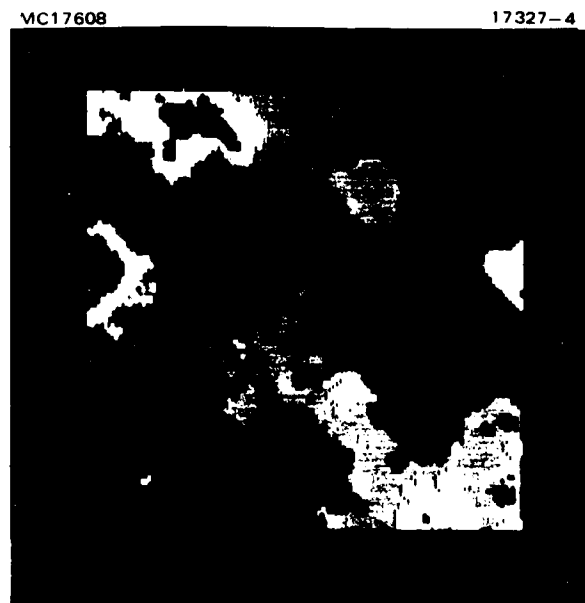


Figure 6. Pseudo-color plot of a typical phase screen used to distort the pump and Stokes waves.

Linear propagation is simulated by a solution of the propagation integral that uses either a Hermite-Gaussian transform or the discrete Fourier transform technique described in Appendix A. We found the Fourier transform technique to be more efficient when the beam is highly aberrated. Propagation is accompanied by a transformation that adjusts the size of the beam mesh so that the ratio of the beam size to the mesh size stays roughly constant as the beam diffracts. This transformation is normalized to the diffraction angle of a Gaussian beam. A convergence parameter α is chosen to increase the rate at which the mesh size changes to account for the larger diffraction angle of our distorted beams. Typically, a value of 2 (2X the Gaussian beam diffraction angle) is needed to allow a badly aberrated seed to reach the conjugator without clipping the mesh edge.

Analytically, a perfect conjugator is easy to implement; it is, however, not clear that the SBS process always yields perfect conjugation. For the purposes of this analysis, we assumed the conjugator operated in one of three modes:

- Perfect phase and amplitude conjugator.
- Phase-only conjugator (reflected profile is flat-top).
- An ordinary mirror.

By comparison of the beam quality with the conjugator operating in the different modes, the effect of the conjugator can be clearly demonstrated. Simulations of a phase-only conjugator were found to provide useful insight into the RA/SBS system and were a good complement to the simulation of a mirror that reflects the correct amplitude but the wrong phase. This condition could be representative of conjugation by stimulated scattering under certain conditions.²³

Nonlinear propagation is accomplished by slicing the medium into a number of subregions. The nonlinear interaction between the beams is calculated at the surface of each subregion and its

effects are incorporated into the beams prior to linear propagation across the subregion. The accuracy of this process depends on taking an adequate number of subregions; we typically used 60. The nonlinear interaction takes the form

$$\frac{\partial u_s}{\partial z} + \frac{1}{2ik_s} \nabla^2 u_s - \frac{\gamma}{2} |u_p|^2 u_s = 0 \quad (9)$$

$$\frac{\partial u_p}{\partial z} + \frac{1}{2ik_p} \nabla^2 u_p + \frac{\gamma^* k_p}{2 k_s} |u_s|^2 u_p = 0 \quad , \quad (10)$$

where u represents the complex field, k the propagation constant, subscripts p and s the pump and Stokes waves, and $\gamma = \gamma_0(1+i\beta)$ the complex loss. The dispersion factor β is included to model nonreciprocal dispersion effects, such as when the seed frequency is off line-center of the Raman gain curve.

As discussed above, a convergence parameter α is needed to account for diffractive size changes of the beams. A value of 2 was found necessary to give adequate beam containment within the Raman cell. This convergence parameter, however, is not sufficiently large to model the far-field, as is demonstrated on the right side of Figure 7. As seen in the figure, increasing the convergence parameter to $\alpha = 8$ gives suitable far-field patterns. This value of 8, however, is not suitable for accurate representation of the field within the amplifier. Incorporation into the code of a different convergence transformation, for the amplifier and the far field was not possible within the time span of this program. As a result, we have to utilize beam quality measurements that do not require knowledge of the full extent of the beam in the far-field. The Strehl ratio is one such quantity; it only requires an accurate calculation of the peak field in the far-field.

The propagation code gives the intensity and phase of the seed and pump at any point. The magnitude or phase of the complex mesh point values are output as a grayscale or translated into pseudo-color plots. Several beam quality parameters are

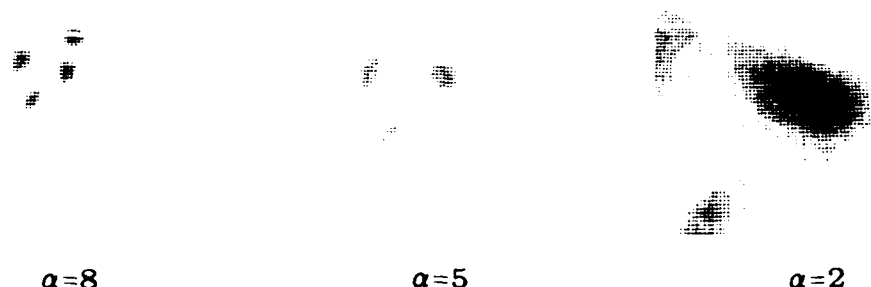


Figure 7. Focal plane pattern with uncompensated aberrations for several values of the convergence parameter α . In this example, the seed wave is a 0.5-cm flat-top beam aberrated by a $\Delta\phi_{RMS} = 1.1$ radian phase aberrator, without Raman amplification or conjugation.

derived from these mesh point values. Photon conversion efficiency is calculated by integrating the intensity of the seed at the end of the Raman cell and comparing it to the integrated input pump intensity. The near-field beam quality is evaluated using the phase-conjugate fidelity:

$$\frac{|\int dx dy u_i u_f|^2}{\int dx dy |u_i|^2 \int dx dy |u_f|^2}, \quad (11)$$

where u_i and u_f are the initial (prior to the phase aberration plate) and final (after conjugation, gain, and passing the aberration plate a second time) seed (Stokes) waves, respectively. The Strehl ratio is calculated from the peak far-field intensity pattern and is equal to the ratio of the observed peak intensity and the peak intensity obtained in the absence of aberrations (normalized to the beam energy).

A comparison of the conjugation fidelity with the Strehl ratio for an assortment of geometries is shown in Figure 8. As seen in the figure, the two measures of beam quality are nearly identical. In no case did we find that the two measures gave dramatically different results; for this reason, we only quote Strehl ratios in this section. For a number of cases, we also calculated the far-field beam size using the energy-in-a-bucket calculation. A representative example is shown in Figure 9. Using the radius that contains a fixed percentage (84% for flat top and 86% for Gaussian) divided by the diffraction-limited radius gives the XDL (times-diffraction-limited) of the beam. These measurements were also well-correlated with the Strehl ratio. That is, the Strehl ratio is the inverse of the XDL squared. Once again, we quote only the Strehl ratios in this section.

As described above, our nonlinear propagation code includes many effects. The majority of these effects occur because of the coupling of some nonlinear phenomena (e.g., saturation) with diffraction in the presence of aberrations. Diffractive effects are modeled within the RA as well as outside it. It follows that a great number of effects are automatically included in the code. The inclusion of Raman gain and conservation of energy allows the observation of pump replication and gain saturation. Nonlinear dispersion was included by allowing a complex gain coefficient. This accounts for cases where the SBS frequency shift is not fully compensated. The inclusion of nonlinear dispersion causes large- and small-scale inhomogeneities in the phase of the seed beam. Large-scale inhomogeneity results in focusing (or defocusing) of the seed beam, while small-scale inhomogeneities result in beam breakup. The effects of RIVED were also included as discussed below. By suitable choice of the degree of aberration, beam geometry, gain, etc., we were able to observe the ability of the RA/SBS system to compensate for the reciprocal phase errors in the presence of the nonreciprocal phase errors discussed above.

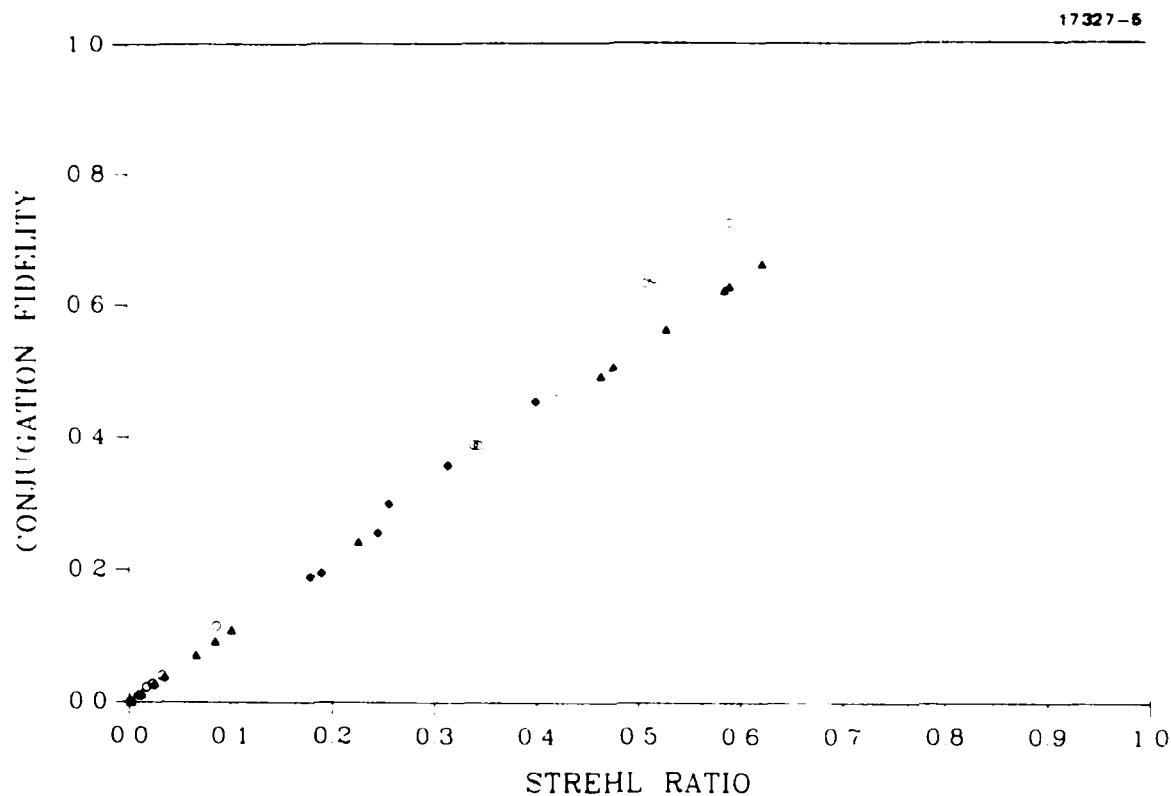


Figure 8. Near-field conjugation fidelity plotted as a function of the far-field Strehl ratio for an assortment of geometries. The linear relationship between the two indicates the correlation of these two measurements.

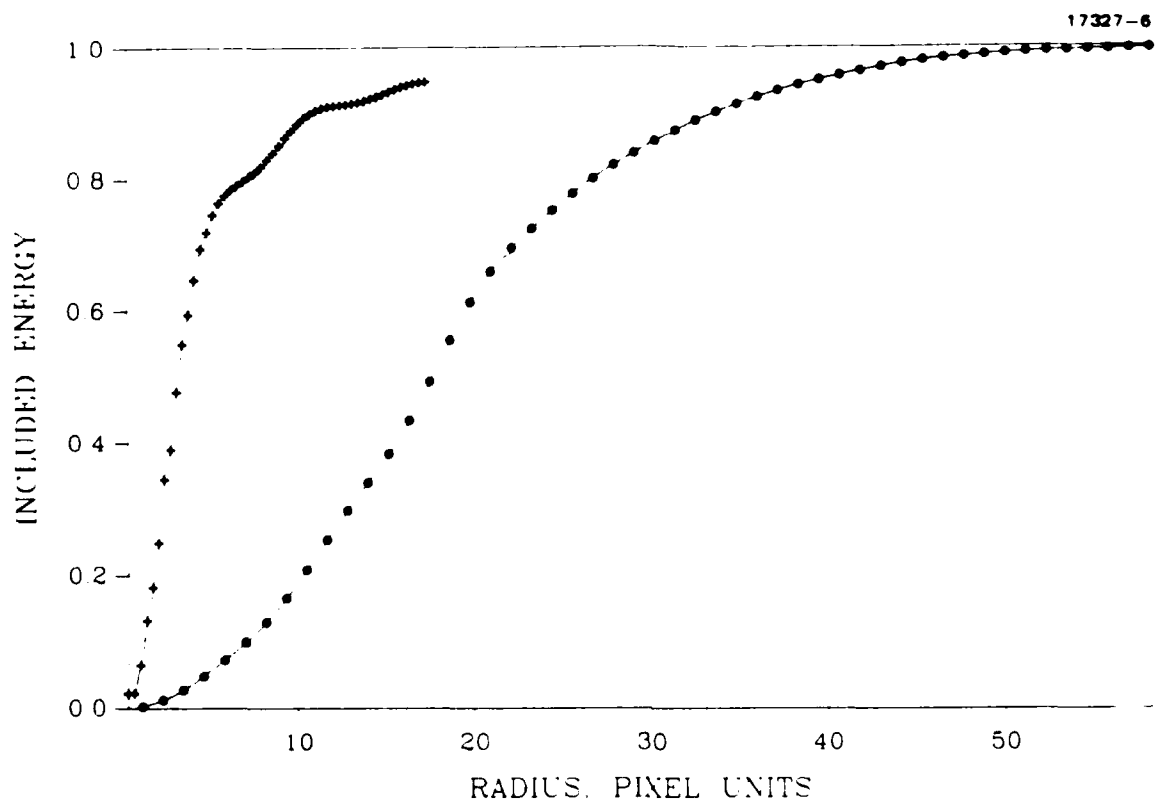


Figure 9. Far field energy-in-a-bucket measurement for a typical aberrated beam for conjugated and unconjugated geometries.

Several additional effects could have been incorporated in the code if time had permitted. These effects include: time-dependent pulses, very high Fresnel number geometries, higher order Stokes waves, and broad laser linewidth or multiple longitudinal modes. These effects were not included because they required a considerable increase in the execution time, and the expense was not judged worthy. Currently, each data point requires an execution time of about 9 min on the DEC VAX 8650, or about 10 s on the CRAY. The inclusion of time-dependent phenomena would require us to store the values in each subregion of the RA; this amounts to a large increase in memory requirements (~60X). High Fresnel number geometries would require a much larger mesh grid, smaller subregion thickness, and increased complexity of the propagation transformations. Higher order Stokes waves would increase the complexity in proportion to the number of orders, and were judged to be not important in the cases we studied. Finally, broad linewidths or multiple longitudinal modes would also increase the complexity in proportion to the number of modes, and were judged not worthy of the additional cost.

3.2 GOALS OF THE MODELING PROGRAM/MODELING TECHNIQUE

The goal of the modeling effort was to determine which physical processes limit compensation of RAs and under what conditions they do so. If all of the aberrations were reciprocal and if the conjugation fidelity of the SBS process were sufficiently good, then the wavefront of the amplified field should be very nearly the phase conjugate of the input reference. Departures from this ideal performance are caused by nonreciprocal aberrations and imperfect performance of the SBS conjugator. The purpose of this modeling effort was to quantify the amount of distortion caused by nonreciprocal aberrations for uniform as well as distorted pump and seed waves.

We looked for processes that deteriorate the beam quality. These processes arise from imperfect phase conjugation, the effects of nonlinear gain, diffraction, and the mutual interaction of these phenomena. Deleterious effects from the conjugator can arise from poor replication of either the amplitude or phase of the input seed. The effects of nonuniform gain, caused by distortions in the pump and saturation, also give rise to a distorted output. Because the gain in the RA is distributed, the effect of nonuniform gain depends on the scale size of the nonlinearities, relative to the amount of diffraction (pump and/or the seed). When the scale size of the gain nonuniformity is very large (uniform gain), the RA/SBS system works very well. As the scale size decreases, the effect of nonuniform gain can dramatically affect the fidelity of the output. In the limit of very short scale size, the fidelity improves due to averaging over gain nonuniformities. It was found that the conjugator can compensate for reciprocal phase errors in almost all cases.

The advantage of utilizing a computer model to investigate the behavior of the amplifier/conjugator system is that the various nonreciprocal aberrations can be independently introduced. In this fashion, the deleterious effects of each can be independently evaluated. It was not possible, nor desirable, to evaluate all combinations of effects within this program.

A perfect conjugator can compensate for phase aberrations that are the same on both the forward and backward passes (reciprocal) through the RA. The conjugator can not be expected to compensate for aberrations that are not the same (nonreciprocal). Our concern is that nonlinear gain and nonreciprocal aberrations could impair the ability of the conjugator to compensate for reciprocal aberrations. The modeling part of this study has been directed towards either strengthening or rejecting this concern.

We chose to quantify these results by asking the following questions: Under what conditions are strong nonlinear effects expected to arise? Under these conditions, How does the beam

quality of a Stokes wave derived from an aberrated seed and reflected from a conjugate mirror compare to the beam quality of a Stokes wave derived from a clean seed and reflected from an ordinary mirror? The beam quality, calculated from the far-field Strehl ratio or the near-field conjugation fidelity, will be poor in either case if the nonreciprocal errors are strong. However, a comparison of the aberrated-conjugated wave with the unaberrated wave highlights the way in which the compensation for reciprocal errors is jeopardized by the Raman amplification process.

As described above, the nonlinear propagation code allows variation of a number of parameters, including:

- Pump wavelength
- Stokes wavelength
- Beam diameters
- Raman cell length
- Small-signal gain parameter (g_{IL})
- Initial seed-to-pump amplitude ratio (seed intensity)
- RMS phase error of aberration plates
- Outer scale length of aberration plates
- Choice of amplitude profile for pump and seed beams
- Choice of conjugator:
 - perfect phase and amplitude conjugator
 - phase-only conjugator
 - mirror reflector.

Because of the large number of parameters, it was impossible to investigate all possible values within the scope of this program. In fact, not all combinations of parameters are interesting. In order to make the modeling effort tractable, we attempted to limit our investigation to combinations of parameters that provide useful insight into the operation of the RA/SBS system. We chose four standard beam profiles for modeling purposes:

- (1) 3.0-cm-diameter flat-top beam.
- (2) 0.5-cm-diameter flat-top beam.
- (3) Gaussian beam, truncated at 0.75-cm-diameter.
- (4) Gaussian beam, truncated at 0.35-cm-diameter.

The $1/e$ radius of the Gaussian intensity profile is set to $2/3$ of the truncation radius. For beam profiles (1) and (2), the injected seed intensity was 10^{-4} of the pump intensity; for beam profile (3) it was 10^{-2} of the pump intensity, and for profile (4) it was 0.16 of the pump intensity. Raman cell length was held at 100 cm. Beam profile (1) corresponds to a Fresnel number ($a^2/L\lambda$) of ~ 350 and represents the largest Fresnel number that can be comfortably handled by the code. High Fresnel numbers are commonly encountered in high energy applications where optical damage thresholds place a lower limit on beam size. Larger Fresnel numbers require a large increase in calculation time, as discussed above. The Fresnel number of beam profile (2) is ~ 9.1 and is the lowest Fresnel number discussed in this section. Beam profile (3) has an intermediate Fresnel number (~ 21). In addition, this beam is a truncated Gaussian, resulting in a decreased far-field diffraction angle and increased effects from nonuniform intensity profiles. Finally, profile (4), with a Fresnel number of ~ 4.5 , closely corresponds to our experiments using a frequency-doubled single-mode Nd:YAG laser.

After choosing the beam geometries discussed above, it was also necessary to determine how to incorporate the nonlinear effects. The difficulty here was to discriminate between the individual effects. To gain insight into the nonlinear effects, we utilized the following sequence:

- (a) Seed aberration, diffraction and conjugation.
- (b) Add the effects of Raman gain to case (a).
- (c) Add the effects of pump aberration to case (b).
- (d) Add the effects of RIVED to case (c).
- (e) Add the effects of nonlinear dispersion to case (b).

We found this sequence provided insight into the ability of the conjugator to compensate for reciprocal phase errors under increasingly difficult situations. The results of this investigation are discussed in detail in the following subsection.

3.3 RESULTS

The results of this analysis are summarized below with reference to Figures 10 to 17. Simulations of our experimental program are reviewed in Section 5. Our results generally consist of the Strehl ratio shown by curves representing the three experimental conditions: first, an unaberrated seed beam and a simple reflection rather than phase conjugation; second, a highly aberrated seed and a perfect phase and amplitude conjugator; third, a highly aberrated seed and a phase only conjugator (the conjugate amplitude is a flat-top). The Strehl ratio in these three conditions is plotted as we add in nonlinear and nonreciprocal effects. By comparing the unaberrated results with the aberrated-conjugated results, we will be able to identify those conditions under which the conjugator is unable to compensate for reciprocal phase errors in the presence of nonreciprocal effects. Comparison of the perfect conjugation results with the phase-only conjugation results indicates the importance of high fidelity replication of the intensity profile during conjugation. That is, some of the nonreciprocal effects, such as gain saturation, alter the intensity profile in a manner equivalent to the phase-only conjugation.

To begin this analysis, we first examine the effects of seed aberration - that is, reciprocal phase errors. In Figure 10, three sets of data are presented; these correspond to intensity profiles (1), (2), and (3) discussed above. In the upper left quadrant of the figure, the high Fresnel number (350), 3.0 cm flat-top beam results are given. The upper right quadrant contains the results for the low Fresnel number (9.1) flat-top beam. The lower left hand quadrant gives the results for the medium

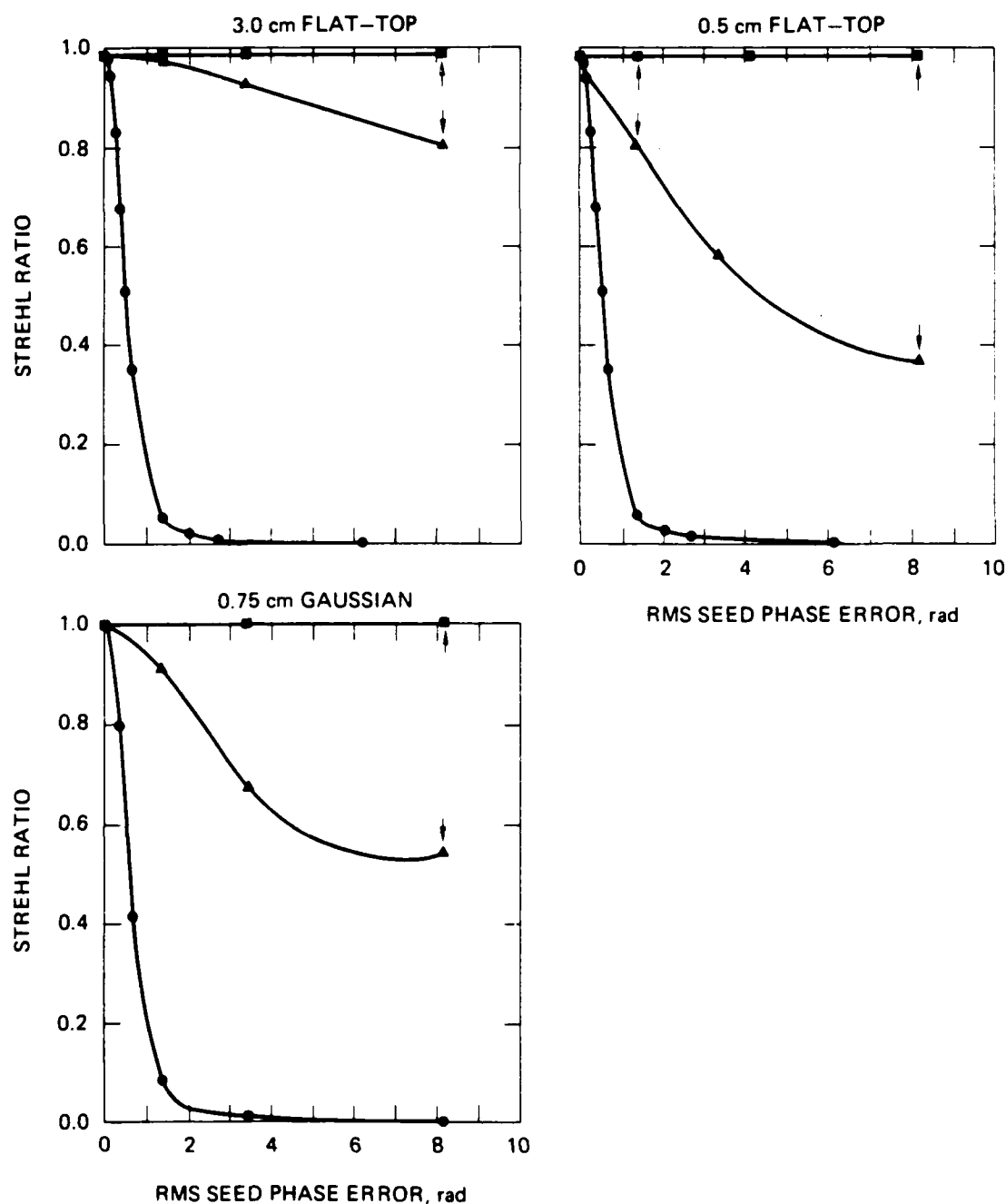


Figure 10. The effect of phase aberration on the Strehl ratio of the seed beam. In each quadrant the top curve is for an aberrated-conjugated beam geometry, the central curve for the aberrated-phase-only-conjugated geometry, and the lowest curve for an aberrated-unconjugated geometry.

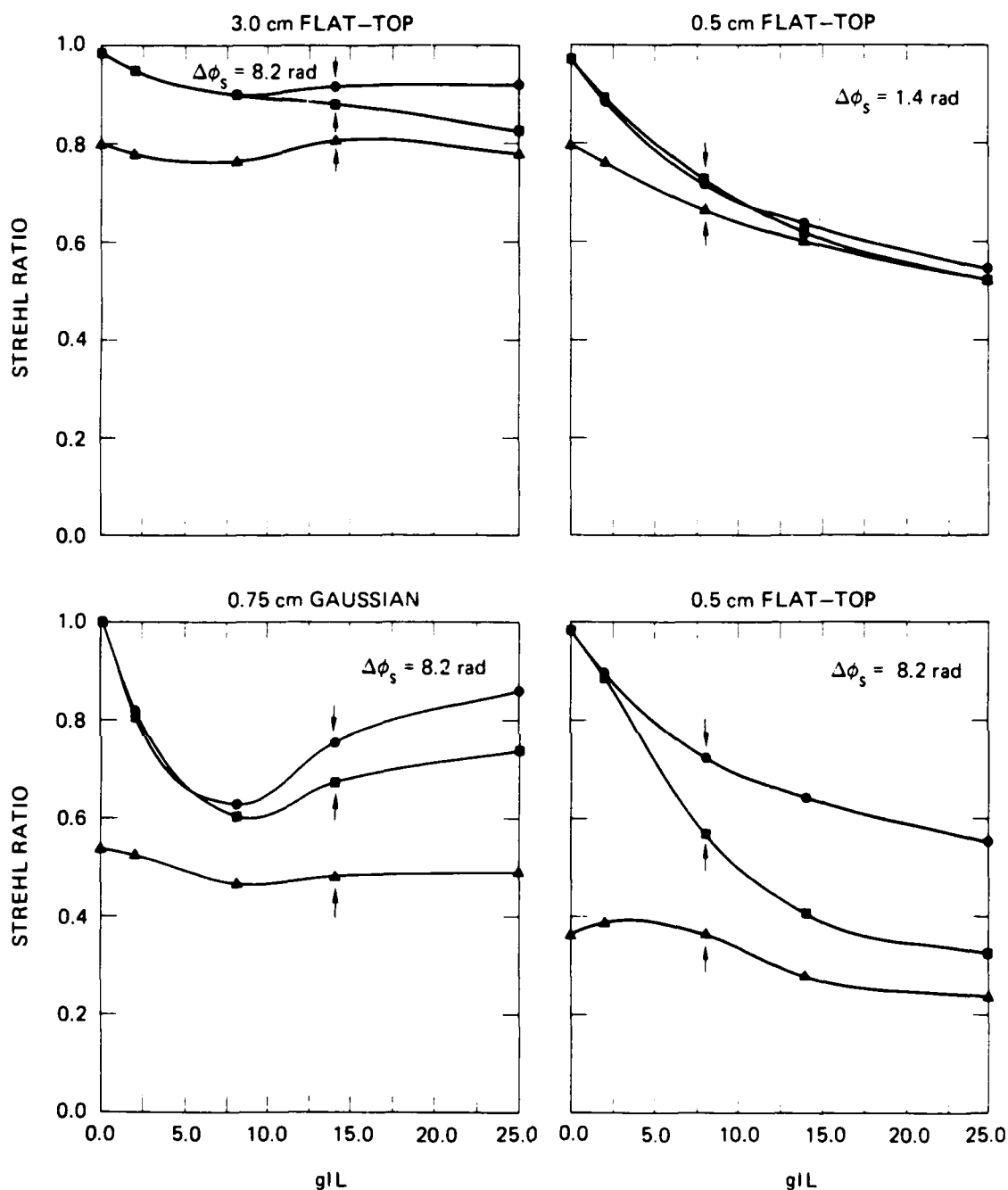


Figure 11. The effect of Raman gain on the Strehl ratio of the seed beam. In each quadrant the top curve is for an unaberrated beam geometry, the central curve is for the aberrated-conjugated geometry and the lowest curve for the aberrated-phase-only-conjugated geometry.

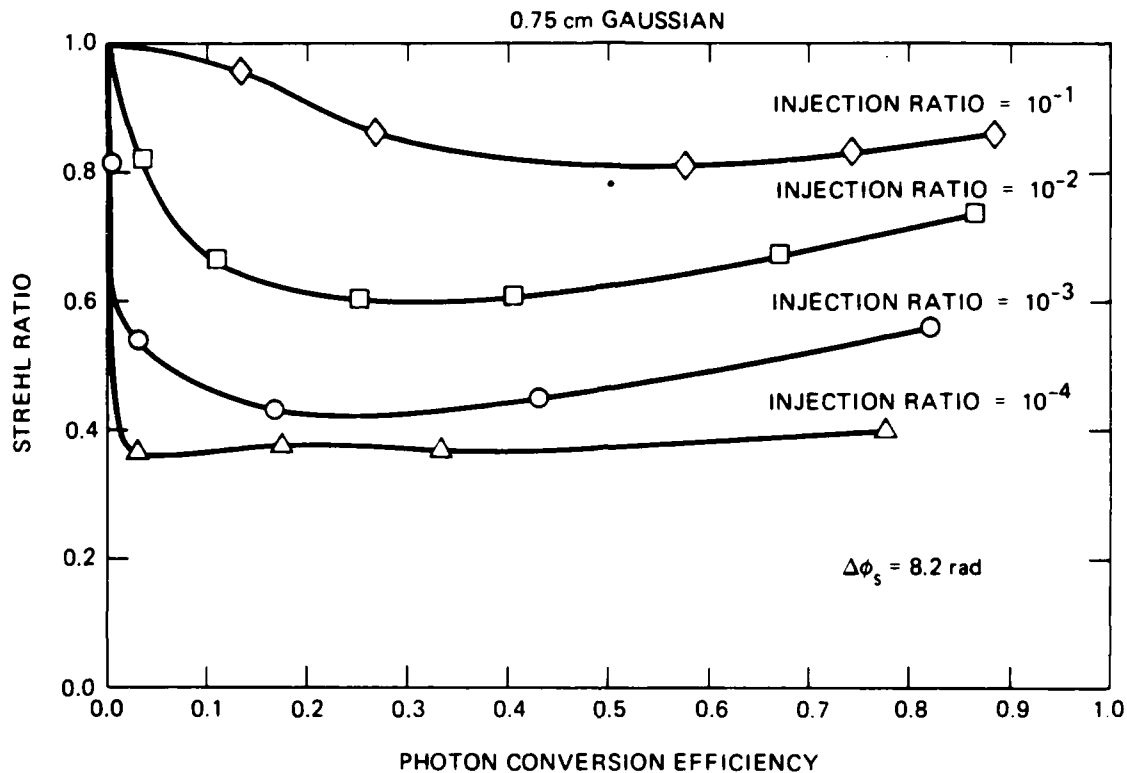


Figure 12. The effect of varying the injection ratio on the Strehl ratio of the seed beam as a function of the photon conversion efficiency. In this example, 0.75-cm-diameter truncated Gaussian beams are used with an RMS seed phase aberration of 8.2 rad and no pump aberration.

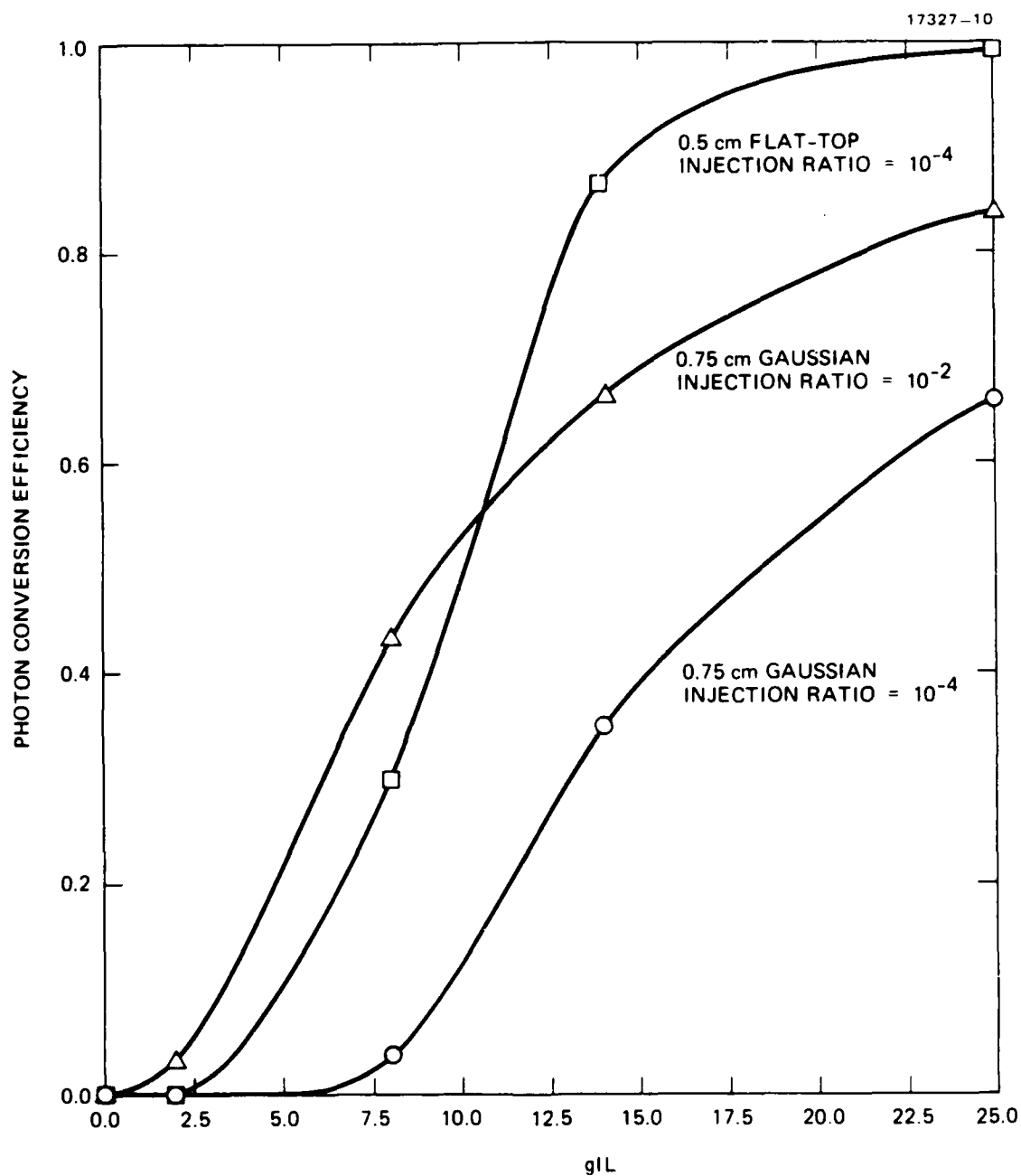


Figure 13. Photon conversion efficiency for flat-top and Gaussian beams.

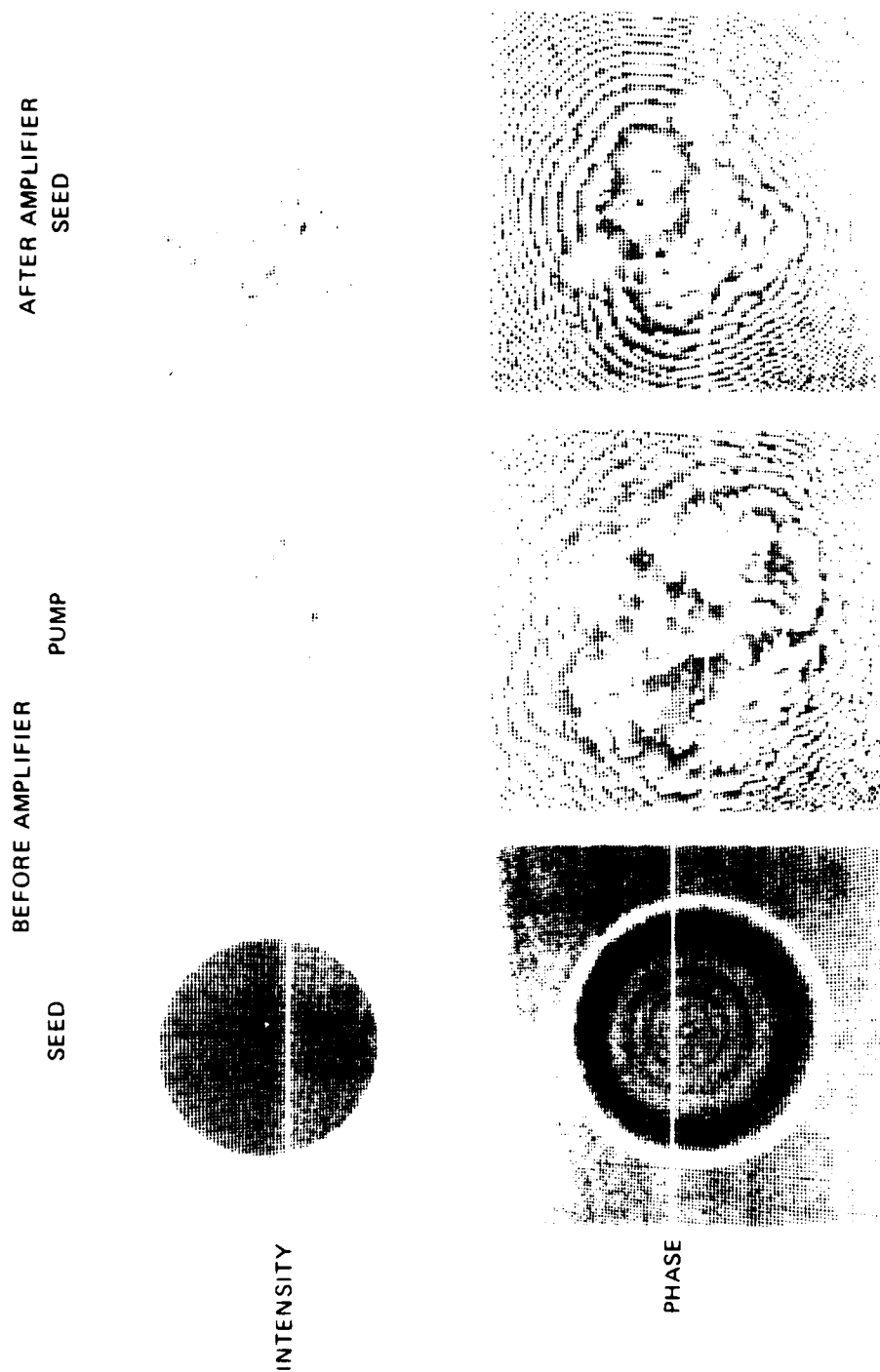


Figure 14. The effects of nonuniform gain and saturation for an unaberrated seed beam, a pump beam aberrated with $\Delta\phi_{\text{RMS}} = 3.8$ rad, and a small-signal gain parameter $g_{\text{IL}} = 8.0$.

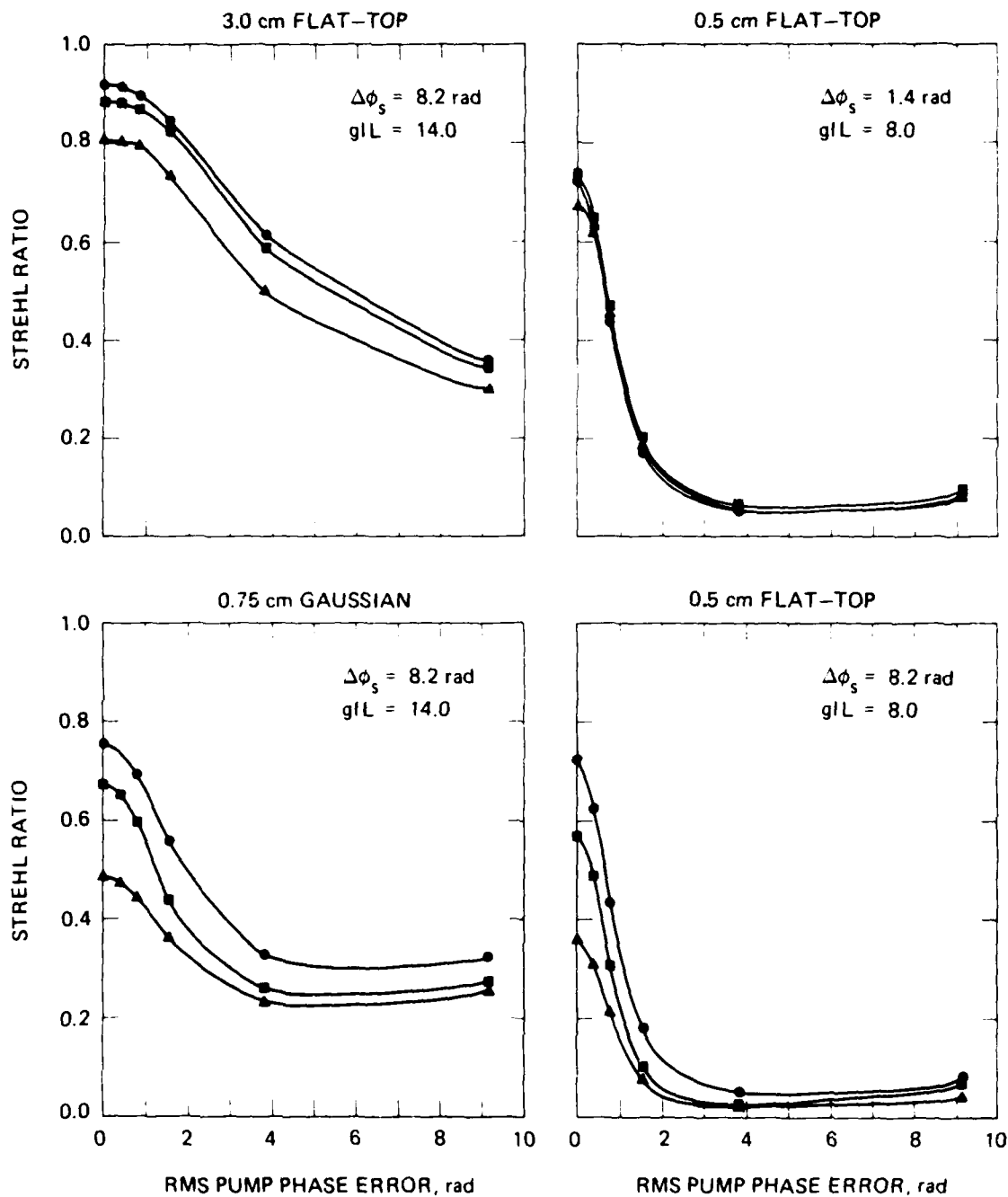


Figure 15. The effect of pump aberration on the Strehl ratio of the seed beam. In each quadrant, the top curve is for an unaberrated beam geometry, the central curve the aberrated-conjugated geometry, and the lowest curve the aberrated-phase-only-conjugated geometry.

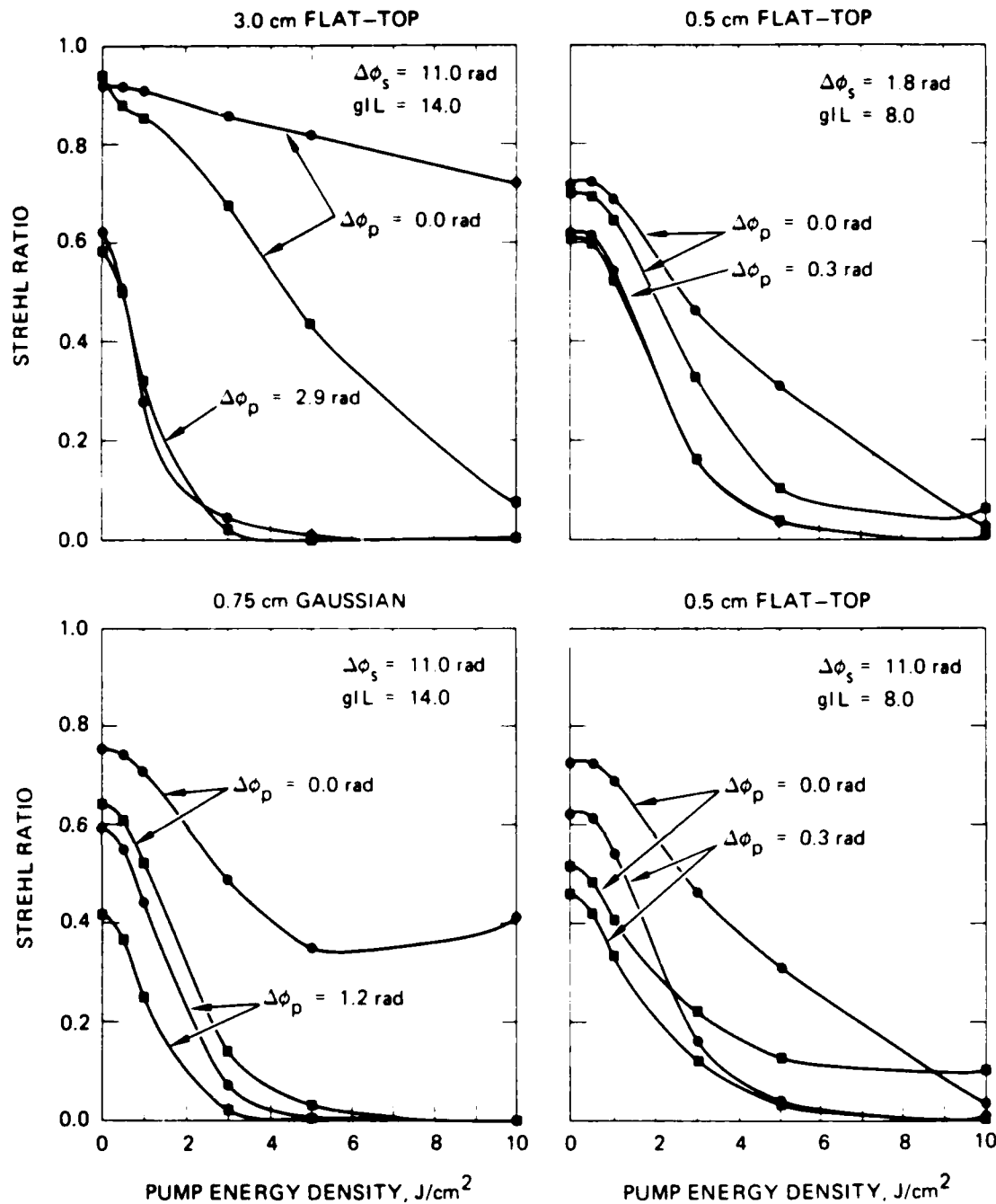


Figure 16. The effect of RIVED on the Strehl ratio of the seed beam. This effect is applicable only to short pulse applications, and the plotted Strehl ratios are what would be observed at the end of the pulse. In each quadrant, the top two curves are for a clean pump and the bottom two curves are for an aberrated pump. Within each pair, one curve (solid circles) represents an unaberrated beam geometry and the other (solid squares) an aberrated-conjugated geometry.

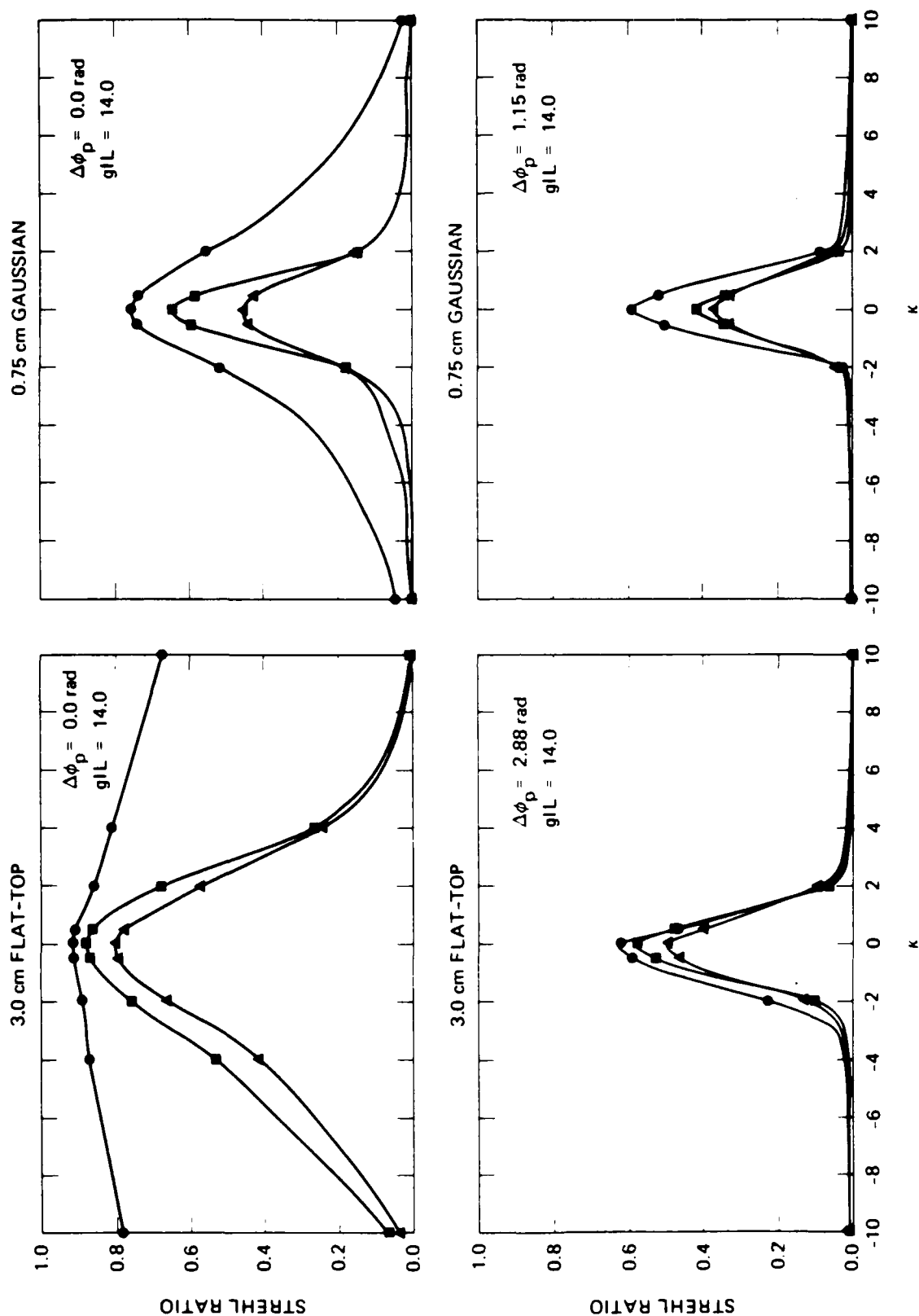


Figure 17. The effect of nonlinear dispersion on the Strehl ratio of the seed beam. In each quadrant, the top curve is for an unaberrated beam geometry, the central curve the aberrated-conjugated geometry, and the lowest curve the aberrated-phase-only-conjugated geometry.

Fresnel number (21) Gaussian beam. In each quadrant, we plot the Strehl ratio of the seed beam as a function of the seed aberration. The amount of seed aberration is represented by the RMS phase error of the phase aberration plate. This RMS value is found by direct evaluation of the phase screen, because different initialization values for the random number generator yield slightly different RMS phase errors. RMS phase errors up to 10 rad are shown in the figure. In RAs where the gas flow has been specifically designed to minimize thermal gradations, we expect aberrations of a few radians (see Appendix B). It should be remembered in the following discussion that we are considering optical beams aberrated up to 2 to 3 times what would be expected in a well-designed system. In the absence of phase conjugation, the aberration of the seed beam is actually twice that of the aberrating plate because it is double passed in the system.

The top curve in each quadrant gives the Strehl ratio of the output beam when a perfect phase and amplitude phase conjugator is used. As expected, there is no reduction of Strehl ratio for RMS phase aberrations as large as 8 rad. The figures show a Strehl ratio of 0.985 for the flat-top beams; this represents the precision with which our code can numerically diffract beams. With the truncated Gaussian beam, the results were normalized to the unaberrated case. As a result, the Strehl is 1.0 for the perfect conjugator. The Strehl of the conjugated beam remains at 1.0 for seed aberrations as large as 11 rad, demonstrating the ability of our diffraction code to accurately simulate diffraction of highly aberrated beams. The central line in each quadrant represents the case where a phase-only conjugator is used. As expected, the Strehl ratio falls off with increasing aberration. For small aberrations, the fidelity of the flat-top beams is very high, because propagation across the amplifier cell has not turned the small phase aberration into a significant amplitude aberration. Therefore, the phase-only (flat-top amplitude) conjugation gives a reasonably good conjugate of the input beam.

It is evident that the beam fidelity falls off with increasing aberration because diffractive effects induce intensity variations on the beam before it reaches the conjugator. It is interesting to note that the Strehl ratio falls off much more rapidly for the low Fresnel number beams, where diffractive effects are much stronger. For small aberrations, the Strehl ratio of the Gaussian beam does not asymptotically approach the perfect conjugator case, because we assume a flat-top intensity profile for our phase-only conjugator even for the Gaussian beam case. Finally, the lower curve in each quadrant gives the results when an ordinary mirror is used. As can be seen, the Strehl of the unconjugated system falls off very rapidly, reducing to ~ 0.1 with RMS phase errors of ~ 1.3 rad. In the description that follows, we find interesting results for RA/SBS systems where the RMS phase errors are ~ 8 rad. Here, the uncorrected (i.e., without conjugation) Strehl ratio is $\ll 0.001$; the actual value in this case is subject to significant numerical errors and is too small to be of significance. For this reason, we do not attempt to compare the conjugated system with the unconjugated system; rather, the conjugated system with seed phase-aberrations is compared to an unconjugated system without seed phase-aberrations. It should be remembered throughout this discussion that, even when the Strehl ratio of the conjugated system drops by an order of magnitude, we are modeling beams with such large aberrations that, without conjugation, the Strehl ratio would be $\sim 10^3$ lower.

Figure 11 shows the effect of adding gain to the RA. To demonstrate the effect of gain in the amplifier, we have chosen four representative aberration conditions, indicated by the arrows on Figure 10. Three curves are shown in each quadrant of the figure. The upper curve gives the output Strehl ratio of an unaberrated seed beam. The central line shows the results for a aberrated-conjugated beam. The lower line represents an aberrated-phase-only-conjugated beam. In all cases the pump beam

was unaberrated. With very low Raman gain, the perfect conjugator is able to correct for all seed aberrations, while the phase-only conjugator is somewhat less effective. As the gain is increased, saturation and pump nonuniformity begin to play an important role, altering the intensity pattern of the seed beam on its second pass through the amplifier. This, together with diffraction, yields an inaccurate intensity/phase profile when the beam retraverses the seed-phase aberrating plate, and leads to a reduced Strehl ratio. When the gain becomes extremely high, the pump is strongly depleted soon after it enters the amplifier (before diffraction has a significant effect). This results in a seed amplitude profile that nearly matches the pump amplitude profile at the amplifier input. Because the pump is unaberrated in this example, the seed profile becomes uniform (flat-top), closely matching the case of a phase-only conjugator. As can be seen in the figure, the Strehl ratio of the aberrated-conjugated beam matches the unaberrated beam for low gain, and approaches the Strehl ratio of the phase-only conjugated beam at high gains.

The results for the low Fresnel number flat-top beam are shown on the right side of Figure 11. In the upper right quadrant are the results for low seed aberration ($\phi_{RMS} = 1.4$ rad). We see that, for typical values of small-signal gain ($g_{IL} < 10$) the phase conjugator is capable of correcting for essentially all the reciprocal phase errors (induced by the aberration plate). This is evident because the Strehl ratio of the aberrated-conjugated beam is indistinguishable from the unaberrated beam. Both Strehl ratios are reduced because the diffraction rings on the pump lead to nonuniform gain, altering the intensity profile of the seed beam. At high gains ($g_{IL} \sim 14$), pump depletion begins to play an important role. The Strehl ratio of the unaberrated-unconjugated beam continues to decrease, approaching a value of ~ 0.5 . The Strehl ratio of the aberrated-conjugated beam decreases only slightly farther and becomes equal to the phase-only-conjugation Strehl at very high gains (saturation).

A more dramatic example is shown in the lower right quadrant where the seed phase aberration has been increased $\sim 6X$ ($\phi_{RMS} = 8.2$ rad). The general trends are the same as discussed above; however, the effect of aberration is much stronger. The difference is the intensity aberration of the seed (due to diffraction of larger seed aberrations) is much larger, and the effects of poor amplitude preservation (gain saturation or phase-only conjugation) are more evident.

As discussed above, the decrease of the Strehl ratio under conditions of high gain is due largely to intensity aberrations that result from diffraction of the large phase aberrations produced by the aberration plate. It follows that a higher Fresnel number geometry should yield better results. The high Fresnel number beam geometry is given in the upper left quadrant of Figure 11. As in the lower right, the phase aberration $\phi_{RMS} = 8.2$ rad. Here, the Strehl ratio remains largely independent of the Raman gain, because the large Fresnel number geometry minimizes diffraction effects and the seed beam intensity profile remains uniform.

The Gaussian beam result is shown in the lower left quadrant of Figure 11. The results are qualitatively different from those obtained with flat-top beams: at low to moderate gains the Strehl ratio decreases, but at high gains the ratio increases. Investigation has shown that this initial decrease is due to the nonuniform gain resulting from the Gaussian profile of the pump, which serves to dramatically reduce the near-field beam diameter and hence the Strehl ratio. At high gains, saturation becomes important. Because the gain is significantly higher in the center of the pump, the seed beam depletes the central portion of the pump, giving relatively higher gain to the outer regions. As the seed depletes the entire pump beam, it begins to replicate the pump intensity profile. If it were not for diffraction, the two intensity profiles would be identical and the Strehl ratio would regain a value very near 1.

To emphasize this point, we have plotted the aberrated-conjugated curve for the Gaussian beam along with similar curves calculated for other injection ratios (seed-to-pump intensity ratio). As the injection ratio changes, so does the amount of gain required for the seed beam to deplete the pump. To compensate for this, we plot the data in Figure 12 as a function of photon conversion efficiency (η) rather than the small-signal gain parameter (g_{IL}). The aberrated-conjugated curve of the lower left quadrant of Figure 11 is shown by the curve labeled "injection ratio = 10^{-2} "; that is, an injection ratio of 1%. It is clear from the figure that, as the injection ratio is reduced, the Strehl-reducing-effect of nonuniform gain is enhanced. It is interesting that the Strehl ratio for lower injection remains low, even at high photon conversion efficiency. The reason is the low injection ratio requires very high gain and, with high gain, aberration of the pump becomes very important. For the purposes of this plot, we are using an RMS seed phase error of 8.2 rad. When the unconjugated seed double passed this aberrator, its Strehl ratio was reduced to well below 10^{-3} . In fact, to the extent that single-passing an aberrator with $\Delta\phi_{RMS} \sim 8.2$ rad is equivalent to double-passing a $\Delta\phi_{RMS} \sim 4.1$ rad aberrator, we expect that the Strehl ratio of the pump is ~ 0.01 (see Figure 10) after passing through the seed aberration plate. Therefore, if the seed beam truly matched the pump (pump replication), the Strehl ratio would be ~ 0.01 , rather than the observed values > 0.3 . It follows that, even in the worst case represented in Figure 12, the conjugator still does a good job of correcting the reciprocal phase errors.

In Figure 13, we have plotted the photon conversion efficiency as a function of the small-signal gain parameter. Shown in the figure are the results for a 0.5-cm-diameter flat-top beam (injection ratio 10^{-4}) and a 0.75-cm truncated Gaussian beam (injection ratios 10^{-2} and 10^{-4}). It is clear from the figure that it is much more difficult to deplete the Raman gain (high

photon conversion efficiency) for Gaussian beams than it is for flat-top beams. The flat-top beam attains good photon conversion efficiency (>90%) with physically realizable small-signal gain parameters ($gIL \sim 15$). This flat-top evaluation is in good agreement with the formula for photon conversion efficiency (η) in one dimension.²⁴

$$\eta = \left(1 + \left| \frac{\lambda_p}{\lambda_s} \left(\frac{u_{si}}{u_{pi}} \right)^2 - 1 \right| e^{-gI_p L} \right)^{-1} \quad (12)$$

The equivalent situation for a Gaussian beam is shown by the lowest curve in Figure 13. At a small-signal gain parameter (gIL) of 15, the photon conversion efficiency of the Gaussian beam is roughly half that of the flat-top beam. At the highest gains shown in the figure, the photon conversion efficiency has still attained only a value of ~60% - the result of the low gain on the outer edges of the pump. If the injection ratio of the seed is increased, the situation improves. The central curve is plotted for a Gaussian beam with an injection ratio 100X larger than the other two curves. For small gains, the conversion efficiency is higher, but the flat-top beam is superior for high conversion efficiency. Analytic results for small-signal gain parameters as high as 25 are plotted in the figure. In practice, however, these gains are probably not achievable. Not only will amplified spontaneous emission (ASE) become important, but also 2nd Stokes will be generated from the center before the outer ring is saturated. These effects were not included in the code.

Up to this point, we have discussed the effects of reciprocal phase error and diffraction in the RA with a unaberrated pump beam. The effects of depletion and saturation of the pump beam have also been discussed. When considering a truncated Gaussian pump beam, we found significant effects caused by nonuniform gain. At this point, we wish to consider the effects of adding phase and intensity aberrations to the pump beam, which results in highly nonuniform gain that cannot be compensated with the phase conjugate mirror.

We created a dirty pump beam with both phase and amplitude aberration by placing a phase aberrating screen in the path of the pump beam and allowing propagation (diffraction) to create intensity aberrations. For convenience, this propagation distance was chosen to be equal to the Raman cell length. The intensity aberrations of the pump beam are transmitted to the seed beam through nonuniform gain. These seed intensity aberrations develop into phase aberrations during propagation across the amplifier. The degree to which the seed beam replicates the pump depends on the interplay of nonuniform gain, saturation, and diffraction. High fidelity replication of the pump occurs only under limited conditions and was not observed from the simulations done under this program. An example of this process is shown in Figure 14. On the left side of the figure, the seed beam (a 0.5-cm unaberrated flat-top) is shown at the entrance to the amplifier (after conjugation). The upper left grayscale plot is the intensity profile, while the lower left grayscale plot is the phase profile. It is evident that the seed has developed a small phase ripple as a result of diffraction, but there is no discernible ripple in the intensity. The pump beam, shown by the central grayscale plots, has been aberrated ($\Delta\phi_{RMS} = 3.8$ rad) and allowed to propagate. The pump has large amplitude and phase aberrations (pump Strehl ~ 0.025). On the right side of the figure, the intensity and phase of the seed are shown at the amplifier output (gIL = 8). Clearly, the seed has picked up large aberrations from the pump. The seed aberrations do not, however, replicate the pump aberrations because: (1) the pump and seed diffract at different rates because of their different wavelengths; (2) the small-signal gain parameter gIL = 8 causes the high intensity portions of the pump to saturate at the beginning of the RA; consequently, nonuniform gain and diffraction can not cooperate to give a good replication.

For comparison with prior results, we have considered the addition of pump aberrations to the results shown in Figure 11. Figure 15 shows the effect of aberrating the pump beam at the

points indicated by the arrows in Figure 11. The beam geometries for each quadrant in Figure 15 are the same as in the corresponding quadrant in Figure 11. The general conclusion from this figure is that nonuniform gain caused by pump intensity aberrations cannot be compensated by phase conjugation. This does not mean that the conjugator is not working. The conjugator is able to compensate for essentially all the reciprocal phase errors introduced by the aberration plate. It is clear from Figure 15 that the Strehl ratio for all three curves fall off together. That is, the aberrated-conjugated system behaves just as well as the unaberrated system. It follows that gain nonuniformities must be minimized by "smoothing" out the pump intensity aberrations. This can be accomplished by providing more uniform pump beams or by lowering the gain and increasing aberration so that the pump beam aberration averages out. It is also evident from Figure 15 that the higher Fresnel number geometries (large flat-top and Gaussian beams) have higher Strehl ratios, which is not surprising, because the larger beams experience less diffraction and hence less intensity aberration.

As described in the preceding discussion, we found no situations under which the perfect phase and amplitude conjugator was unable to compensate for essentially all the reciprocal phase errors. We do, however, find such an effect when we consider RIVED, which, in contrast to the effects described above, leads to a direct phase error rather than an intensity error.

The Raman amplification process transfers molecules from the ground state to a vibrationally excited state. While in this excited state, the molecules have a different polarizability, which leads to a change in the index of refraction. Clearly, this can only be a strong effect when significant numbers of molecules are transferred to the excited state, and when they do not have time to thermalize and/or diffuse out of the regions of high intensity. If all the molecules are excited, the polarizability of the medium increases by 20% (hydrogen). To estimate

the change in refractive index, we assume an optical pulse that is much shorter than the phonon relaxation time. It follows that every photon transferred from the pump to the Stokes wave yields an excited molecule. If we also assume that the medium does not saturate (i.e., we don't use up the available molecules), we find that

$$\Delta\Phi = 0.4\pi P(n-1)_0 \left(\frac{J_p}{A} \right) \left| Nhc \Delta(|u_s|^2) \right|^2, \quad (13)$$

where $\Delta\Phi$ is the phase error accumulated by the end of the pulse at a given location, P the gas pressure, $(n-1)_0 \sim 135 \times 10^{-6} \text{ amagat}^{-1}$, (J_p/A) the initial peak pump intensity, N the gas density, h is Planck's constant, c the speed of light, and u_s the Stokes field normalized (as in the code) to the initial peak pump field.

The result of this simulation is shown in Figure 16. As in Figures 11 and 15, there are four quadrants, each representing a particular beam geometry. The upper and lower right quadrants are for the low Fresnel number flat-top beam, with the low aberration at the top and high aberration at the bottom. The upper left is for a high Fresnel number flat-top beam, and in the lower left, a moderate Fresnel number truncated Gaussian. Each quadrant contains four curves. These curves represent the unaberrated and the aberrated-conjugated beams with, and without, pump aberration; each is plotted as a function of pump energy density. The unaberrated results are indicated by the solid circles, while the aberrated-conjugated results are shown by the solid squares.

As expected, the Strehl ratio is reduced by the effects of RIVED. It is interesting that, when the pump is unaberrated ($\Delta\phi_p = 0.0 \text{ rad}$), the Strehl ratio of the aberrated-conjugated beam can be significantly lower than that of the unaberrated-unconjugated beam. In contrast, the two Strehl ratios are nearly equivalent for aberrated pump beams.

For unaberrated pump beams, we believe the reduction in Strehl ratio is due to the effect of seed aberration. That is, the seed beam aberration causes the seed intensity near the conjugator to be highly nonuniform. The number of molecules transferred to the excited vibrational state, giving rise to the RIVED, is then proportional to the seed intensity (uniform pump intensity), and, thus, is spatially highly nonuniform. It follows that the aberrated seed beam experiences a much larger nonreciprocal phase error. For the Gaussian beam, the effect is even more pronounced - the result of a lensing action caused by the higher pump intensity, and therefore higher photon conversion efficiency, near the center of the beam.

For the aberrated pump beam, spatial nonuniformity of the excited vibrational state density results from pump intensity aberrations as well as seed aberrations. In this case, the effect from the seed aberration is masked by the pump aberration.

This RIVED effect is applicable only for short optical pulses - so short that the seed beam does not overlap itself completely on the first and second passes through the amplifier. If it did, the phase error, due to RIVED, would be sensed on the first pass and compensated by the conjugation (i.e., the effect is reciprocal).

An additional effect, giving rise to a direct phase aberration of the seed beam, is due to nonlinear dispersion, which in turn is a result of frequency mismatch between the Stokes seed beam and the Raman gain. This effect can result from either multimode operation, where the laser linewidth is not narrow compared to the Raman linewidth, or from an uncompensated SBS frequency shift. In contrast to RIVED, this is a true nonreciprocal phase error, because the Raman process gives gain only in one direction. As discussed in Section 2, the amount of nonlinear dispersion can be evaluated from the Kramers-Kronig relationship. The magnitude of the dispersion is proportional to the small-signal gain of the amplifier:

$$g_{IL} = \frac{1 - 2i(\delta\omega/\Gamma)}{1 + 4(\delta\omega/\Gamma)^2} g_o IL \quad (14)$$

This relationship shows that the maximum dispersion occurs at a frequency offset equal to one-half the full-width-half-maximum ($\delta\omega = \Gamma/2$) of the Raman gain line; at this point, it attains a value of $g_o IL/2$. Nonlinear dispersion has been simulated in our code by using a complex gain parameter $g_{IL} = \Phi(1 - i\kappa)$. It follows that the largest realizable value of κ is 0.5. From Figure 17, which shows the results of modeling this effect, the conclusion can be drawn that this value will not cause any significant degradation of beam quality.

It follows that nonlinear dispersion does not have a serious effect on the RA/SBS system. For illustration purposes, we have modeled frequency offsets as large as $\kappa = 10$. Although this represents a condition not achievable by the process of nonlinear dispersion, there could be other nonlinear processes that produce such effects. The figure shows that the effect is more significant for distorted pump beams and can have significant effect for values of κ approaching 2. This implies that the nonlinear induced phase shift must be kept to less than a wave within the Raman gain length (i.e., $\kappa < 1$).

In summary, we have modeled the effects of pump and seed aberration on the beam fidelity of a RA/SBS system. Our simulation includes diffraction of the seed and pump beams, Raman gain, gain saturation/pump depletion, RIVED, and nonlinear dispersion. All these effects give rise to nonreciprocal aberrations in the RA. The degree to which a phase conjugate reflector can compensate for reciprocal aberrations, in the presence of nonreciprocal aberrations, has been evaluated and was discussed in detail in the preceding paragraphs. The results of this study can be summarized as follows:

- (1) We modeled nonreciprocal phase errors present in RAs and found very few situations in which the phase conjugator was not able to compensate for simultaneously induced reciprocal phase errors. In these few situations, we found that the Strehl ratio of the conjugated beam would drop by a factor of 2 or 3 from what it would be if there were no reciprocal aberrations in the system. In these cases we are, however, modeling reciprocal aberrations strong enough to reduce the Strehl ratio by at least 2 to 3 orders of magnitude in a system without a conjugator.
- (2) When phase aberrations of the seed beam are strong enough to distort its intensity profile prior to conjugation, preservation of amplitude information during conjugation is required. High gain in the RA can lead to a strongly depleted pump before significant diffraction has occurred, and has the same effect on beam quality as a conjugator that does not preserve amplitude information.
- (3) Pump-dependent refractive indexes impair the ability of the conjugator to compensate for seed aberrations. Dispersion from operation off line-center of the Raman gain does not produce serious effects. However, RIVED, resulting from the transfer of significant numbers of molecules to their excited states, can be important for short pulses. This requires intense pulses shorter than the relaxation time of the excited vibrational level and the transit time of the system, and becomes noticeable for pulse energy densities $> \sim 1 \text{ J/cm}^2$.
- (4) For high gain and low Fresnel number geometries, strong aberrations can occur from nonuniform gain. Any impairment of the ability of the conjugation process to compensate for reciprocal phase errors was masked by deterioration of the beam due to nonuniform gain.

SECTION 4

EXPERIMENTAL RESULTS

4.1 GOALS OF THE EXPERIMENTAL PROGRAM

The goal of the experimental effort on this program was to set up a double-pass RA/SBS conjugator system, and evaluate its performance. More specifically, the objectives were to:

- (1) demonstrate that SBS phase conjugation can be used to compensate for reciprocal phase errors in the double-pass RA,
- (2) demonstrate that nonreciprocal phase errors exist in these systems, (3) evaluate the effect of nonreciprocal phase errors on system performance, and (4) compare the experimental results with the simulation code described in the previous section.

In previous programs at the Hughes Research Laboratories (HRL)^{13,25,26,27} and in the published literature,²⁸ SBS has been shown to produce high fidelity conjugate reflections. Unfortunately, quantitative results and evaluation of the range of validity are not easily obtained. A major effort during the experimental program was devoted to quantifying the beam fidelity so that the effect of nonreciprocal phase errors could be demonstrated. After arriving at methods to quantify the beam fidelity, we proceeded to demonstrate the dependence of the fidelity on the RA characteristics.

4.2 DATA REDUCTION AND INTERPRETATION OF RESULTS

Our experimental program consisted of measuring the seed beam fidelity as a function of experimentally adjustable parameters for both multimode and single-mode laser operation. The adjustable parameters include the pump energy, the seed energy, and the amount of pump and seed aberration. The dependence of the fidelity on these parameters gives insight into the physical processes that limit the fidelity in the double-pass RA/SBS system. The beam fidelity was determined from near- and far-

field energy distributions of the pump and seed beams. These distributions were measured using the laser intensity profiling system (LIPS) discussed below.

The LIPS used during these experiments consisted of a photodiode array camera, video digitizer, video frame buffers, and a computer for synchronization and data analysis. Figure 18 is a schematic of the LIPS system. Optical beams are recorded using an EG&G Reticon camera (m/n MC9256), which has a 256x256 photodiode array, controlled by an EG&G formatter (m/n MB900) to produce an RS-170 compatible video signal. The video signal is digitized by an Imaging Technology analog processor (m/n AP512) and stored in one of three Imaging Technology frame buffers (m/n FB512). Each frame buffer is capable of holding a single 512x512 video image, or up to four 256x256 video images. A companion Imaging Technology arithmetic logic unit (m/n ALU512) assists the analog processor for high speed video manipulations. The video digitizer and optical experiment are controlled by a Digital Equipment Corporation PDP micro-11/73 computer with a 30 Mbyte hard disk, a dual 5-1/4-in. floppy drive, a streamer tape unit, and a LA50 printer and VT240 graphics terminal for input and output. Synchronization for the camera and the computer

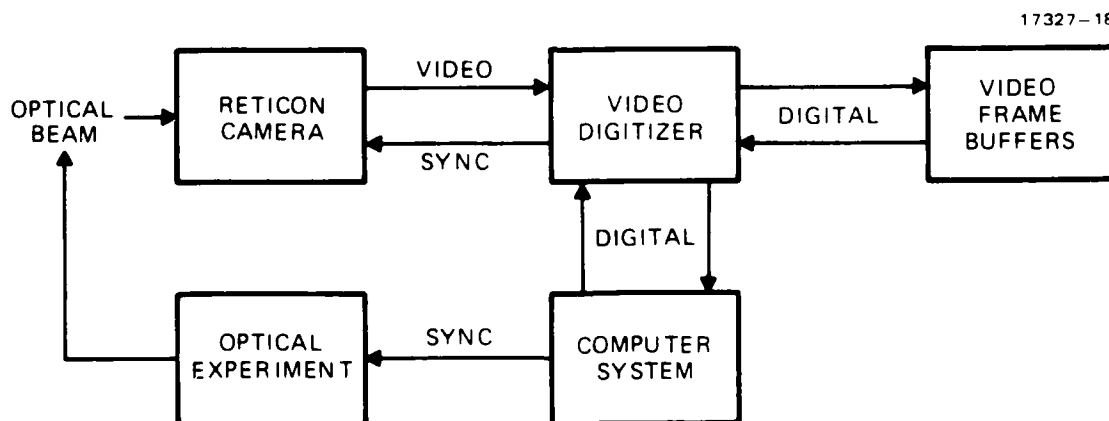


Figure 18. Schematic of the laser intensity profiling system used to evaluate near- and far-field intensity patterns.

system is provided by the video digitizer. The computer system synchronizes the pulsed lasers to the video system. Extensive software has been written on this system for controlling optical experiments and data reduction.

The LIPS digitizes the energy density, for a single shot of the laser, on a 256x256 grid. Several measures of beam quality are possible, including near- and far-field intensity profiles, beam sizes, Strehl ratios, and times-diffraction-limited (XDL). Near- and far-field intensity profiles are the basic data from which we calculate the beam fidelity. They are output either as contour plots of the intensity, or as profiles taken in the horizontal and/or vertical directions. Typical far-field beam contour and profile plots are shown in Figures 19 and 20.

These plots give good qualitative indication of the beam shape, but not a quantitative measure. We have used a "profile index" as a quantitative measure of the beam shape. This index, Ω , is defined by

$$\Omega = (\langle I \rangle \langle I^3 \rangle - \langle I^2 \rangle^2) / \langle I^2 \rangle^2, \quad (17)$$

where I is the energy density and the brackets " $\langle \rangle$ " indicate an integration over the transverse coordinates. This profile index is zero for a flat-top beam, is one-third for a Gaussian beam, and is 0.490 for the Airy disk pattern. Generally, the more spiked the beam is, the higher the profile index. Figure 21 shows a bullet plot of the profile indexes measured for the beams analyzed under this program. The ticks labeled "G" and "A" indicate the profile index of a Gaussian beam and an Airy disk pattern, respectively. The solid and open triangles represent the near- and far-field multimode laser measurements, respectively. The solid and open diamonds represent the near- and far-field single-mode laser experiments. As can be seen from the figure, the profile index of the near-field exposures lie between the Gaussian and the flat-top results. The multimode far-field

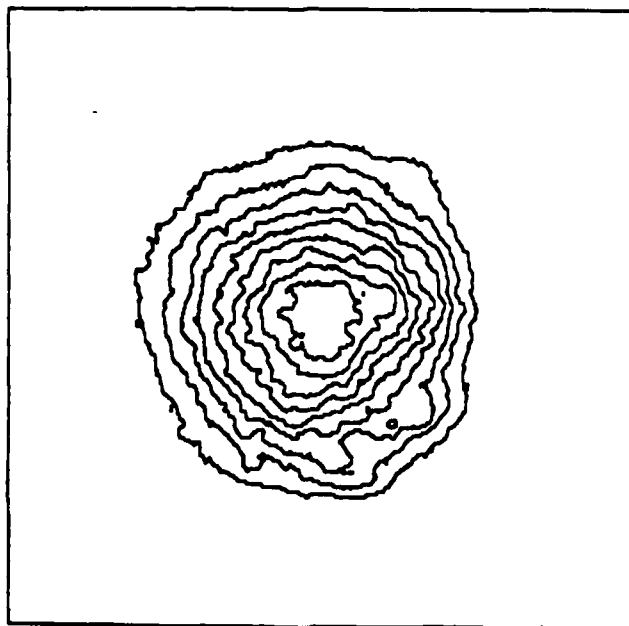


Figure 19. Contour plot of a typical far-field beam shape. In this figure the peak digitized value is 140, and the contour spacing is 14.

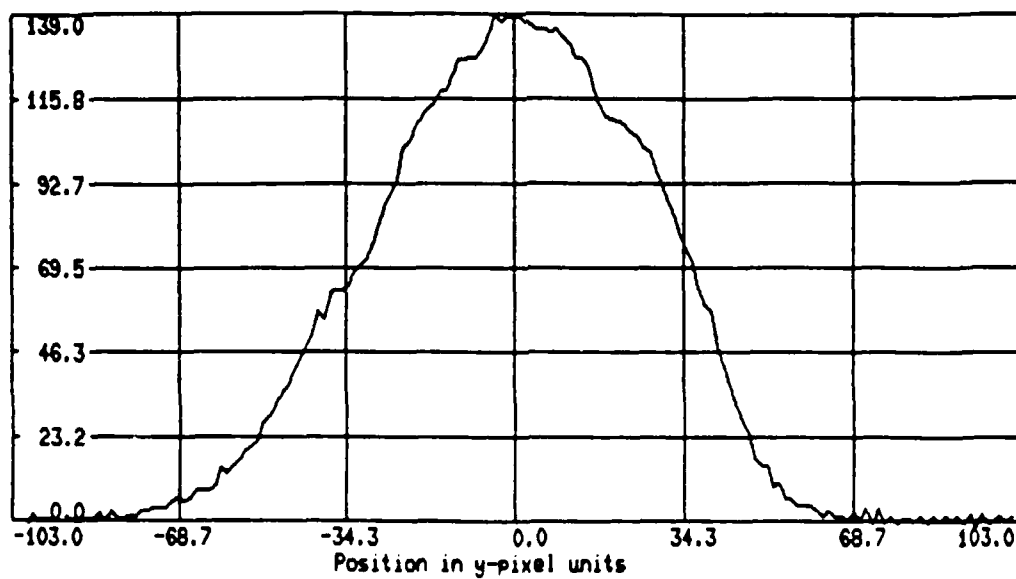


Figure 20. Profile of the beam shown in Figure 19, taken from a cut through the center of the beam along a horizontal axis.

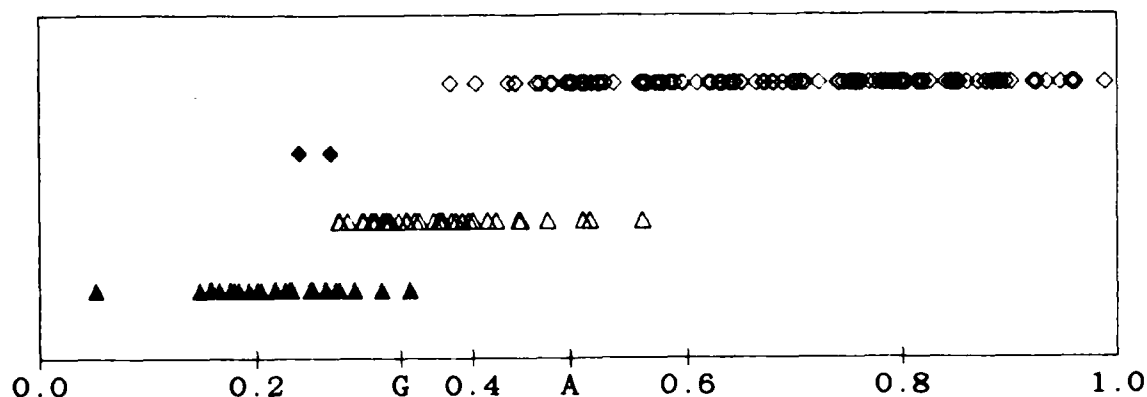


Figure 21. Bullet plot of the profile index for the beams analyzed during this program. A flat-top beam has a profile index of zero, a Gaussian beam has an index of one third (indicated by 'G'), and an Airy disk an index of 0.490 (indicated by 'A').

results lie generally between the Gaussian and Airy index, and the single-mode far-field index is generally higher. This implies that our beams are not strictly Gaussian or flat-top but actually lie somewhere between.

The fidelity of the laser beam was measured via the Strehl ratio and the XDL. Both of these measures compare the observed far-field to the far-field of an equivalent unaberrated beam. For flat-top and Gaussian near-fields, simple solutions exist for the far-field beam shapes. However, reference to Figure 21 indicates that our beams are neither Gaussian nor flat-top, and the assignment of an equivalent far-field beam shape is difficult. In addition, this assumption dramatically affects the calculated far-field of the beam; that is, the far-field radius of the Gaussian beam is approximately half as large, while its on-axis intensity is four times larger. To make our results comparable to the work of others, we have evaluated the beam fidelity both under assumed near-field shapes for the multimode laser results,

and under the Gaussian near-field shape for the single-mode results.

A beam with a flat-top near-field diffracts into an Airy disk pattern in the far-field. When examined, by observing in the focal plane of a lens with focal length f , the far-field intensity pattern is given by

$$I_f^f(\rho) = 4I_f^{nf} J_1^2[(k\rho_f^{nf}/f)\rho]/[(k\rho_f^{nf}/f)\rho]^2, \quad (18)$$

where subscripts indicate the flat-top beam, superscripts the far-field (ff) and near-field (nf), I_f^{nf} intensity in the near-field, J_1 a first order Bessel function, $k = 2\pi/\lambda$, and ρ_f^{nf} the near-field radius of the beam. We model the near-field radius of our "flat-top" beam by setting ρ_f^{nf} equal to the radius of an aperture that contains 90% of the energy in our near-field exposure. The far-field "flat-top," ρ_f^{ff} , radius is taken as the aperture radius that contains 83.79% of the energy of the far-field exposure, the same fraction of the energy as contained within the first dark ring of the Airy disk pattern. In both cases the aperture is positioned to allow maximum throughput from a smaller radius giving ~50% transmission. To obtain the XDL, the measured far-field radius (ρ_f^{ff}) is compared to the radius of the first zero in the Airy disk pattern calculated from the near-field radius (ρ_f^{nf}). That is,

$$XDL_f = \rho_f^{ff}/(j_{1,1} f/k\rho_f^{nf}), \quad (19)$$

where $j_{1,1}$ is the first positive zero of the first order Bessel function ($j_{1,1} \sim 3.83171$). The Strehl ratio is calculated by comparing the highest intensity pixel in the exposure with the peak intensity calculated from the Airy disk pattern, both normalized to the total power in the beam. It follows that the Strehl ratio θ_f is given by

$$\theta_f = (\sigma/E_o)/[\pi(\rho_f^{nf})^2/2\lambda^2 f^2], \quad (20)$$

where σ is the exposure level in the hottest pixel, and E_0 is the total exposure of the beam.

A beam with a Gaussian near-field diffracts into another Gaussian in the far-field. When examined, by observing in the focal plane of a lens with focal length f , the far-field intensity pattern is given by

$$I_g^{ff}(\rho) = I_g^{nf}(0) [\pi(\rho_g^{nf})^2/\lambda f]^2 \exp(-2[9\rho/(\lambda f/\pi\rho_g^{nf})]^2), \quad (21)$$

where the subscripts indicate the Gaussian beam. We model the radii of the "Gaussian" beams (ρ_g^{nf} and ρ_g^{ff}) by setting them equal to the radii of an aperture that contains 86.47% of the energy in the exposures, the same fraction of the energy as contained within the $1/e^2$ radius of a perfect Gaussian beam. As above, the aperture is positioned to allow maximum throughput from a smaller radius giving ~50% transmission. To obtain the XDL, the measured far-field radius (ρ_g^{ff}) is compared to the $1/e^2$ radius of the far-field Gaussian beam calculated from the near-field radius (ρ_g^{nf}). That is,

$$XDL_g = \rho_g^{ff}/(\lambda f/\pi\rho_g^{nf}) \quad (22)$$

The Strehl ratio is calculated by comparing the highest intensity pixel in the exposure with the peak intensity calculated from the far-field Gaussian beam pattern, both normalized to the total power in the beam. It follows that the Strehl ratio θ_g is given by

$$\theta_g = (\sigma/E_0)/[2\pi(\rho_g^{nf}/\lambda f)^2] \quad (23)$$

Our experimental program consisted of evaluating the profile indexes, the near- and far-field radii, the Strehl ratios, and the XDLs as a function of the experimentally adjustable parameters. Comparison with theoretical and simulation results allows identification of the nonreciprocal aberrations.

4.3 MULTIMODE LASER RESULTS

Multimode laser investigations were carried out using the experimental apparatus depicted in Figure 22. A YG581C YAG laser manufactured by Quantel International was used as the optical source. This laser consists of an actively Q-switched Nd:YAG oscillator/amplifier, designed for high energy applications. This results in an energetic, but highly multimode (transverse and longitudinal) laser output. The ~ 700 mJ IR ($\lambda = 1.06 \mu\text{m}$) output of the oscillator/amplifier is frequency doubled, resulting in ~ 300 mJ of vertically polarized optical energy in the visible spectrum ($\lambda = 532$ nm). This output is split by a 30% reflecting beam splitter; the 70% transmitted is used to pump backward stimulated Raman scattering (BSRS) for generating the seed beam (see below), and the 30% reflected by the beam splitter is used to pump the RA.

The polarization of the optical pulse transmitted by the beam splitter is first rotated to the horizontal plane by a half-wave plate ($\lambda/2$), and then focused into a high pressure H_2 cell to generate the Raman seed beam by BSRS. This red ($\lambda = 683$ nm) seed beam is separated from the green pump beam using an optical prism. The seed beam then passes through a 3:5 telescope reducer and an optional aberration plate before entering the RA. During its first pass through the RA, the seed beam senses aberrations due to optics and inhomogeneities in the amplifier. Because the seed beam is polarized orthogonal to the pump beam on the first pass, the Raman gain is very small; in addition, the Raman gain could be zero because the pump beam has not entered the amplifier. After leaving the amplifier, the seed passes through a dichroic mirror and is converted to circular polarization by a quarter-wave plate ($\lambda/4$). The resulting beam is focused into a SBS phase conjugation cell and reemerges with circular polarization of the opposite handedness. Thus, the polarization of this conjugated beam is converted to vertical linear polarization by the quarter-wave plate prior to being combined with the pump at

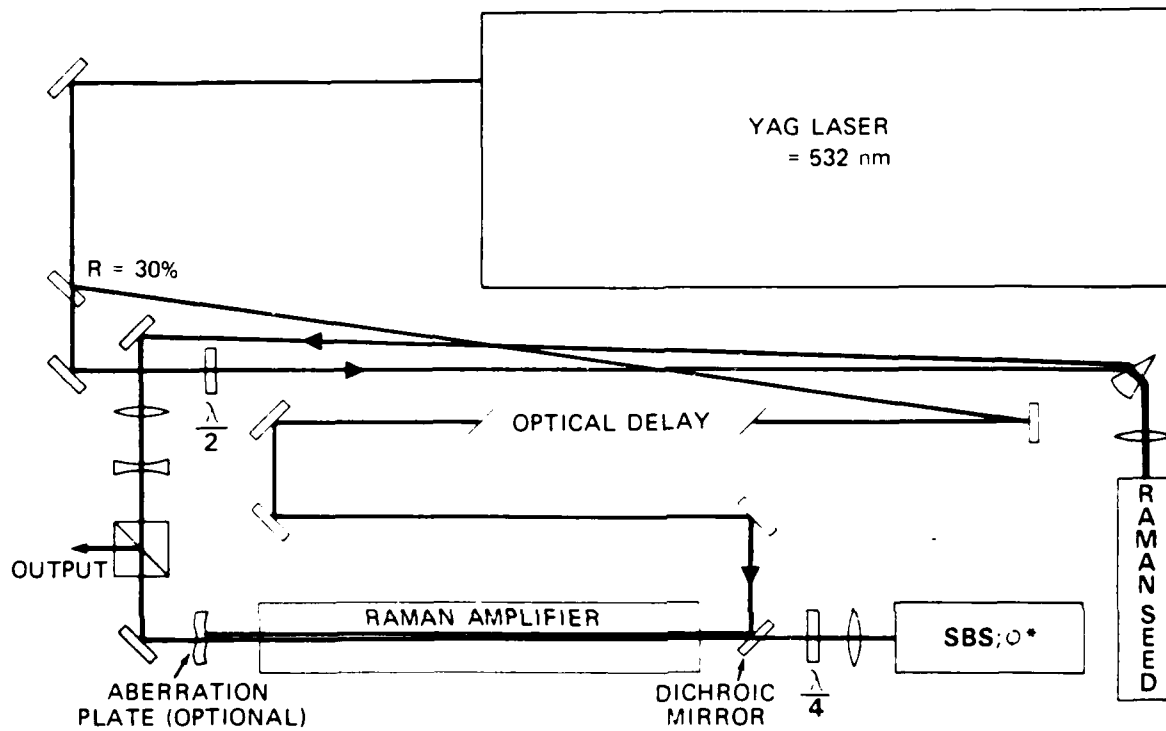


Figure 22. Schematic of the experiment used to observe the effect of nonreciprocal aberrations using a multimode laser.

the dichroic mirror. After being combined, the conjugated seed and the coincident pump beam enter the RA, transferring energy from the pump beam to the seed beam. The amplified conjugated seed beam repasses the optional aberration plate and is split off in a polarizer by virtue of its rotated polarization. At this point, the beams (seed and/or pump) are examined to determine their near- and far-field characteristics. The near-field is measured at the polarization beam splitter, while the far-field is measured at the focal plane of a 100 cm lens.

The pump beam for the RA is split off by the 30% beam splitter and undergoes an optical delay by transitting the table several times. The optical delay of the pump beam is adjusted so the pump will be coincident with the seed beam on its second pass through the RA. Two pumping configurations are used. In the first configuration, a long focal length lens is placed in the optical delay path. This lens images the laser output into the RA, producing a more uniform pump intensity than when the pump beam is allowed to simply diffract during the optical delay. In the second configuration, the pump beam is allowed to diffract during the optical delay.

The Quantel laser produces a highly multimode (transverse and longitudinal) optical pulse of ~ 10 ns duration. During these experiments, the laser was operated in two different modes: "smooth pulse," and "narrow linewidth." To operate this laser in the smooth pulse mode, an intracavity reflector is added to the oscillator. The effect of this reflector is to fill in the mode spectrum of the laser, driving the intermode beat frequency beyond the bandwidth of common laboratory detectors. The result is a pulse that appears temporally "smooth." This reflector increases the number of oscillating modes, but the laser bandwidth remains at the normal operation level of ~ 30 GHz. In the narrow linewidth mode of operation, an etalon is added to the oscillator to reduce the mode spectrum. With this etalon, the laser bandwidth is reduced to ~ 7 GHz. As discussed below, we

found, as expected, that in the smooth pulse mode the efficiency of the stimulated scattering processes was reduced because of the wide bandwidth. In fact, we were unable to obtain sufficient reflection from the SBS conjugator to demonstrate the operation of the RA/SBS system. In the narrow linewidth mode of operation, the laser linewidth was sufficiently narrow to obtain good SBS, and operation of the RA/SBS system was possible.

The seed beam for our RA/SBS system was created by BSRS. This process has been used successfully to efficiently generate high quality "conjugate" seed beams using narrow bandwidth lasers.²⁹ With wide bandwidth pump lasers, the BSRS process is less efficient and Raman seed beams are typically generated using forward stimulated Raman scattering (FSRS) in single- or multi-pass cells, or using resonator configurations.³⁰ In this program the BSRS and the FSRS processes were investigated, and the results are shown in Figures 23 and 24. In Figure 23, the stimulated scattering output is shown as a function of the pumping F-number. At low F-numbers, the BSRS output dominates, maximizing at $\sim F/15$ with a quantum efficiency of $\sim 17\%$, and beam quality matching the pump. At high F-numbers, the FSRS output dominates, achieving a quantum efficiency of $>60\%$ at $\sim F/100$. The beam quality is, however, very poor. In Figure 24, the stimulated Raman scattering (SRS) output is shown as a function of the cell pressure in low and high F-number geometries. In the low F-number ($F/13.6$) geometry, the BSRS output dominates for low pressure and is in strong competition with the FSRS at high pressures. In the high F-number ($F/104$) geometry, the FSRS output continues to increase with pressure.

Simultaneous experiments, discussed below, demonstrated that, while the BSRS process worked with the broad bandwidth laser, the SBS process would not. Because of this, the line narrowing etalon was inserted into the laser, narrowing the bandwidth to ~ 7 GHz. With the new narrower linewidth, the BSRS process became much more efficient. These results are shown in Figures 25 and 26. In Figure 25 the BSRS output energy is shown as a function

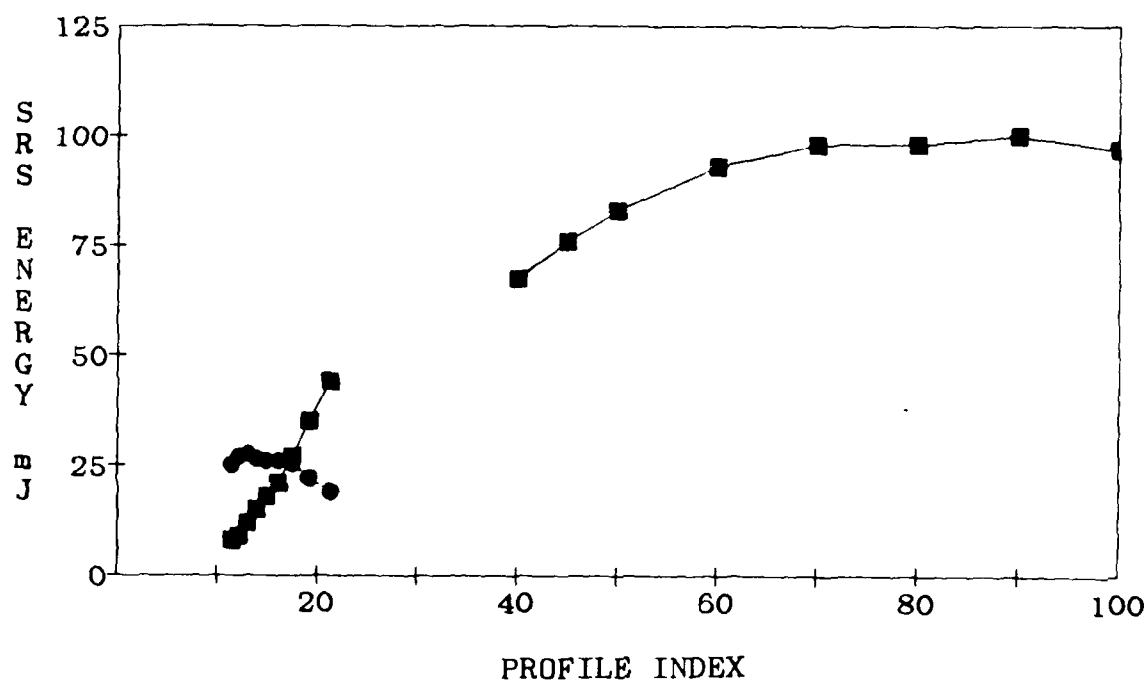


Figure 23. Energy contained in an SRS generated seed pulse. The Raman cell was filled with hydrogen at 1700 psi and pumped at a 532 nm wavelength with a 200 mJ wide bandwidth (30 GHz) laser pulse. The circles show the BSRS output; the squares, the FSRS output.

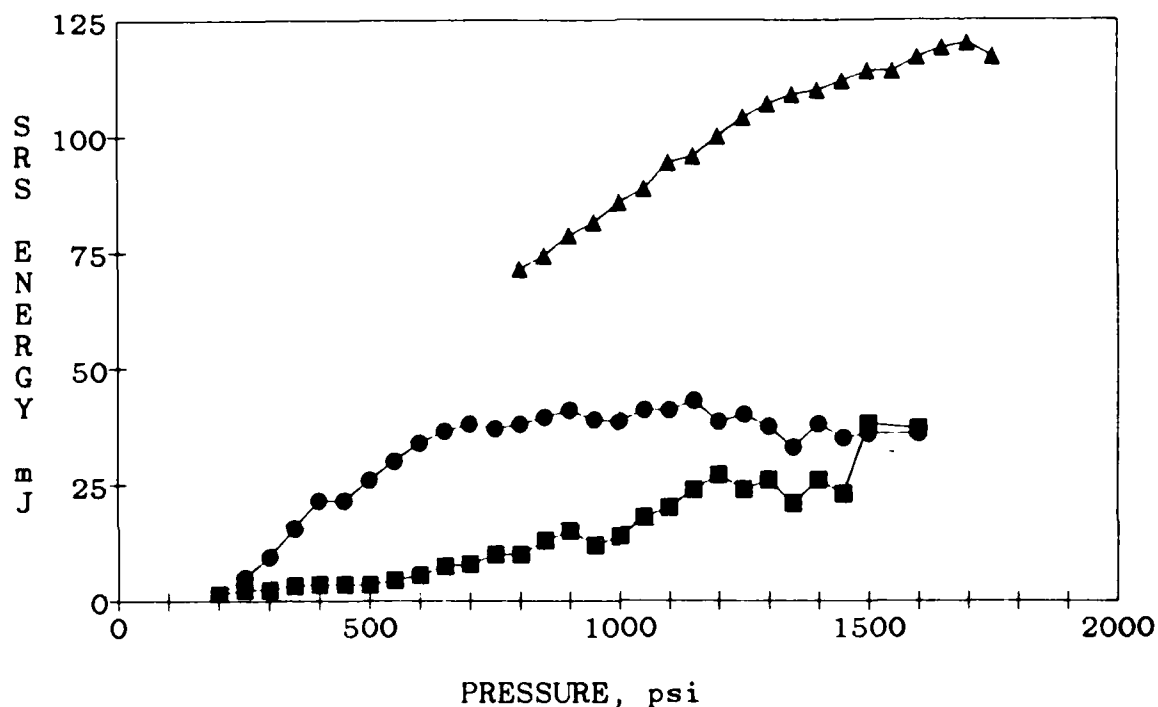


Figure 24. Energy contained in an SRS generated seed pulse. The hydrogen filled Raman cell was pumped at a 532 nm wavelength with a 200 mJ wide bandwidth (30 GHz) laser pulse. The circles and squares show the BSRS and FSRS output, respectively, in an F/13.6 geometry. The triangles show the FSRS output in an F/104 geometry.

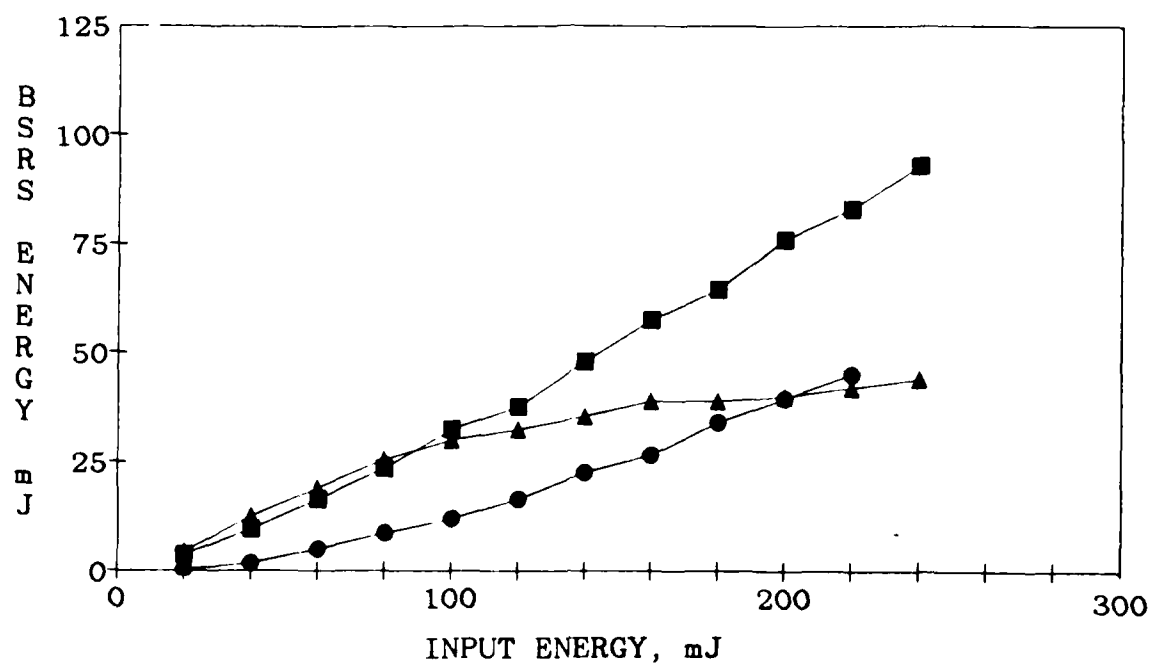


Figure 25. Energy contained in a BSRs generated seed pulse. The hydrogen Raman cell (1580 psi) was pumped at a 532 nm wavelength with a narrow bandwidth (7 GHz) laser pulse. The circles, squares, and triangles show the BSRs output in an F/7.5, an F/12.5, and an F/25 geometry, respectively.

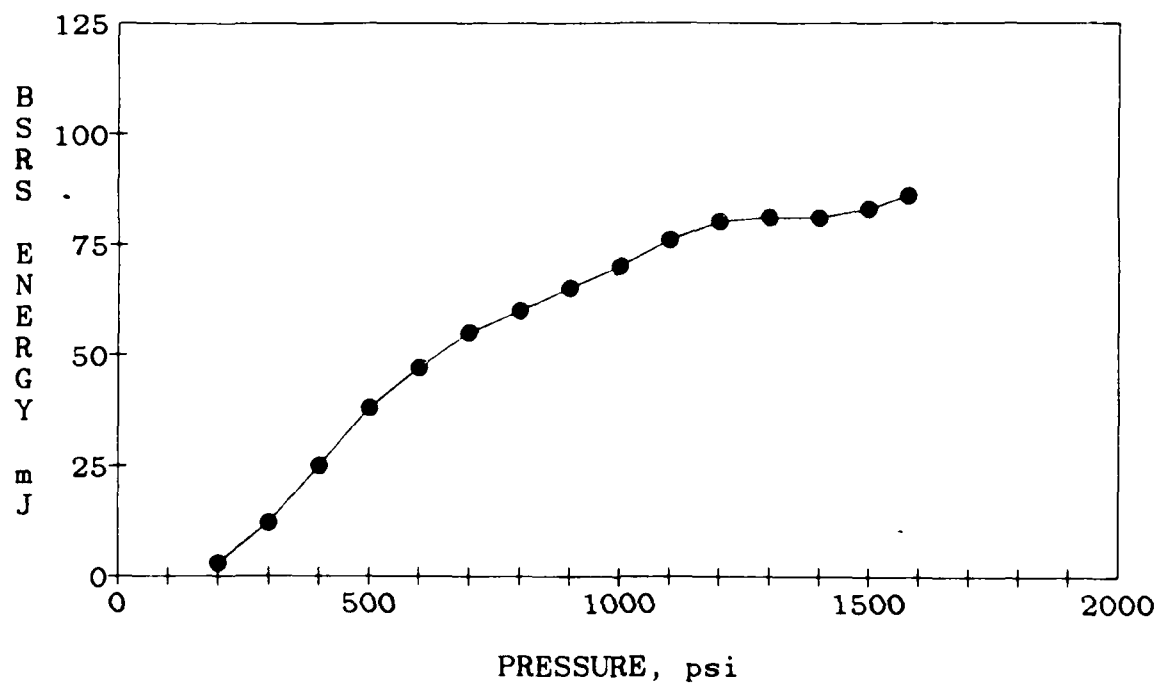


Figure 26. Energy contained in the BSRs generated seed pulse. The hydrogen filled Raman cell was pumped at a 532 nm wavelength with a 200 mJ narrow bandwidth (7 GHz) laser pulse in an F/12.5 geometry.

of the pump energy. The figure shows that the BSRS process is much more efficient with the narrow bandwidth laser, attaining a quantum efficiency of ~50% in an F/12.5 configuration. This is almost three times the value attained with the wide bandwidth laser. Figure 26 shows the BSRS output as a function of cell pressure for a F/12.5 pumping geometry. The output energy increases with cell pressure, saturating at ~1200 psi. For the purposes of demonstrating nonreciprocal aberrations in the RA, we operated the BSRS seed generator at a pressure of ~2000 psi with a narrow bandwidth pump of ~200 mJ. This gave a seed pulse of ~90 mJ at the input of the RA, and was large enough to obtain sufficient reflectivity from the SBS conjugator.

SBS phase conjugation of the multimode laser beams was performed in a high pressure gas cell. Both methane (CH_4) and sulfur hexafluoride (SF_6) were evaluated as conjugator materials. Neither gave suitable reflectivities with the wide bandwidth laser. In fact, the SBS reflection was sporadic and of poor quality. This held true under all pressures, focusing conditions, and pump energies at both 532 and 683 nm pump wavelengths.

With the narrow bandwidth laser, the situation was considerably improved. An SBS phase conjugate signal could be observed from the pump beam and the BSRS seed beam in both CH_4 and SF_6 . The observed reflectivity was in the 20% to 30% range for pump energies ranging from 25 to 200 mJ. At any given pressure, the SBS gain of SF_6 is substantially higher than CH_4 . However, SF_6 liquefies at a pressure of ~300 psi (room temperature), and at this pressure, the SBS gain in SF_6 is comparable to the gain in CH_4 at high pressure (~2000 psi). In initial experiments with SF_6 (300 psi), we observed BSRS in addition to the SBS signal; undoubtedly the presence of this competing nonlinear process reduces the fidelity of the phase conjugate signal. No BSRS was observed with CH_4 . For these reasons, we selected CH_4 as the best material for the SBS phase conjugator. The SBS cell was 37 cm long, contained CH_4 at a pressure of 2000 psi, and was

operated in an F/10 geometry. The SBS reflectivity of our CH₄ cell was estimated by first measuring the system losses and then taking them out of the reflectivities measured for the data discussed below. These estimates are plotted in Figure 27 as a function of input to the SBS cell. As can be seen, the SBS reflectivity is typically in the range of 20 to 30% for input energies of >20 mJ. At higher input energies, the SBS reflectivity did not increase substantially.

The RA used in these experiments was a 107-cm-long high pressure cell containing ~2000 psi of hydrogen. At this pressure, the Raman lineshift $\Delta\nu_r = 4154.80 \text{ cm}^{-1}$ gives a peak Raman gain at 683 nm (pump at 532 nm). The Raman linewidth $\delta\nu_r$ is approximately 7.1 GHz at this pressure.³¹ The SBS frequency shift for our CH₄ cell is only 1.3 GHz and the effect of being off line-center of the Raman gain is negligible. The peak Raman gain $g_0 = 3.0 \times 10^{-9} \text{ cm/W}$ gives a small-signal gain coefficient $g_0 IL \sim 2.4$ for a 40 mJ pump pulse.

As discussed above, our experimental observation of nonreciprocal aberrations consisted of evaluating the amplified seed fidelity as a function of experimental parameters. We begin this discussion by characterizing the pump beam, the seed beam, and the conjugation process. This is followed by a discussion of the effect of Raman gain and saturation of Raman gain on the conjugate seed beam fidelity.

As discussed above, the fidelity of our beams was characterized by evaluating the size of the beam and its peak intensity. The results of these evaluations on the pump beam are shown in Figures 28, 29, and 30. In Figure 28, the near- and far-field pump beam radii are shown as a function of the pump energy. These beam profiles were evaluated after the pump beam traversed the RA in the absence of the seed wave. As such, variations in the pump beam can be attributed to nonlinear interaction of the pump with itself (e.g., self-focusing). The radii are given by the radius of an aperture that, when centered on the beam, transmits a fixed fraction of the beam. The 0.9000 (triangles) and

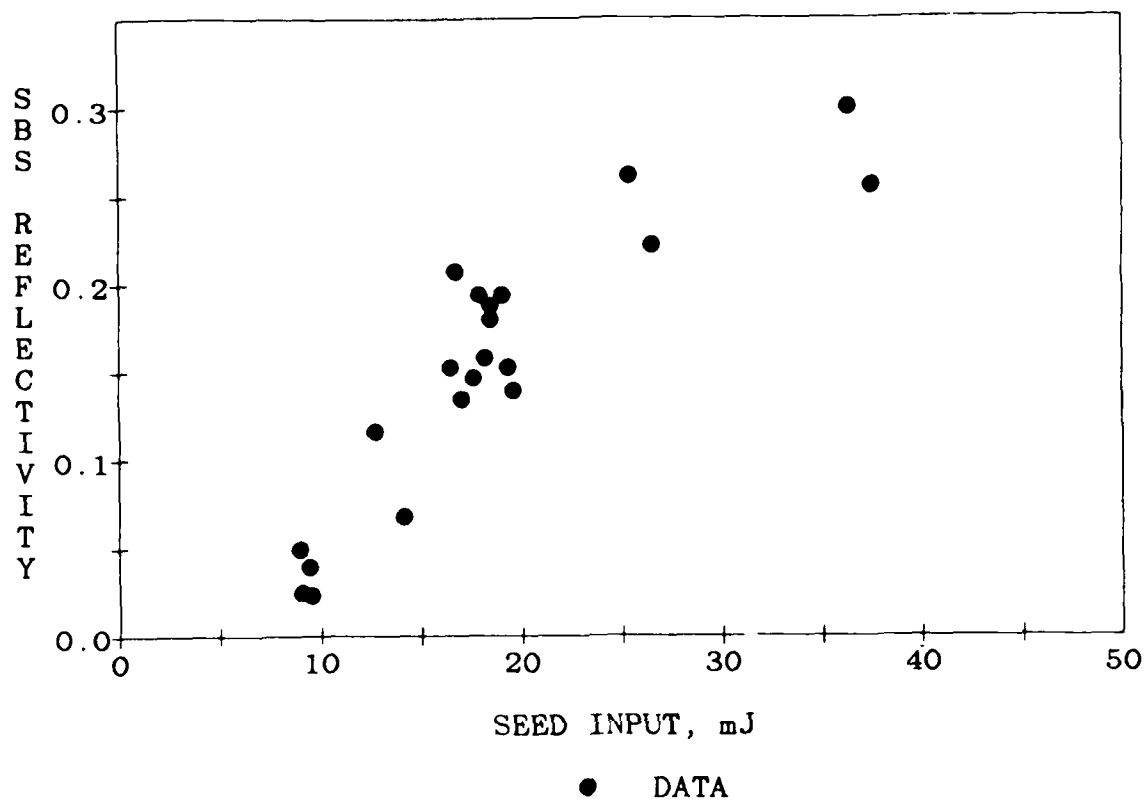


Figure 27. Estimated reflectivity of CH₄ SBS cell at a pressure of 2000 psi for narrow bandwidth (~7 GHz) radiation at a wavelength of 683 nm.

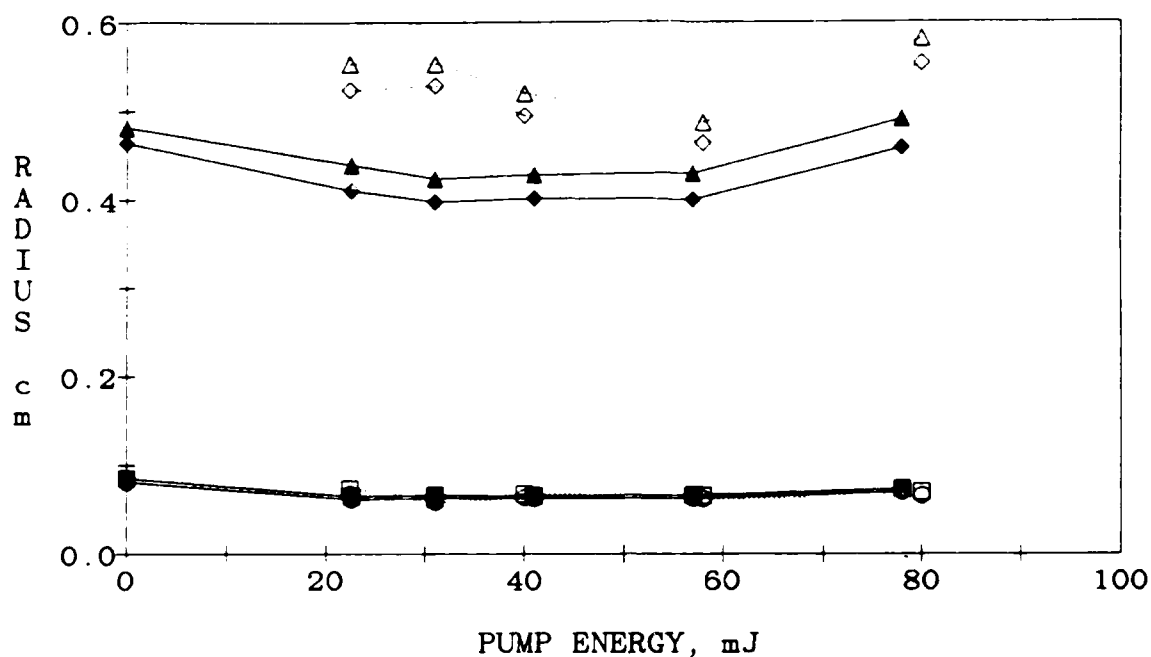


Figure 28. Pump beam radius as a function of the energy of the pump pulse. The radii are given by the radius of an aperture that, when centered on the beam, transmits a fixed fraction of the beam. The triangles and diamonds give the radii corresponding to 0.9000 and 0.8647 of the near-field beam, while the circles and squares give radii corresponding to 0.8379 and 0.8647 of the far-field beam, respectively. The solid symbols are for the imaged pumping geometry, while the open symbols are for the diffracted pumping geometry.

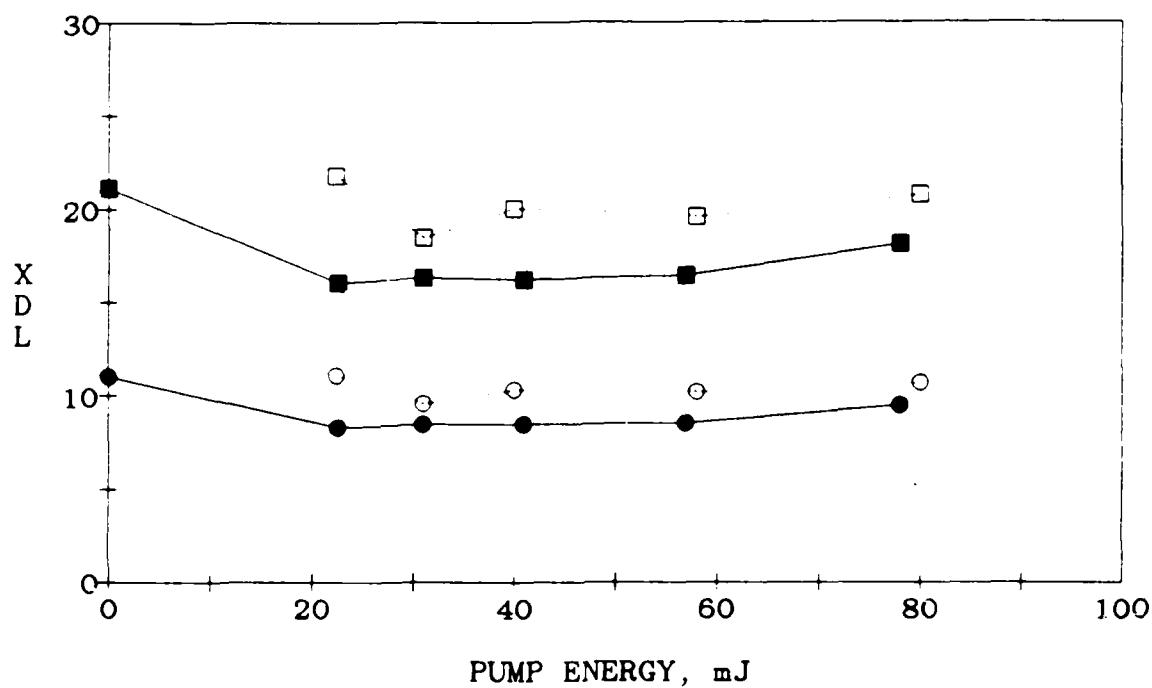


Figure 29. Pump beam XDL as a function of the energy of the pump pulse. The circles and squares give XDL under the flat-top and Gaussian beam geometries, respectively. The solid symbols are for the imaged pumping configuration, while the open symbols are for the diffracted pumping condition.

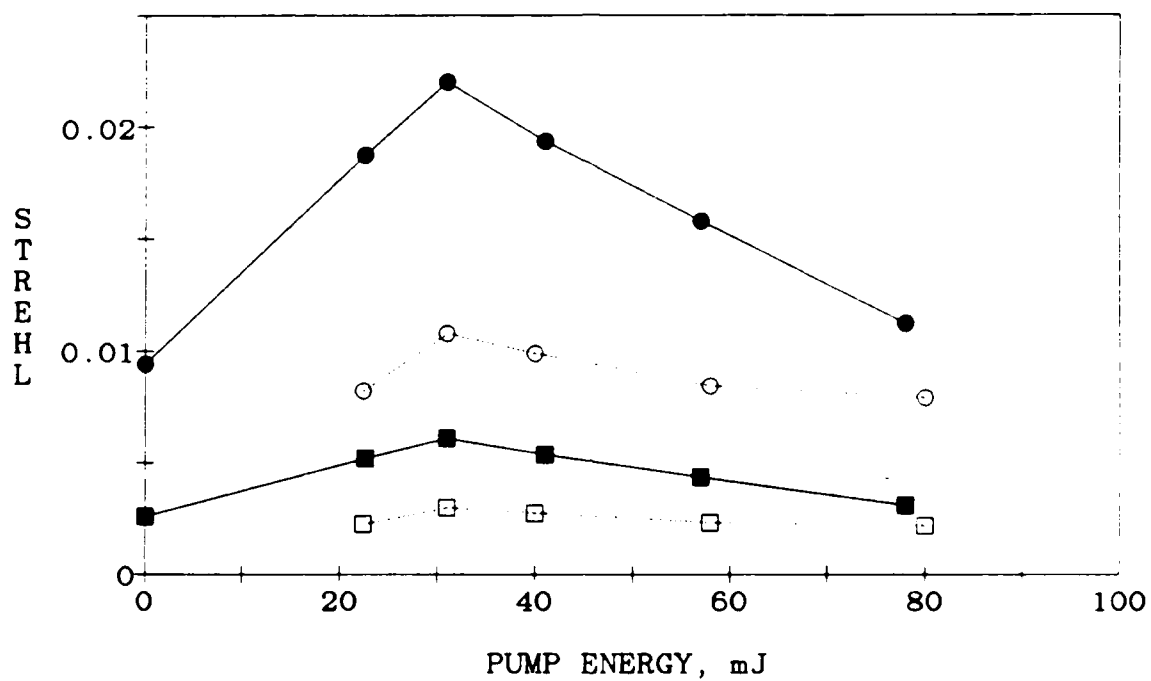


Figure 30. Pump beam Strehl as a function of the energy of the pump pulse. The circles and squares give Strehl under the flat-top and Gaussian beam geometries, respectively. The solid symbols are for the imaged pumping configuration, while the open symbols are for the diffracted pumping condition.

the 0.8647 (diamonds) radii of the near-field beam are used to estimate the radius of an equivalent flat-top and Gaussian beam, respectively. The solid symbols in the figure indicate results obtained in the "imaged" pumping geometry, and the open symbols, the "diffracted" pumping geometry. The value for a pump energy of "0" was obtained by removing the Raman cell. The data show very little change in the near-field beam radii. The small increase in the beam radii observed for high pump energy indicates that a nonlinear mechanism, such as self-defocusing, may be present in the amplifier, although its effect is small. The near-field radius of the pump beam was estimated by a linear least squares extrapolation to a pump energy of 0.0 mJ. These values were used to estimate the far-field radii and peak intensities as listed in the table below.

TABLE 1. Characteristics of Multimode Pump Beam.

PUMP BEAM	IMAGED		DIFFRACTED	
	GAUSSIAN	FLAT TOP	GAUSSIAN	FLAT-TOP
NEAR FIELD RADIUS (cm)	0.419	0.440	0.504	0.530
FAR-FIELD RADIUS (cm)	0.00404	0.00738	0.00336	0.00612
$I^f(0)/E_0$ (cm^{-2})	38919	10739	56334	15587

The XDL of the pump beam is plotted as a function of the pump energy in Figure 29. The circles show the flat top results and the squares the Gaussian results. As above, the open symbols represent the diffracted pumping configuration, and the solid symbols represent the imaged pumping configuration. As expected, the XDL of the pump beams increases slightly with increasing pump energy. In Figure 30, the Strehl ratio of the pump beam is plotted as a function of the pump energy. The Strehl ratio is seen to initially increase and then to decrease. This amounts to an

~2X change in the Strehl ratio. Reference to Figure 29 indicates that the far-field radius (XDL) changes by <20%, accounting for an ~40% change in the Strehl [$\text{Strehl} \propto 1/(\text{XDL})^2$]. Because the change in Strehl is larger, the far-field intensity profile must also be changing. That is, at high pump energies the far-field energy distribution flattens out.

The quality of our seed beam was characterized in an equivalent manner to the pump beam characterization discussed above. This characterization was done without the RA, the pump beam, or the SBS phase conjugator; the results are given below:

TABLE 2. Characteristics of Multimode Seed Beam.

SEED BEAM	GAUSSIAN CALCULATION	FLAT-TOP CALCULATION
NEAR FIELD RADIUS (cm)	0.406	0.428
FAR-FIELD RADIUS (cm)	0.00536	0.00974
$I^{ff}(0)/E_0$ (cm^{-2})	22160	6163
<XDL>	23.73	12.46
<STREHL>	0.00206	0.00740

The results labeled <XDL> and <STREHL> are the XDL and Strehl ratio calculated for 12 intensity profiles taken without the RA. These results are used in all subsequent evaluations of the seed beam fidelity. In this manner, the seed fidelity is calculated relative to that observed without a RA or SBS phase conjugator. In a similar manner, the fidelity of the phase conjugate beam is evaluated. There was no significant difference between these results and those given above. To demonstrate that the SBS phase conjugator can compensate for reciprocal phase errors in the RA, an aberration plate was inserted between the dichroic mirror and

the quarter wave plate. This location was chosen because the plate induced such large aberrations that the seed beam would be clipped by the optics if the aberrator had been placed further away from the SBS cell focusing lens. With this aberrator, the Strehl ratio of the seed beam reflected from an ordinary mirror decreased:

**TABLE 3. Characteristics of Aberrated/
Unconjugated Multimode Seed
Beam.**

ABERRATED SEED BEAM	GAUSSIAN CALCULATION	FLAT-TOP CALCULATION
NEAR FIELD RADIUS (cm)	0.557	0.581
FAR-FIELD RADIUS (cm)	0.387	0.367
<XDL>	72.18	37.75
<STREHL>	0.00025	0.00091

When reflected from the SBS phase conjugator, the fidelity of the seed beam was much improved (see Table 4).

Comparison of the data in these three tables indicates that while the phase conjugate fidelity was not perfect, the phase conjugator was able to compensate for the most of the reciprocal phase error introduced by the aberration plate. In the discussions that follow, we observe reductions in the Strehl of <50%; we believe the SBS conjugator is capable of providing a good conjugate of beams with aberrations of this size. In addition, we investigate the change in beam fidelity as a function of gain in the RA; as a result, the observed changes in Strehl must result from nonreciprocal processes in the amplifier.

Our analysis of nonreciprocal aberrations consisted of first, evaluating the effect of Raman gain, and second, the effect of Raman gain saturation. To investigate the effects of Raman gain, we replaced the RA cell and adjusted the pump to be coincident with the conjugated seed beam. In these experiments, a seed

TABLE 4. Characteristics of Aberrated/
Conjugated Multimode Seed Beam.

CONJUGATED SEED BEAM	GAUSSIAN CALCULATION	FLAT-TOP CALCULATION
NEAR FIELD RADIUS (cm)	0.452	0.476
FAR-FIELD RADIUS (cm)	0.149	0.140
<XDL>	27.86	14.40
<STREHL>	0.00157	0.00566

pulse of ~30 mJ entered the RA on the first pass. Taking the reflection losses of the RA cell windows, the dichroic beam-splitter, the focusing lens, and the SBS cell windows, we estimate that ~17 mJ of seed energy actually entered the SBS cell. From Figure 27, the anticipated SBS reflectivity is ~15%, and, with additional system losses, we estimate that ~1.5 mJ of conjugated seed energy actually entered the RA on the second pass. Figure 31 shows the measured Raman gain (Amplified Stokes energy/Input seed energy) as a function of pump energy. At the highest gains, we estimate that ~30% of the pump energy has been depleted by the amplification process. It follows that pump depletion is a consideration in these measurements. This is also evident from the linear increase of gain with pump energy. At very low gains, pump depletion becomes less important and the gain is exponential with pump energy. Reference to the figure indicates that this is true only for pump energies <30 mJ.

Figures 32 and 33 show the results of amplified seed beam fidelity. In Figure 32, the near- and far-field seed beam radii are shown as a function of the pump energy. These beam profiles were evaluated at the RA output, and variations in the radii can be attributed to aberrations produced by the interaction of the pump and seed beams within the RA. The near-field radii,

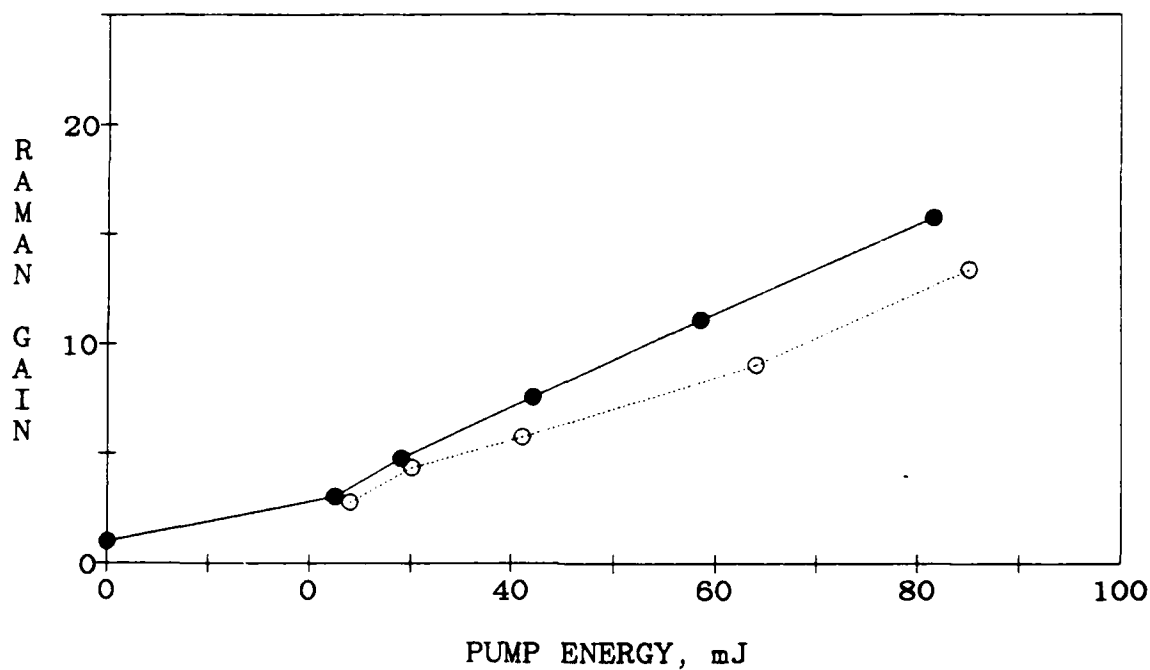


Figure 31. Measured gain in the RA as a function of the pump energy. The input seed energy is estimated to be ~ 1.5 mJ. The solid symbols are for the imaged pumping configuration; the open symbols, the diffracted pumping situation.

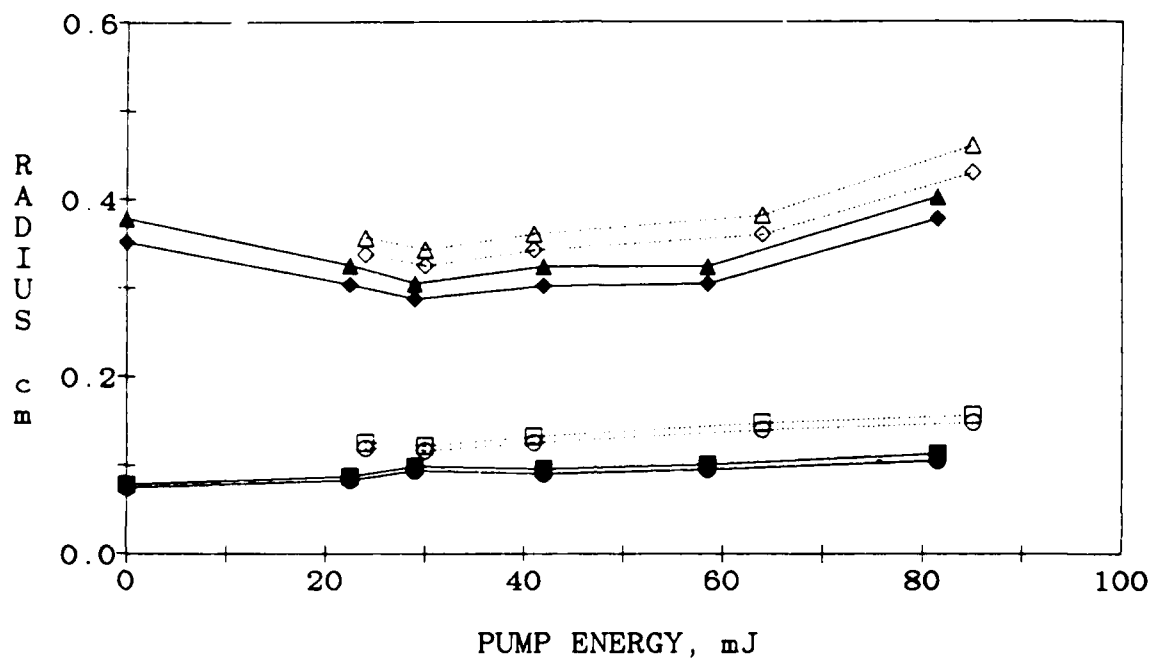


Figure 32. Seed beam radius as a function of the pump energy. The symbols correspond to those used in Figure 28.

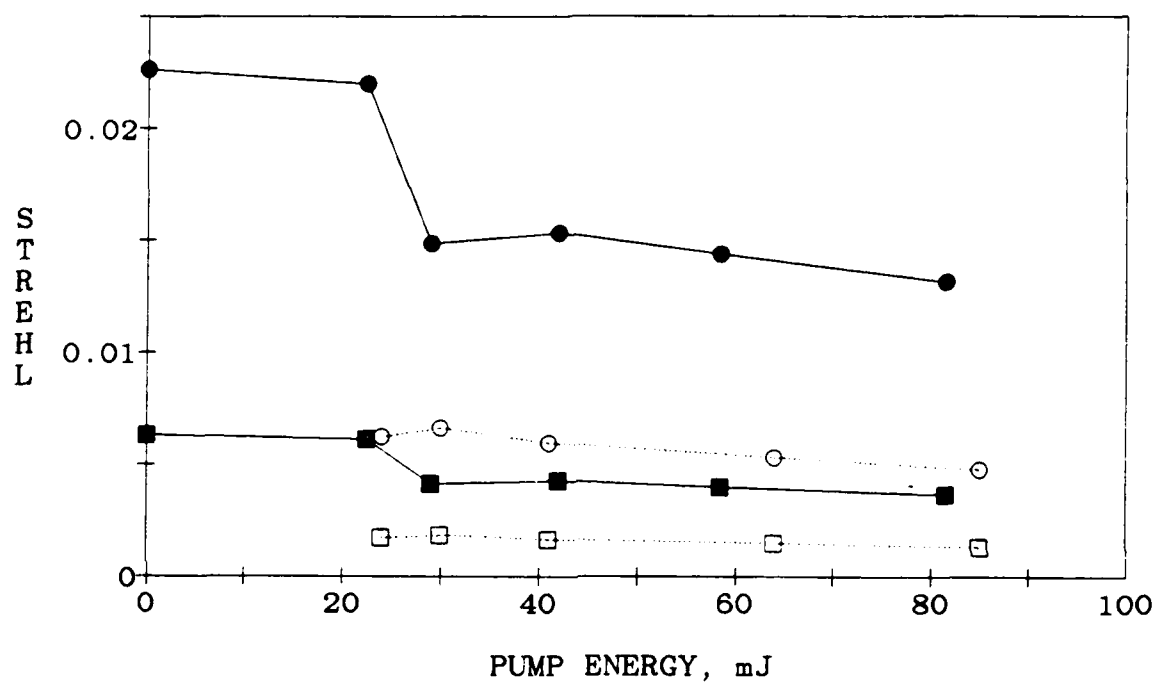


Figure 33. Strehl ratio of the amplified-conjugated seed beam as a function of the pump energy. The symbols correspond to those used in Figure 30.

indicated by the triangles and the diamonds, show an initial decrease followed by an increase. The initial decrease is thought to be a result of nonuniform gain caused by the Gaussian-like profile of the pump beam. For pump energies in excess of 30 mJ, the Raman gain begins to saturate, depleting the high intensity center of the pump beam. As a result, near-field radii increase in a manner much like that discussed in Section 2.3. The far-field radii, shown by the circles and squares, increase monotonically with pump energy.

In Figure 34, the XDL of the amplified conjugated seed beam is plotted as a function of the pump energy. As is evident from Figure 34, the XDL of the beam shows a significant (~50%) increase with Raman gain. Figure 33 shows the Strehl ratio of the amplified-conjugated seed beam. As expected, the Strehl ratio decreases with increasing pump energy. The initial strong decrease in Strehl is a result of nonuniform gain, as discussed above. At pump energies above ~30 mJ, the pump beam begins to saturate and the effects of nonuniform gain decrease. At this point, the Strehl ratio remains roughly constant with increasing energy. At the highest gains, the Strehl ratio of the amplified-conjugated seed beam (for imaged pumping condition) is roughly equivalent to that of the pump beam, because the pump and seed have similar profiles under these conditions. When the diffracted pumping condition is used, the Strehl ratios drop by nearly a factor of 2; this drop results from the different pump and seed profiles.

To investigate the effects of Raman gain saturation, we evaluated the conjugate beam fidelity as a function of seed energy. In these experiments, a constant pump pulse energy of ~40 mJ entered the RA. The seed energy entering the RA on the second pass was estimated by measuring the conjugated seed beam output without the pump beam and compensating for the system losses. Figure 35 shows the measured Raman gain as a function of seed energy. For the smallest input energy, we estimate that <1%

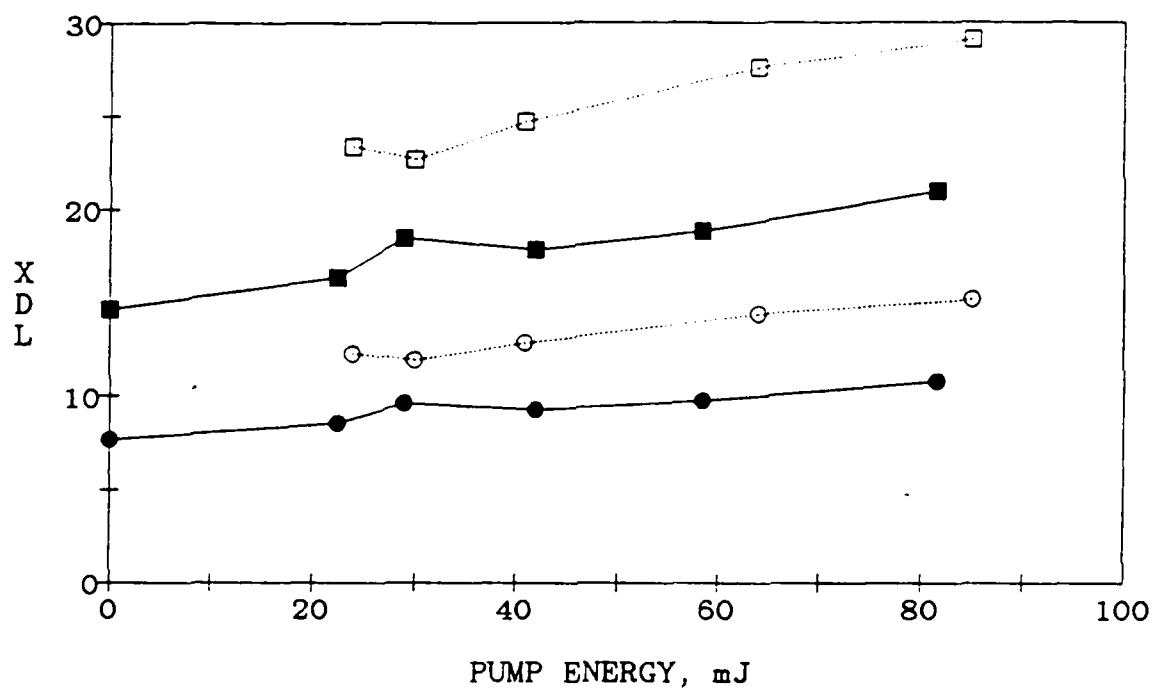


Figure 34. XDL of the amplified conjugated seed beam as a function of the pump pulse energy. The symbols correspond to those used in Figure 30.

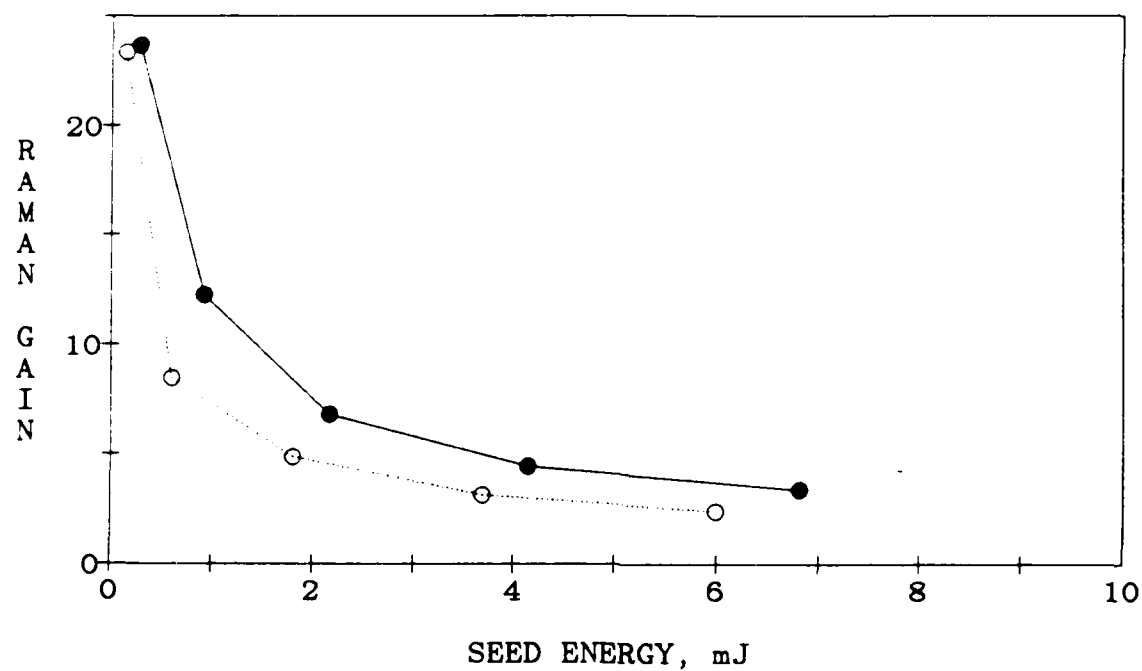


Figure 35. Measured gain in the RA as a function of seed energy entering the amplifier on the second pass. The pump energy is ~ 40 mJ. The symbols correspond to those used in Figure 31.

of the pump energy has been transferred to the seed beam, and thus pump depletion plays no role. At the highest seed energy, ~60% of the pump energy is transferred to the conjugated seed, with pump depletion playing an important role. Pump depletion effect on conjugate seed fidelity is shown in the next three figures.

In Figure 36, the near- and far-field seed beam radii are shown as a function of the seed energy. These beam profiles were evaluated at the RA output, and variations in the radii can be attributed to aberrations produced by the interaction of the pump and seed beams within the RA. The near-field radii, indicated by the triangles and the diamonds, show a gradual increase with seed energy, as a result of the amplified seed beam taking on a more flat-top-like profile because of pump depletion in the hot center of the seed. This change in profile is also indicated by a reduction in the profile index as the seed energy is increased. The far-field radii, shown by the circles and squares, also increase monotonically with pump energy.

The XDL of the amplified-conjugated seed beam is plotted as a function of the seed energy in Figure 37. As is evident from Figure 37, the XDL of the beam shows an increase as the Raman gain saturates. The observed change in XDL is smaller than that observed in Figure 34, which is probably the result of a decreased conjugation fidelity for low seed energies (reflectivity <20%, for seed energy <2 mJ). Figure 38 shows the Strehl ratio of the amplified-conjugated seed beam. As expected, the Strehl ratio decreases with increasing pump energy. The reduction in Strehl ratio shown in Figure 38 is similar to that in Figure 34, and is believed to be due to similar processes. The initial strong reduction is due to nonuniform gain, and the subsequent slow reduction is due to pump beam saturation.

In summary, we have observed a reduction in the Strehl ratio of our multimode seed beam, as a result of amplification by a multimode pump beam in a RA. At low extraction, when pump

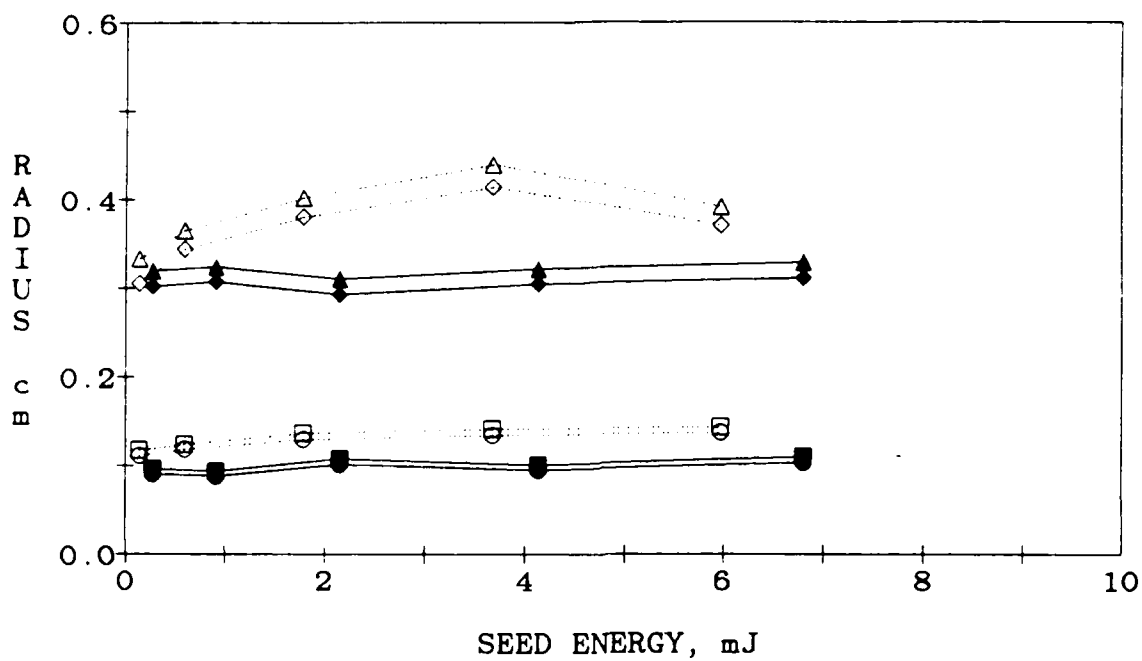


Figure 36. Seed beam radius as a function of the seed energy. The symbols correspond to those used in Figure 28.

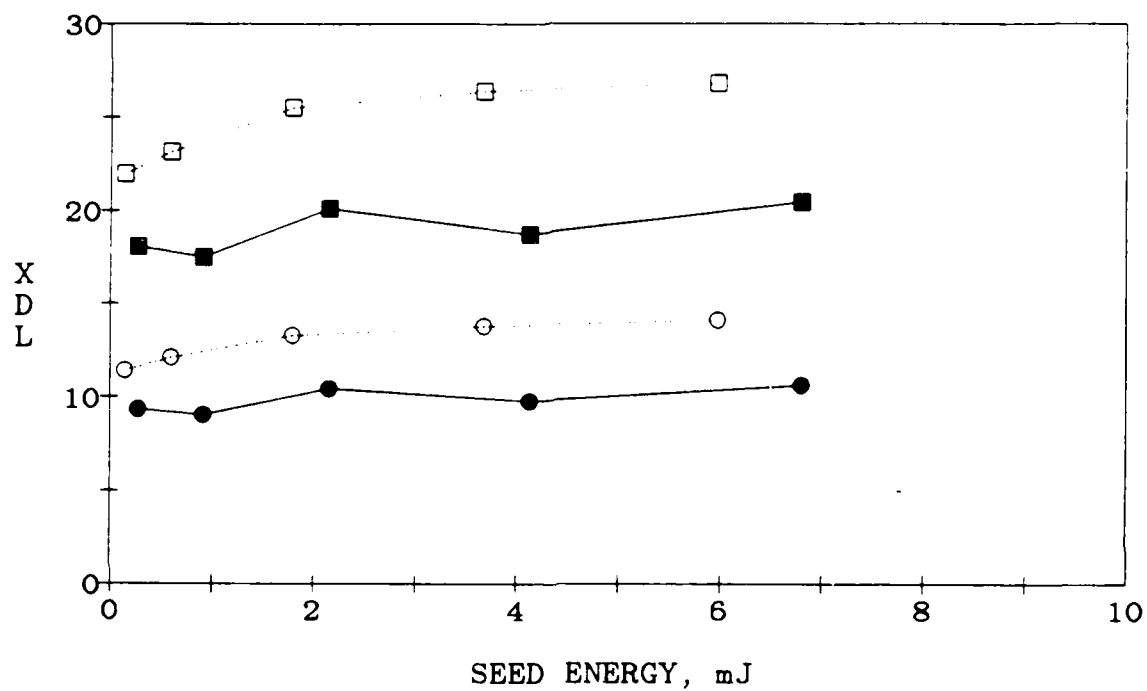


Figure 37. XDL of the amplified-conjugated seed beam as a function of the seed pulse energy. The symbols correspond to those used in Figure 29.

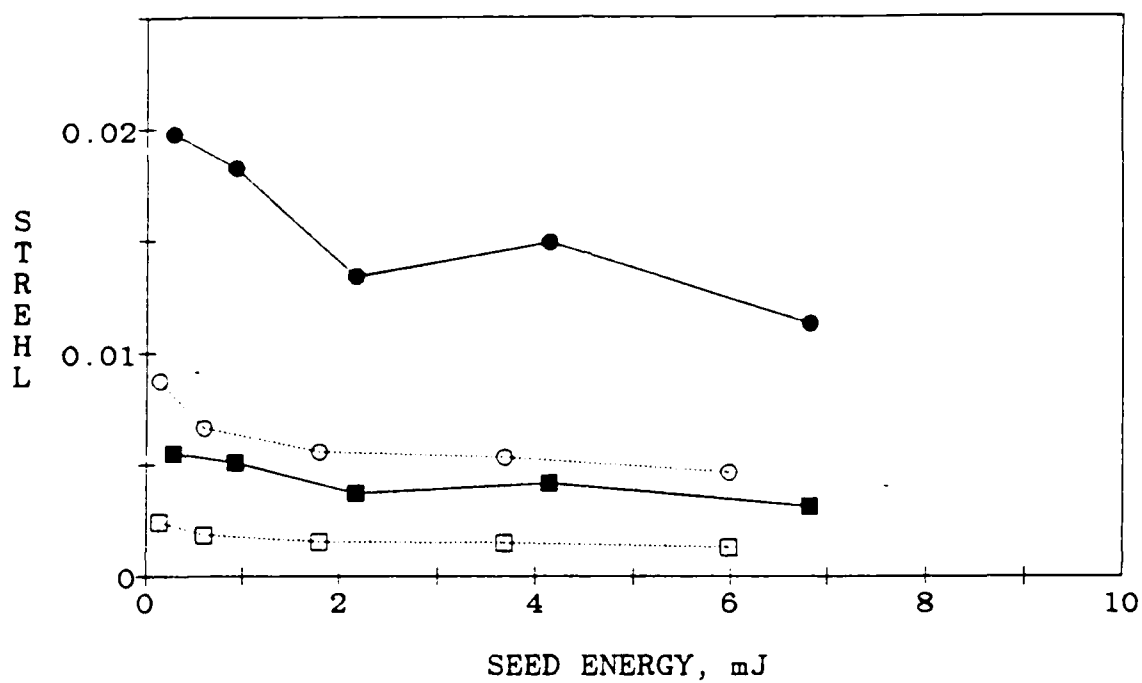


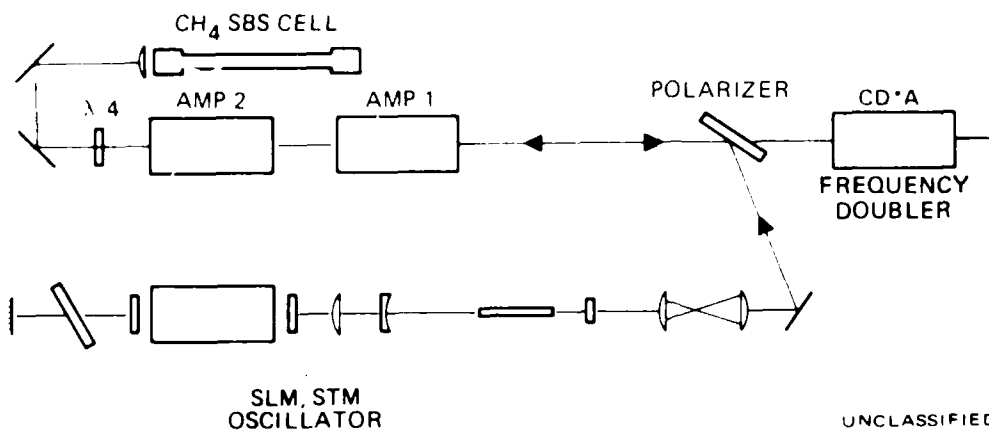
Figure 38. Strehl ratio of the amplified-conjugated seed beam as a function of the seed energy. The symbols correspond to those used in Figure 30.

depletion is not important, large decreases in the beam fidelity are observed as a result of nonuniform gain, in turn the result of a pump beam that is not strictly flat-top. As the pump becomes depleted, the seed beam begins to take on the intensity profile of the pump beam. Further reductions in amplified seed beam fidelity are not significant.

4.4 SINGLE-MODE LASER EXPERIMENTS

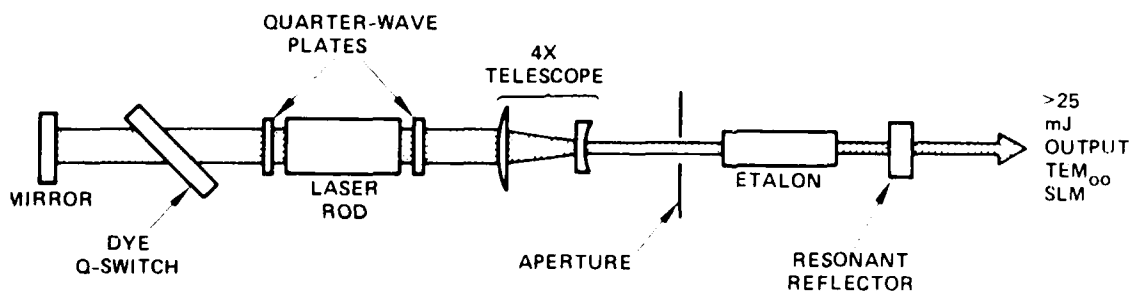
After conducting multimode experiments, we proceeded to evaluate the RA/SBS system for a diffraction-limited, single-longitudinal mode (SLM) pump laser with a 532 nm output energy of ~250 mJ. For these experiments, we were able to use a laser previously developed for another program.³² The laser consists of a commercial Nd:YAG laser modified for operation in a phase conjugate master oscillator power amplifier (MOPA) configuration as shown in Figure 39. The oscillator and amplifier heads are from a QUANTEL YG481 laser, and each contain two flashlamps and a 7-mm-diameter-by-9-cm-long Nd:YAG rod inside a BaSO₄-lined cavity. The oscillator uses a telescopic resonator design and a flowing liquid dye Q-switch, as shown in Figure 40. The oscillator output is coupled to the amplifiers by the polarizer. After undergoing a single pass through the two amplifier heads, the laser pulse is reflected by a phase conjugate mirror (PCM) that uses SBS in high pressure CH₄. The SBS "mirror" generates a retroreflected wavefront-reversed replica of the incident pulse with a reflectivity of ~80%. This replica passes back through the amplifier heads, extracting most of the remaining stored energy. The 1.064- μ m energy output is ~700 mJ. After exiting through the polarizer, the output is frequency doubled using type I doubling in a noncritically phase matched CD*A crystal. Final output is ~250 mJ at 532 nm.

The temporal pulse length of the 532 nm pulse is ~19 ns at FWHM; the pulse shape is shown in Figure 41. The beam profile is actually somewhere between a Gaussian and a flat-top, as shown in Figure 42, a plot of average intensity vs radius for the near-field of the pump beam. The pump beam was found to be SLM in



UNCLASSIFIED

Figure 39. Low energy Nd:YAG pump laser schematic. The oscillator operates in a single-longitudinal single-transverse mode.



UNCLASSIFIED

Figure 40. Single-longitudinal, single-transverse mode oscillator.

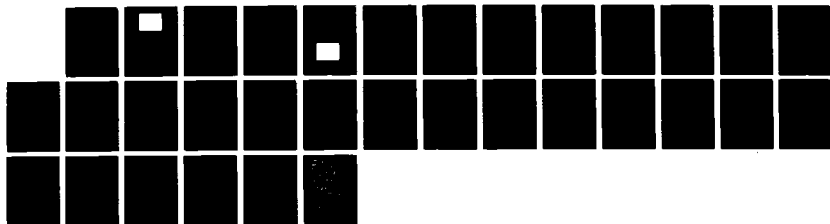
NO-A109 428

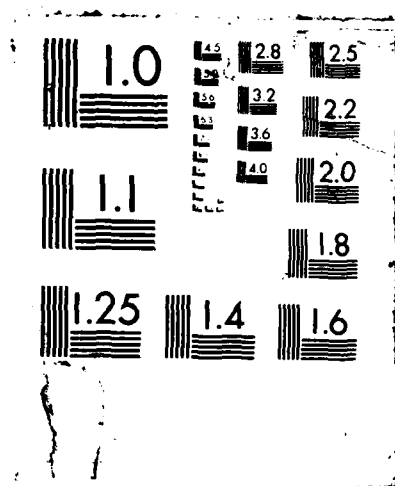
PHASE PRESERVATION CLEANUP IN A DOUBLE-PASS RAMAN
AMPLIFIER SBS (STIMULAT.. (U) HUGHES RESEARCH LABS
MALIBU CA 5 M JENSEN ET AL. 10 DEC 87 MAC-REF-00031
NO0014-85-C-0839 F/G 9/3

2/2

UNCLASSIFIED

ML





17327-22

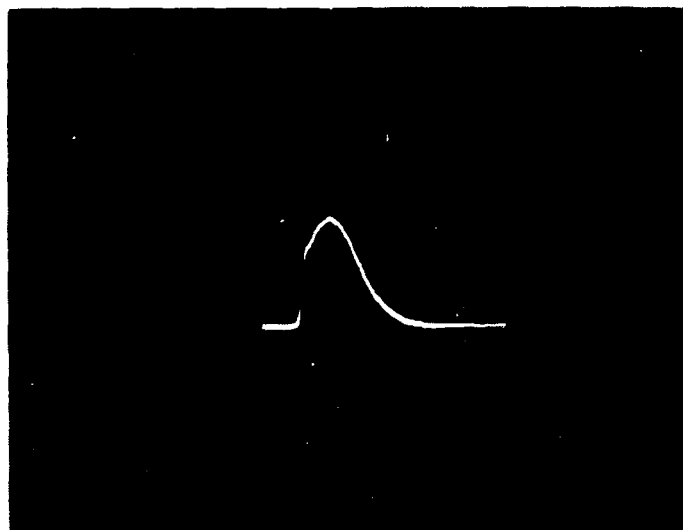


Figure 41. Temporal pulse shape of the single mode pump laser, the horizontal scale is 10 nsec/div.

17327-21

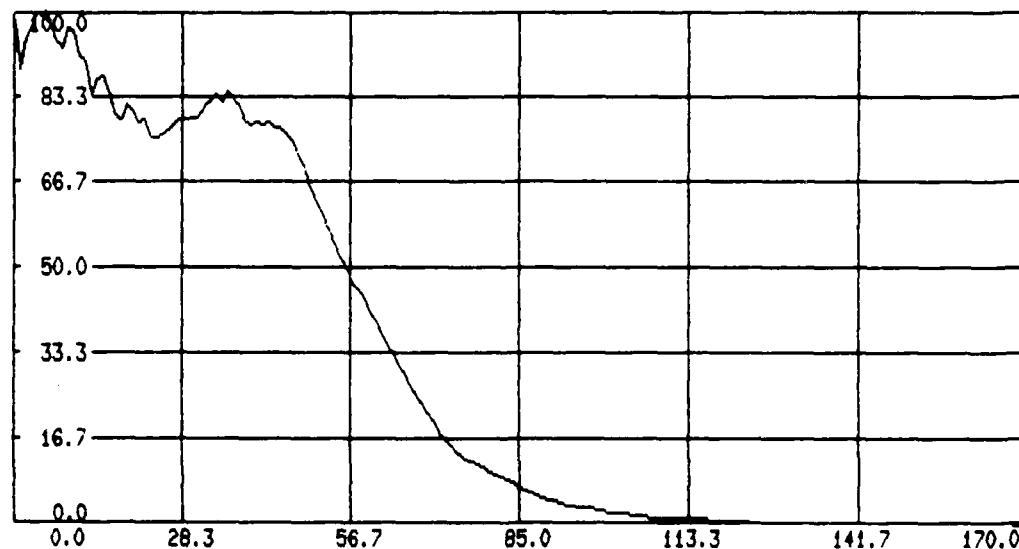


Figure 42. Average intensity vs radial position of the single-mode pump laser near-field.

approximately 85% of its pulses. The other 15% of the pulses showed modulation of the temporal shape, indicating the presence of two or more modes. The pump beam linewidth was checked, via a measurement of its coherence length (>3 m), and found to be <100 MHz. This implies a nearly transform-limited linewidth.

The experimental arrangement used in the SLM RA/SBS experiments is shown in Figure 43. Two harmonic beamsplitters are used as the first two turning mirrors to eliminate the residual $1.06\text{ }\mu\text{m}$ energy from the second harmonic. Next, a beamsplitter directs $\sim 30\%$ of the pump energy to the Raman oscillator. A long-wave-pass dichroic beamsplitter directs this pump energy through the lens into the Raman oscillator. The dichroic beamsplitter transmits the backward 1st Stokes Raman energy into a separate path that takes it through the Raman amplifier. After its first pass through the amplifier, where it picks up distortion information, the backward Stokes "seed" passes through another dichroic beamsplitter and a quarter-wave plate before entering the PCM. A phase conjugate replica of this seed proceeds back through the amplifier with a polarization orthogonal to that of the input. Because of the conjugate nature of the returning wave, reciprocal aberrations are corrected on the second pass through the amplifier. On its return path, the conjugate beam is copropagating with a pump beam of the same polarization.

Thus, the Stokes seed experiences gain and, possibly, non-reciprocal phase aberrations. After the second pass, the amplified Stokes is extracted from the original beam path by a polarizer and reaches the beam diagnostics, which include energy and beam profile measurements. Approximately 70% of the original 532 nm pump energy traveled through a delay line in order to reach the Raman amplifier at the same time the Stokes seed was making its second pass through the amplifier. Both 70% of the pump energy and of the Raman oscillator outputs are imaged to the amplifier and reduced in size in order to increase gain and extraction. This imaging of their respective apertures to the

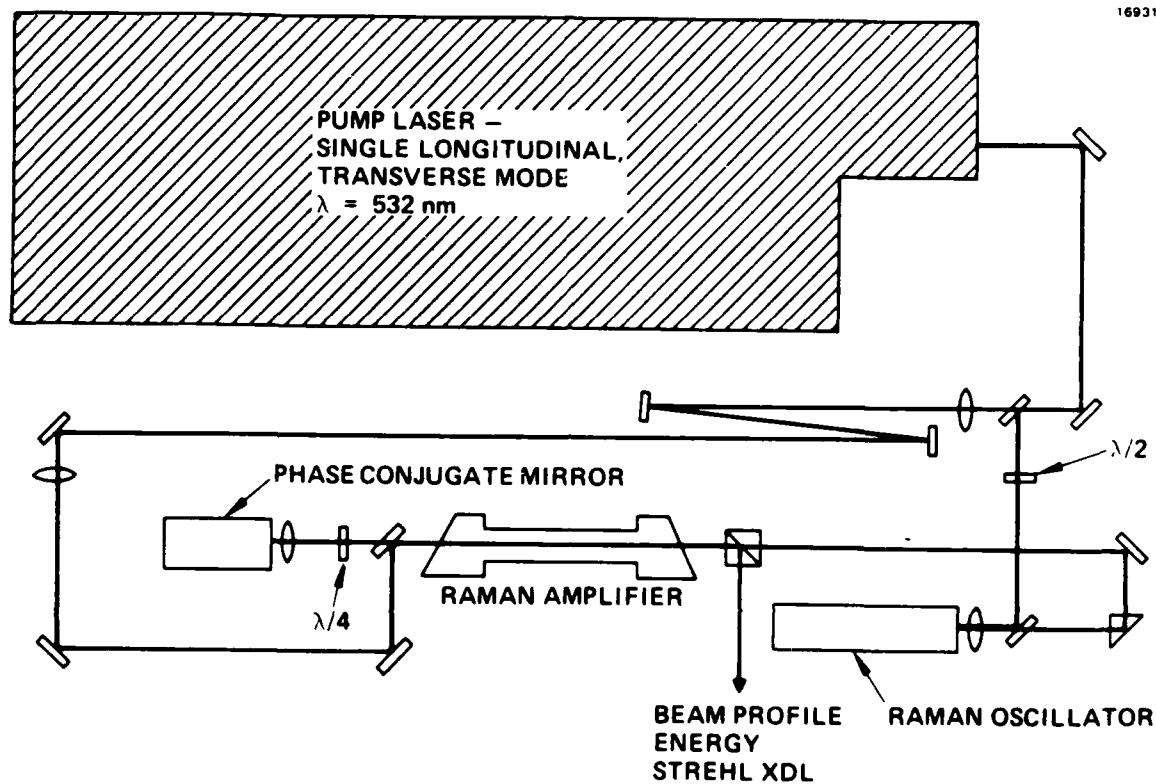


Figure 43. Experiment used to demonstrate nonreciprocal aberrations using the single-mode laser.

amplifier eliminates Fresnel diffraction until the beams are propagating through the amplifier. Note that the pump and Stokes seed beam polarizations are mutually orthogonal until the return pass of the Stokes seed through the Raman amplifier, thereby minimizing the Raman gain during the first pass. During the experiments, the pump and seed energies were varied by inserting neutral density filters into the beams.

The backward Stokes Raman oscillator was operated with an input pump energy of ~ 70 mJ ($\sim 30\times$ threshold). When seed energy was reduced, the neutral density filters were placed in the red beam only, so constant pump input to the Raman oscillator was maintained. Approximately 50% energy conversion, or 65% quantum conversion, was obtained. The temporal pulse shape of the backward Stokes seed is shown in Figure 44. Note the modulation that occurs with a period of ~ 2 to 2.5 ns. This is a typical pulse and corresponds to a pump pulse in Figure 41 that has no modulation. A coherence length measurement showed that the bandwidth of the Stokes pulse was at least three times wider than that of

17327-23

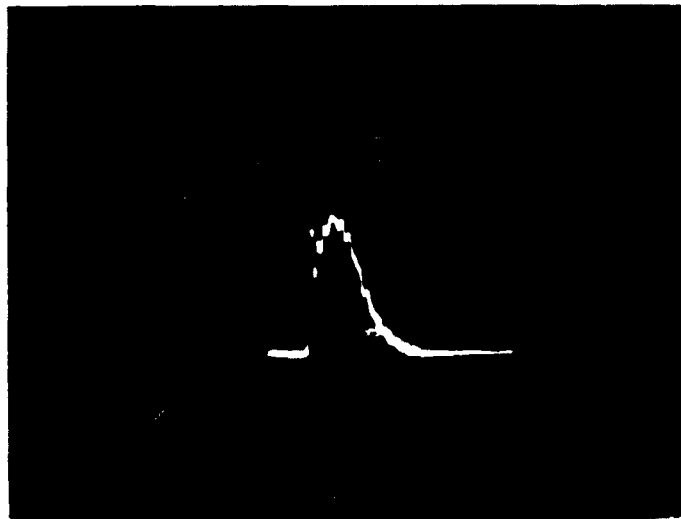


Figure 44. Temporal pulse shape of the Stokes seed.
Horizontal scale is 10 ns/division.

the pump. Nevertheless, the linewidth is less than one-third of the RA gain bandwidth.³³ It is, however, much broader than the SBS gain bandwidth in methane³⁴ (~20 MHz). We chose acetone as the SBS medium for these experiments because it has an SBS gain bandwidth of ~220 MHz.³⁵

4.5 EXPERIMENTAL RESULTS

Once the experimental arrangement was assembled, we checked for self-focusing of the pump beam in the Raman amplifier. During these experiments, the pump beam fidelity transmitted by the RA was measured as a function of pump energy. No significant change in the fidelity was observed. The pump beam quality is given in Table 5.

As can be seen from the table, the XDL and Strehl calculated using the flat-top beam assumption give erroneous results, because our pump beam has a smaller diffraction limit than a

TABLE 5. Characteristics of Single-Mode Pump Beam.

PUMP BEAM SINGLE-MODE	GAUSSIAN BEAM	FLAT-TOP BEAM
NEAR FIELD RADIUS (cm)	0.1430	0.1572
XDL	1.58	0.84
STREHL	0.54	1.78

perfect flat-top beam. In fact, the pump beam has a diffraction limit only 1.5X larger than a Gaussian beam. In what follows, we will describe RA/SBS experiments using an unaberrated pump beam, described above, and an aberrated beam. The aberrator used for these experiments was a microscope cover slip softened by flame and allowed to distort and sag over a piece of ceramic material that had small irregular bumps machined into it. After aberration, pump beam quality decreased to a Strehl of 0.026, or 14.8 XDL.

Using the unaberrated pump beam, we evaluated the small-signal gain and extraction in the Raman amplifier. A small-signal gain greater than 120, and energy extraction from the pump beam of 61% (quantum conversion of approximately 78%), were measured. This high extraction was achieved using a seed energy of 19 mJ and methane as the SBS medium. As mentioned above, we chose acetone as the SBS medium for the RA/SBS experiment because of its wider bandwidth. Acetone, however, could not withstand high seed energy (without sparking). The necessary reduction of seed energy resulted in lower extraction efficiency. Using 1.1 mJ of seed energy, energy extraction was ~22% (~28% quantum conversion) using acetone as the SBS medium.

Measurements of the SBS conjugate fidelity were made using the Stokes seed with and without an aberrator. These data are summarized in the table below:

TABLE 6. Characteristics of Single-Mode Seed Beam.

STOKES SEED	UNABERRATED XDL	UNABERRATED STREHL	ABERRATED XDL	ABERRATED STREHL
INPUT SEED BEAM	1.240 ±0.034	0.781 ±0.029	4.172 ±0.034	0.150 ±0.002
CONJUGATED SEED BEAM	1.681 ±0.046	0.582 ±0.020	2.471 ±0.078	0.554 ±0.024

From the table, it can be seen that the phase conjugate fidelity was not perfect. This could be the result of the Stokes seed linewidth being much broader than the SBS gain bandwidth. The phase conjugate fidelity of the narrower bandwidth pump laser was much better than the results given in the table above.

Having established the quality of the pump beam and the phase conjugation fidelity, we proceeded with experiments to observe nonreciprocal aberrations in the RA/SBS system. In Figure 45, we plot the measured gain of the RA for both aberrated and unaberrated beams. For an aberrated seed beam and an unaberrated pump

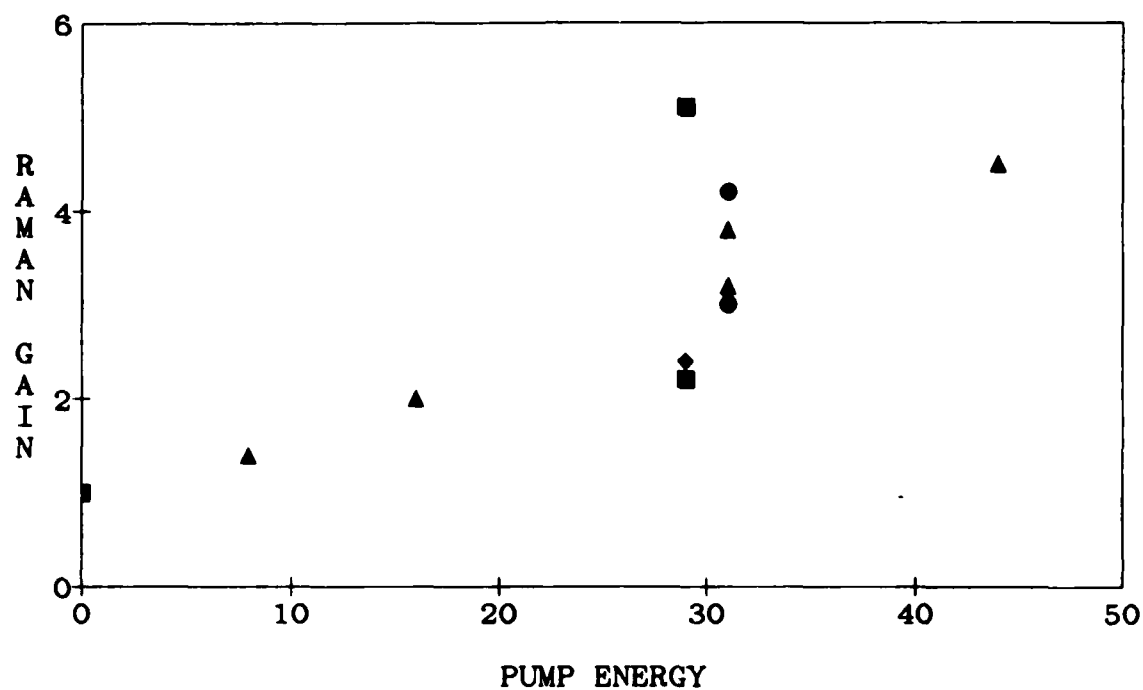


Figure 45. Raman gain as a function of the pump energy and beam aberration using the single-mode laser system. Data represented by the triangles and diamonds are for an aberrated seed beam; the squares and the diamonds represent the aberrated pump beam; otherwise the beams were unaberrated.

beam, the available data show a nearly linear increase of gain with pump energy. This indicates that saturation of the pump is playing an important role in these measurements. A least squares fit to the data shows that (at a pump energy of 30 mJ) gIL decreases from 1.47 with unaberrated beams to 0.91 with aberrated beams. In Figure 46, the XDL (Gaussian beams assumed) of the conjugated seed beam is plotted for aberrated and unaberrated beams. As expected, the XDL of the amplified seed beam increases with pump energy, because the nonuniform (Gaussian-like) pump beam profile gives higher gain to the center of the seed beam, thereby distorting the seed beam intensity profile and increasing the XDL. When the pump beam is aberrated, the unaberrated seed beam XDL is increased, as expected. If, however, the seed beam is aberrated, we find a reduction in the XDL: the reason is not known.

In Figure 47, we plot the Strehl corresponding to the XDL of Figure 46. As can be seen, the Strehl decreases monotonically with increasing pump energy; this result is consistent with Figure 46. The fact that the Strehl of the aberrated and unaberrated seed beams are nearly equal is a result of our aberration plate, which contains primarily short-scale-size aberrations. The resultant aberrated beam consists of a strong central peak with a broad plateau of scattered radiation. Consequently, the increase in XDL is much larger than the decrease of Strehl.

In the single-mode experiments described above, the RA contained a pressure of 468 psi hydrogen, while the Raman oscillator (seed generator) contained 1252 psi. This differential pressure was chosen to exactly compensate the SBS shift of acetone (4.69 GHz).^{36,37} For comparison with the simulations described in Section 2.3, we chose to vary the hydrogen pressure in the Raman oscillator. We chose not to vary the RA pressure so the Raman gain bandwidth would stay fixed at ~1.5 GHz. The oscillator pressure was varied from 1099 to 1510 psi, corresponding to a shift of -0.92 to 1.54 GHz off line-center. The measured Raman gain is plotted in Figure 48. The data show an unexpected result.

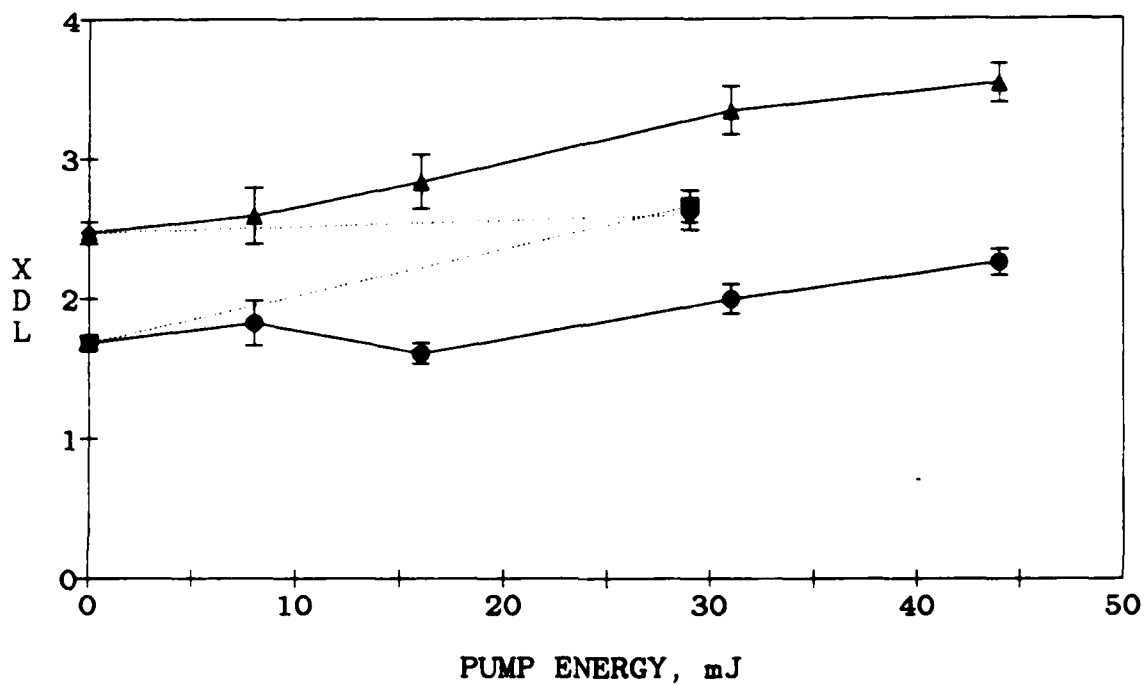


Figure 46. Conjugate beam fidelity as a function of pump energy for the single-mode RA/SBS system. The data represented by the triangles and diamonds are for an aberrated seed beam; the squares and the diamonds are for an aberrated pump beam; otherwise the beams were unaberrated.

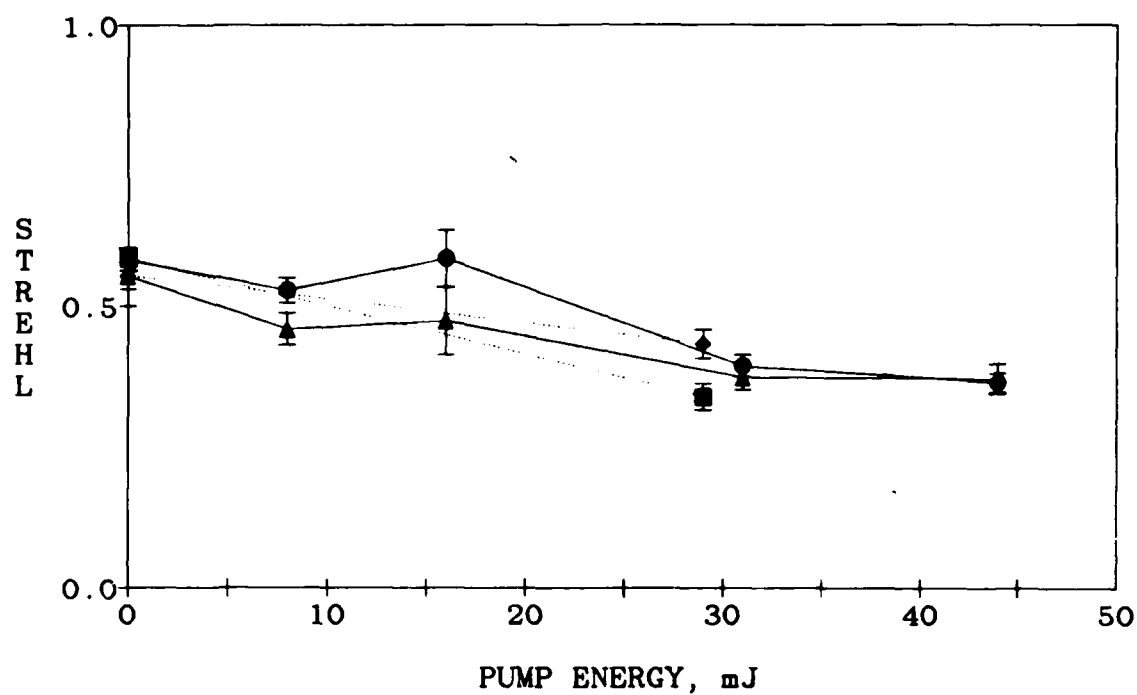


Figure 47. Conjugate beam fidelity as a function of pump energy for the single-mode RA/SBS system. The data represented by the triangles and diamonds are for an aberrated seed beam; the squares and the diamonds are for an aberrated pump beam; otherwise the beams were unaberrated.

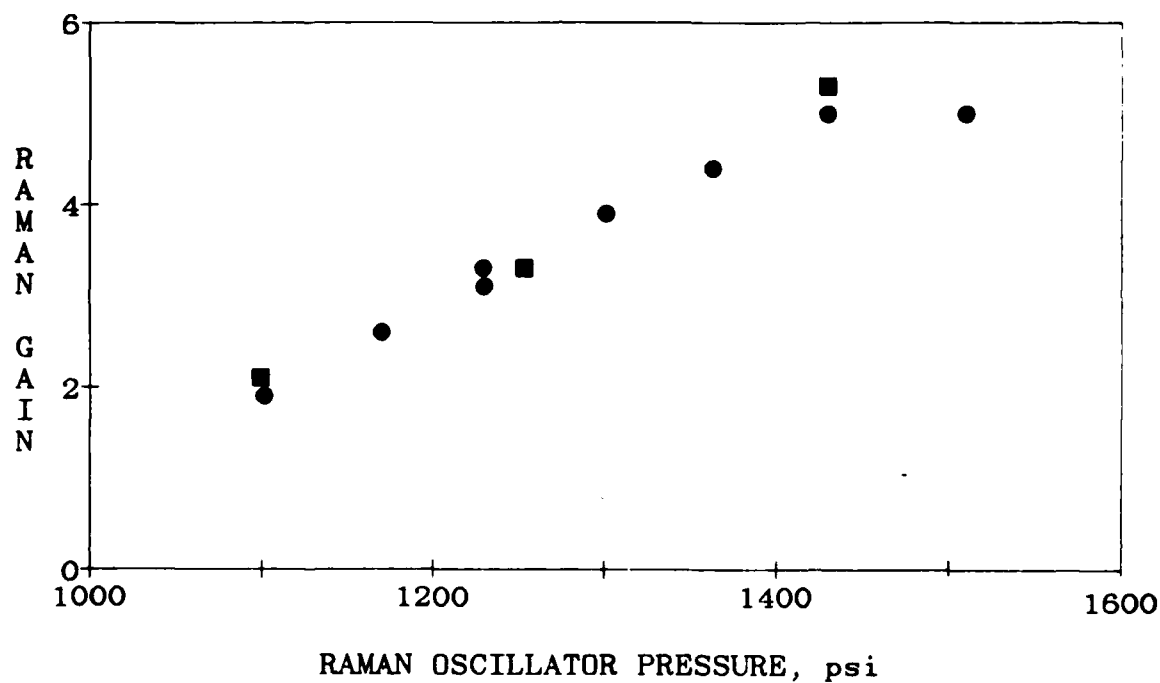


Figure 48. Raman gain as a function of the RA cell pressure using the single-mode RA/SBS system. The beams are unaberrated except for the squares, where the seed beam was aberrated.

The measured Raman gain varied linearly with the oscillator pressure. The expected result was that the gain would peak on "line center," or at about 1252 psi. Our results indicate that the maximum Raman gain occurs with an oscillator pressure of ~ 1500 psi. This corresponds to a SBS shift $\sim 1.3X$ larger than expected, or a pressure dependence of the Raman shift $\sim 0.76X$ smaller than expected. The interplay of the pump beam, seed beam, and RA linewidths could also contribute to these unexpected results. Because of time constraints, we were unable to pursue this issue further. We did, however, measure the conjugate beam fidelity as a function of the Raman oscillator pressure. These results are shown in Figures 49 and 50. In Figure 49, the conjugate beam XDL is plotted as a function of oscillator pressure, and in Figure 50 the conjugate Strehl is plotted. No significant change in conjugate beam fidelity is observed as the Raman oscillator pressure is changed.

In summary, we have assembled a RA/SBS system to evaluate nonreciprocal aberrations using a single-longitudinal/single-transverse-mode laser. The diffraction limit of the RA/SBS system was significantly better than is theoretically possible for flat-top beams, and was only $\sim 1.5X$ diffraction limited using Gaussian beam calculations. Using fixed aberrators, we demonstrated that SBS phase conjugation was capable of good compensation for large induced reciprocal aberrations. The conjugate beam fidelity was then measured as a function of the RA gain for both aberrated and unaberrated beams. We found that the amplified seed beam fidelity decreased monotonically with increasing pump energy, probably as a result of nonuniform gain resulting from the Gaussian-like intensity profile of the pump beam. Investigation of the conjugate beam fidelity as a function of frequency mismatch between the conjugate seed and the peak of the Raman gain yielded unexpected results: further investigation is needed.

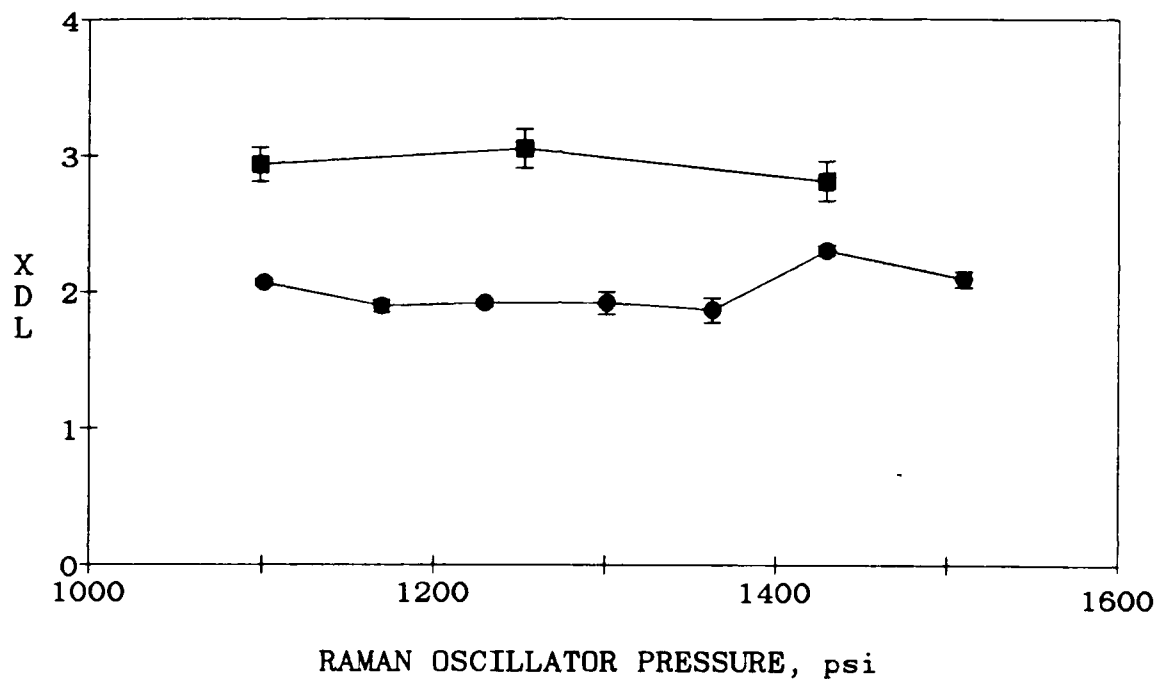


Figure 49. Conjugate beam fidelity as a function of Raman cell pressure for the single-mode RA/SBS system. The circles represent unaberrated seed beam results and the squares aberrated seed beam results. The pump beam was unaberrated in both cases.

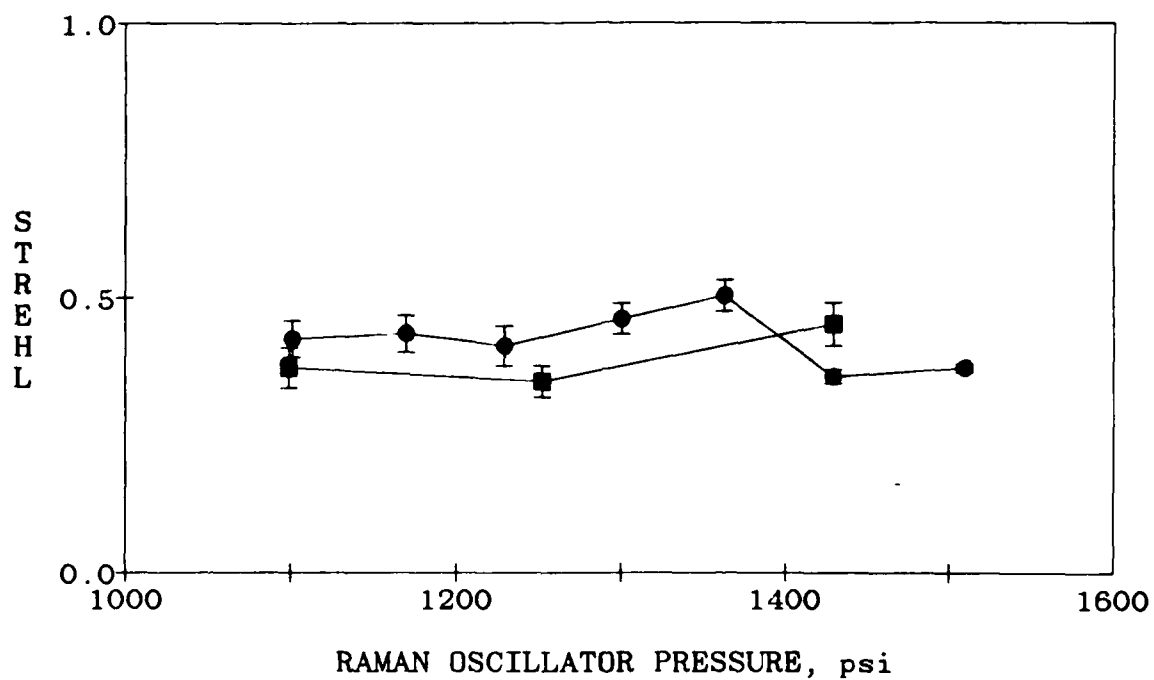


Figure 50. Conjugate beam fidelity as a function of RA pressure for the single-mode RA/SBS system. The circles represent unaberrated seed beam results and the squares the aberrated seed beam results. The pump beam was unaberrated in both cases.

SECTION 5

SUMMARY AND RECOMMENDATIONS FOR FUTURE WORK

5.1 COMPARISON OF SIMULATIONS WITH SINGLE-MODE LASER RESULTS

As discussed in Section 2, we have simulated the conjugate beam fidelity for a situation that closely corresponds to the single-mode laser data discussed in Section 4.4. These results are shown in Figures 51 and 52. In Figure 51, the calculated reduction of Strehl is plotted as a function of the small-signal gain parameter. The solid lines show the simulation results, while the open circles and squares show single-mode experimental results for an aberrated and unaberrated seed beam, respectively. The pump beam was unaberrated in both cases. As were the simulation results, the experimental results are normalized to the Strehl of the unamplified seed beam. The figure shows that our experimental results lie between the simulation of a perfect conjugator and the phase-only conjugator. This result implies that the fidelity of our SBS phase conjugator is not perfect, but also that the impact of a nonreciprocal aberration (nonuniform gain) is as strong as the simulations predict. In Figure 52, the experimental results are plotted along with the simulations of RIVED. As seen in the figure, all our experimental results lie at pump energies too small for the RIVED effect to be significant. In fact, the simulation results correspond to the reduction of Strehl at the end of the pulse, the effect being absent at the beginning. As such, the effective energy for the experimental results should be reduced by about a factor of 2 (assuming linear reduction of Strehl with cumulative energy during the pulse).

Comparison of the multimode laser results with the simulations was not done because the simulation does not take into account the broad laser bandwidth.

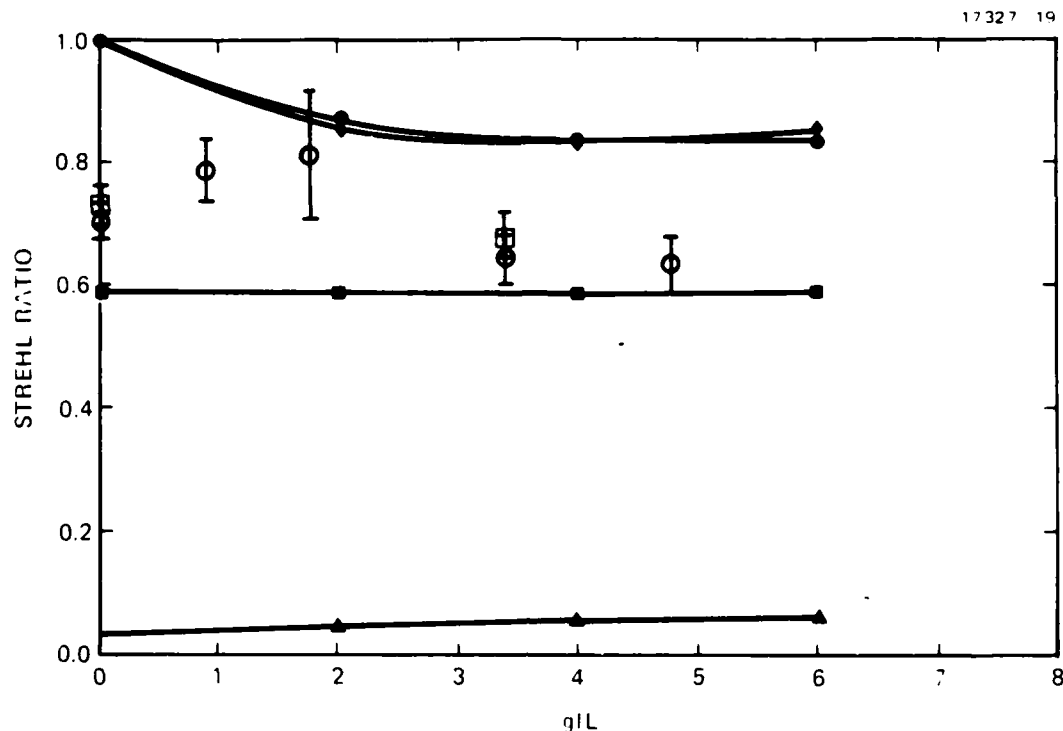


Figure 51. Comparison of simulated and experimental conjugate beam fidelity as a function of RA gain. Simulation results are represented by the solid symbols: the solid dots are for an unaberrated seed beam. The solid diamonds, squares, and triangles are for an aberrated seed beam with perfect conjugation, phase-only conjugation, and without conjugation, respectively. In all cases, the pump beam was assumed to be an unaberrated Gaussian. The open symbols show the single-mode experimental results, normalized to the seed fidelity, as were the simulations. The open circles and squares are for the aberrated and unaberrated seed beam, respectively.

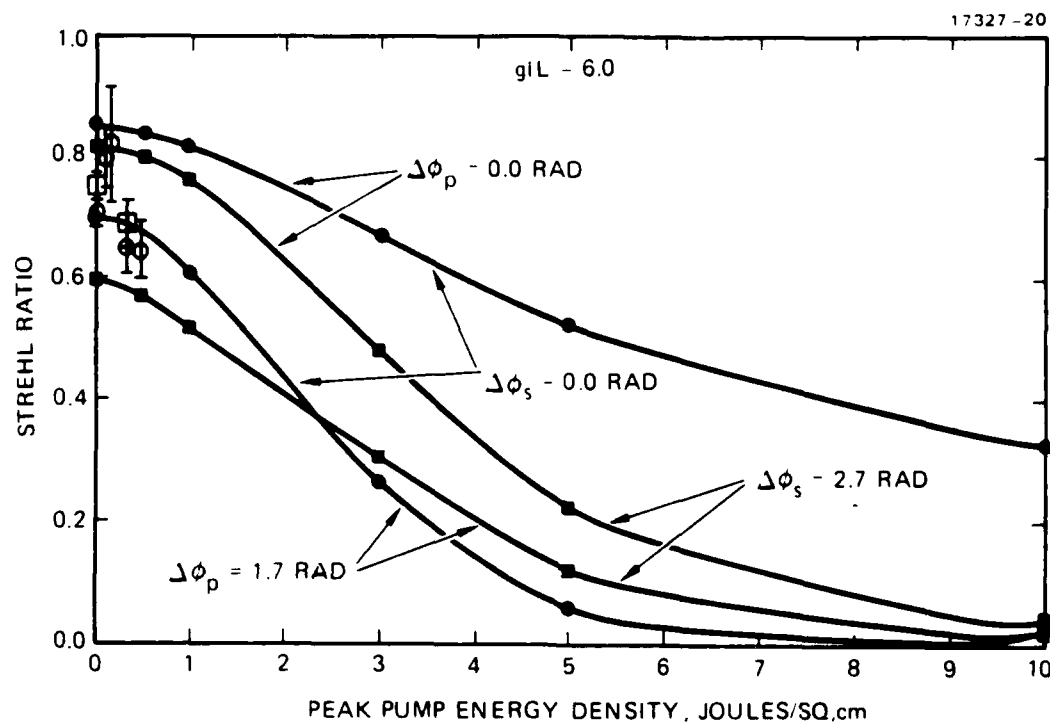


Figure 52. Comparison of experimental results with the simulation of RIVED. Simulation results are shown by the solid lines and described in the caption of Figure 16. The experimental results are shown by the open symbols and described in the caption of Figure 51.

5.2 RECOMMENDATIONS FOR FUTURE WORK

During this program, we demonstrated the reduction of beam fidelity with Raman gain in a RA/SBS system. These reductions result from nonreciprocal aberrations in the RA. Theoretical, numerical simulations and experimental results are in good qualitative agreement. Quantitative agreement between single-mode experiments and the simulations is within experimental uncertainties. The RA/SBS system shows great promise for high energy laser applications, but its implementation requires a deeper understanding of the basic device physics. Within the scope of this program we were able to demonstrate the concept, and the impact of nonreciprocal aberrations, and to identify nonreciprocal processes. The experimental implementation revealed knowledge gaps for the basic processes in the nonlinear devices. These knowledge gaps reveal clear avenues for future investigation:

- SBS phase conjugators:
 - Conjugation fidelity for wide bandwidth pump beams
 - Conjugation fidelity for highly aberrated pump beams
 - Phase vs amplitude conjugation
- Backward stimulated Raman oscillators:
 - Linewidth of generated seed
 - Dependence on pump laser bandwidth
 - Dependence on aberration on pump beam
- Raman Amplifier:
 - Reciprocal aberrations induced by thermal effects
 - Operation in high Fresnel number geometry.

In addition, simulations of transient effects, such as RIVED, are needed to correctly determine the effect of this aberration in pulsed laser systems.

REFERENCES

1. T.R. O'Meara and G.C. Valley, Optical phase conjugation applications study, Hughes Research Laboratories Final Report, published by Air Force Weapons Laboratory, AFWL-TR-82-94, January 1983.
2. T.R. O'Meara, "Compensation of laser amplifier trains with nonlinear conjugation techniques," Opt. Eng. 12, 243-251 (1982).
3. G.C. Valley and D. Fink, "Three dimensional phase conjugate resonator performance," J. Opt. Soc. Am. 73, 572 (1983).
4. R.T.V. Kung and J.H. Hammond, Visible laser technology evaluation, Vol. II- Excimer laser analysis, W.J. Schafer Assoc. Final Technical Report, WJSA 82-200, August 1982.
5. R.T. Kung, "Nonlinear index effects due to pump laser bandwidth in Raman Conversion," IEEE J. Quant. Electron. QE-18, 2056 (1982).
6. A. Flusberg et al., "The effect of weak dispersion on stimulated Raman scattering," IEEE J. Quant. Electron. QE-21 (1985).
7. W. Kolos and L. Wolniewicz, J. Chem. Phys. 46, 1426 (1966).
8. G.C. Valley and D. Fink, "Three dimensional phase conjugate resonator performance," J. Opt. Soc. Am. 73, 572 (1983).
9. J. Goldhar and J.R. Murray, "Intensity averaging and four wave mixing in RAs," IEEE J. Quant. Electron. QE-18, 389 (1982).
10. G.C. Valley and D. Fink, "Three dimensional phase conjugate resonator performance," J. Opt. Soc. Am. 73, 572 (1983).
11. A. Flusberg and D. Korff, J. Opt. Soc. Am. B4, 682 (1987).
12. G.C. Valley and D. Fink, "Three dimensional phase conjugate resonator performance," J. Opt. Soc. Am. 73, 572 (1983).
13. R.C. Lind et al., Correction of phase distortion by nonlinear optical techniques, Final Technical Report, contract No. N00014-77-C-0593, May 1981.
14. J.D. Daugherty, Avco Everett Research Laboratory, Everett, MA 02149, private communication, 1984.

15. R.T.V. Kung and J.H. Hammond, Visible laser technology evaluation, Vol. II - Excimer laser analysis, W.J. Schafer Assoc. Final Technical Report, WJSA 82-200, August 1982.
16. R.T.V. Kung and J.H. Hammond, "Phase front reproduction in Raman conversion," IEEE J. Quant. Electron. QE-18, 1306 (1982).
17. E.A. Stappaerts et al., Low distortion Raman amplification, Final Technical Report, DARPA contract No. F29601-83-C-0061, Northrop Research and Technology Center, 1985.
18. E.A. Stappaerts et al., Low distortion Raman amplification, Final Report, DARPA contract F29601-83-C-0061, Northrop Research and Technology Center, 1985.
19. N.V. Kravtsov and N.I. Naumkin, JETP Lett. 21, 257 (1975).
20. M.I. Baklushina et al., Sov. Phys. JETP 46, 436 (1977).
21. N.V. Kravtsov and N.I. Naumkin, Sov. J. Quant. Electron. 10, 519 (1980).
22. W.P. Brown, "Computer simulation of adaptive optical systems," Final Technical Report, Naval Surface Weapons Center contract No. N60921-74-C-0249, Sept. 1975.
23. A.I. Sokolovskaya et al., "Wavefront reconstruction (Conjugation) by stimulated scatterings: A review," J. Quant. Electron. QE-23, 1332-1344 (1987).
24. D.A. Rockwell and H.W. Bruesselbach, "Wavelength conversion by stimulated Raman scattering," in Physics of New Laser Sources, Ed. N.B. Abraham et al. (Plenum, New York, NY, 1985).
25. T.R. O'Meara and G.C. Valley, Optical phase conjugation applications study, Hughes Research Laboratories Final Report, published by Air Force Weapons Laboratory, AFWL-TR-82-94, January 1983.
26. T.R. O'Meara, "Compensation of laser amplifier trains with nonlinear conjugation techniques," Opt. Eng. 12, 243-251 (1982).
27. G.C. Valley and D. Fink, "Three dimensional phase conjugate resonator performance," J. Opt. Soc. Am. 73, 572 (1983).
28. B.Ya. Zel'dovich et al., Principles of Phase Conjugation, Ed. T. Tamir (Springer-Verlag, Berlin, 1985).

29. H.W. Bruesselbach and D.A. Rockwell, "Backward Stokes Raman Laser Investigation," Final Report to MK Associates, Inc., February, 1984.
30. H.W. Bruesselbach and D.A. Rockwell, "Visible and Near Infrared Laser Source," Final Report, AFWAL-TR-82-1098, 1982.
31. W.K. Bischel, at "Workshop for nonlinear optical techniques for short-wavelength lasers," Naval Research Laboratories, 1984.
32. J.O. White, H.W. Bruesselbach, M.S. Mangir, J.J. Ottusch, and D.A. Rockwell, "Tunable High Energy Raman Laser Source (THERLS)," Annual Report to U.S. Army Missile Command, Contract #DAAH01-84-C-A052, December, 1986.
33. W.K. Bischel and M.J. Dyer, "Temperature dependence of the Raman linewidth and line shift for the Q(1) and Q(0) transitions in normal and para-H₂," Phys. Rev. A 5, 3113 (1986).
34. V.I. Kovalev, V.I. Popovichev, V.V. Ragul'skii, and F.S. Faizullov, "Gain and linewidth in stimulated Brillouin scattering in gases," Sov. J. Quantum Electron. 2, 69 (1972).
35. A. Laubereau, W. Englisch, W. Kaiser, "Hypersonic absorption of liquids determined from spontaneous and stimulated Brillouin scattering," IEEE J. Quantum Electron. 5, 410 (1969).
36. A. Laubereau, W. Englisch, W. Kaiser, "Hypersonic absorption of liquids determined from spontaneous and stimulated Brillouin scattering," IEEE J. Quantum Electron. 5, 410 (1969).
37. W.K. Bischel and M.J. Dyer, "Temperature dependence of the Raman linewidth and line shift for the Q(1) and Q(0) transitions in normal and para-H₂," Phys. Rev. A 5, 3113 (1986).

APPENDIX A

PROPAGATION MODELING

The Basic Approach

The propagation phenomena associated with Raman scattering can be modeled with essentially the same techniques we have used to model the effects of turbulence and thermal blooming for propagation in the atmosphere and fields within laser resonators. The basic idea is that the effects of the medium can be approximated by a series of localized layers of gain and phase shift. The wave is propagated from one layer to the next with a free-space propagator that solves the wave equation in the paraxial approximation, which is done with a Fast Fourier Transform (FFT) algorithm. This approach is highly accurate if the distance between the layers is not too large and the wave is adequately sampled in the direction transverse to the propagation.

The principal difference between the requirements for modeling Raman scattering phenomena and for propagation modeling is the necessity in the Raman problem to include the effect of more than one field. Where all the fields are propagating in nominally the same direction (e.g., in an amplifier in which the effects of backward waves are neglected), the necessity to include more than one field impacts the modeling only by an approximately linear increase in computational time and memory requirements. No significant changes in the modeling technique are required. Where counterpropagating fields exist (e.g., in an amplifier where backward wave scattering exists), the difficulty of the modeling is significantly increased by virtue of the fact that the boundary conditions on the forward and backward waves are not given at the same location. The forward waves are specified at one end of the active medium and the backward waves at the other. We have previously explored various techniques for treating such "two-point" boundary value problems and are actively investigating new techniques under IR&D support.

The Free-Space Propagator

The propagation from one gain/phase layer to the next is calculated using a converging coordinate system. This allows us to consider cases in which the fields are strongly converging or diverging as well as collimated. The converging coordinate system is defined in terms of the convergence (or divergence) of a Gaussian beam having an e-folding radius ρ_0 , equal to one-third the diameter of the fields being propagated. With this choice of e-folding radius, the fictitious Gaussian beam has approximately 90% of its energy confined within the diameter of the propagated field. The converging coordinate variables are

$$S_1 = \frac{x}{\rho_0 P(z)} \quad (A.1)$$

$$S_2 = \frac{y}{\rho_0 P(z)} \quad (A.2)$$

$$P(z) = \alpha^{-1/2} [(1 - z/f)^2 + \alpha^2 (z/k\rho_0^2)^2]^{1/2} \quad (A.3)$$

$$\xi = \tan^{-1} \left\{ \frac{(1+\beta)z/f - 1}{\beta^{1/2}} \right\} \quad (A.4)$$

$$\beta^{1/2} = \alpha (f/k\rho_0^2) \quad (A.5)$$

$$\rho_0 = d/3, \quad (A.6)$$

where x, y, z are Cartesian coordinates with z the direction of propagation, f the distance to the focus of the converging Gaussian beam, α a parameter that allows us to consider cases in which the size of the focal spot may exceed the diffraction limit (e.g., where the initial fields are distorted), and d the diameter of the beams in the plane $z = 0$.

When expressed in terms of the converging coordinate system defined above, the free-space propagator satisfies the equation

$$\frac{\partial w}{\partial \xi} - \frac{i}{2} \left(\frac{\partial^2 w}{\partial \zeta_1^2} + \frac{\partial^2 w}{\partial \zeta_2^2} \right) + \frac{i}{2} (\zeta_1^2 + \zeta_2^2) w = 0 \quad (A.7)$$

In most applications, the increment in ξ in going from one gain/phase layer to the next is small. Thus, we approximate the solution of Eq. (A.7) by

$$w \approx \exp[-i(\zeta_1^2 + \zeta_2^2)\xi/2] \nu \quad (A.8)$$

where ν satisfies

$$\frac{\partial \nu}{\partial \xi} - \frac{i}{2} \left(\frac{\partial^2 \nu}{\partial \zeta_1^2} + \frac{\partial^2 \nu}{\partial \zeta_2^2} \right) = 0 \quad (A.9)$$

Equation (A.9) can be easily solved with a FFT routine. The solution in the transform domain is

$$V(\underline{K}, \xi + \Delta\xi) = V(\underline{K}, \xi) \exp(-iK^2\Delta\xi/2), \quad (A.10)$$

where $V(\underline{K}, \xi)$ is the Fourier transform of the field at the plane ξ . In cases where the distance between the gain/phase layers is larger, we solve Eq. (A.7) directly by expanding w in Hermite polynomials. We refer to this solution as a "Hermite propagator," and to the FFT solution as a "FFT propagator." In most cases we use the FFT propagator because it is more efficient computationally. The Hermite propagator is sometimes used in optical train calculations and in atmospheric propagation calculations in which the wave is propagated in one large step from the top of the atmospheric layer to a distant point in space. Although the Hermite propagator is available if needed, we anticipate that the FFT propagator will be used almost exclusively in the Raman modeling studies.

Sampling and Storage Requirements

The number of mesh points required in the propagation mesh depends on the highest significant spatial frequency of the variation of the complex field amplitude in the direction transverse to the propagation. Because we were interested in the effects associated with dirty pump waves, it was necessary to use a mesh having at least 128 sample points for each transverse direction (i.e., a 128 by 128 mesh for a 3-D (x,y,z) model and a 128 points mesh for a 2-D (x,z) model). Previous experience with the modeling of the distorted output of real high power laser devices has indicated that more sample points could be needed if the code is to model the effects of heavily distorted pump waves.

Having selected the number of points in the propagation mesh, we must consider the impact on the requirements for the number of steps to be taken along the direction of propagation. In order to adequately sample the fields in the transform domain, we must take enough propagation steps that the phase factor in Eq. (A.10) changes by no more than a radian or so between adjacent mesh points. The spatial wavenumber K is related to the number of mesh points N and the increment $\Delta\zeta$ in the transverse variable ζ

$$(K_x, K_y) = [(m-N/2)\Delta K, (n-N/2)\Delta K] \quad (\text{A.11})$$

$$\Delta K = 2\pi/N\Delta\zeta \quad (\text{A.12})$$

It can readily be shown that the maximum phase difference between adjacent mesh points is

$$\Delta\phi_{\max} = \frac{2\pi^2}{N} \frac{\Delta\zeta}{(\Delta\zeta)^2} \quad (\text{A.13})$$

It is immediately obvious from this relation that one must decrease the distance between the gain/phase layers when the distance between the transverse mesh points is decreased. The

increments $\Delta\zeta$, $\Delta\xi$ are related to the number of propagation steps N_{step} and the number of mesh points N_{mp} distributed across the diameter of the input beams by the relations (note that $N_{mp} < N$)

$$\Delta\zeta = \frac{3\alpha^{1/2}}{N_{mp} - 1} \quad (A.14)$$

$$\Delta\xi = \frac{\xi_f - \xi_i}{N_{step}} \quad (A.15)$$

For a case in which the active medium is 2 m long and the input waves are collimated ($f = \infty$), with $d = 0.5$ cm, $\lambda = 0.4$ μ m, $N = 128$, $N_{mp} = 89$, and $\alpha = 1$, the maximum phase shift between mesh points is

$$\Delta\phi_{max} = 0.05 N_{mp}^2 / N N_{step} = 3 / N_{step} \quad (A.16)$$

Thus, something of the order of ten propagation steps would be required to yield adequate sampling in the transform domain in this case. Of course, we must also consider the number of gain/phase layers required to approximate the continuous distribution of gain (phase shift) introduced in the real medium. Generally, the number of gain/phase layers (which is equal to $N_{step} + 1$) must be sufficient to limit the gain introduced by a single layer to unity or less.

The storage requirements are, of course, intimately tied to the sampling requirements. They also depend on whether the fields are all propagating in the same direction or not. The amount of memory available on a Cray is adequate to handle most cases of interest.

Distorted Wave Modeling

We have previously developed techniques for generating 2-D random distributions having specified spatial correlation properties. These techniques are used extensively in our adaptive optics and

propagation software to model the effects of atmospheric turbulence. The same techniques can be used to generate realizations of distorted waves in the Raman modeling studies. For example, "dirty" pump waves and replicas of atmospherically degraded waves for use in the Raman amplifier studies can be generated with these techniques. Generally, a realization of a 2-D random distribution $H(\underline{x})$ having the spatial spectrum $\phi(\underline{K})$ can be obtained from the relation

$$H(\underline{x}) = \int dS(\underline{K}) \exp(i\underline{K} \cdot \underline{x}) \quad (\text{A.17})$$

with

$$\langle dS(\underline{K}) \rangle = 0. \quad (\text{A.18})$$

$$\begin{aligned} \langle dS(\underline{K}_1) dS(\underline{K}_2) \rangle &= 0, & \underline{K}_1 \neq \underline{K}_2 \\ &= d\underline{K}_1 \phi(\underline{K}_1) & \underline{K}_1 = \underline{K}_2 \end{aligned} \quad (\text{A.19})$$

In atmospheric propagation studies we use the following modified Kolmogorov spectrum to describe the phase fluctuations associated with turbulence:

$$\phi(\underline{K}) = 0.207 C_N^2 k^2 \Delta z K_0^{-11/3} (1 + K^2/K_0^2)^{-11/6} \quad (\text{A.20})$$

We have also used the same technique to generate realizations of waves having amplitude scintillations associated with atmospheric turbulence. Dirty pump waves can be modeled by similar techniques in which the amplitude and phase variations of these waves are described by appropriate spatial spectra.

APPENDIX B

PHASE ERRORS IN RAMAN AMPLIFIERS

As an inherent part of the Raman amplification process, energy is deposited in the Raman medium in the form of vibrational excitation. This vibrational energy thermalizes and appears as heat. As is well known, a homogeneously heated gas can induce phase aberrations in an optical beam. In Raman amplifier design, a technique must be found to eliminate these thermally induced aberrations in order to permit PRF scaling while maintaining acceptable beam quality and pointing stability. In this appendix, we estimate the magnitude of the thermal phase distortion.

Consider, as a typical case, a hydrogen Raman amplifier pumped by a 5-J, 10-Hz, 525-nm beam. The first vibrational state of hydrogen has an energy $\sim 20\%$ of a green photon; hence the energy deposited in the gas is approximately 20% of the pulse energy, or ~ 1 J. Operation at 10 Hz corresponds to an average heat load in the gas of ~ 10 W. This heating induces temperature gradients that lead to density fluctuations through a variety of mechanisms, such as thermal expansion and free convection.

Temperature variations in the Raman medium may be turbulent or laminar. Laminar variations are typically larger in magnitude, and of larger spatial scale, while the turbulent fluctuations are smaller, with a small spatial scale. The phase distortions from laminar temperature variations are typically tilt, focus (or defocus), and astigmatism, while the turbulent distortions are small scale random fluctuations that can cause wide angle scattering when the beam is propagated to the far field.

Detailed thermal calculations for a typical situation have been performed. Assuming a 2-cm-diameter, 50-cm-long column of the Raman gas at 60 atm pressure is uniformly heated with 10 W, we find that the temperature profile changes from RMS

fluctuations of a few tenths of a degree in a medium with forced turbulence (i.e., with an internal fan), to a roughly parabolic profile with a peak temperature change of about 10° for a laminar medium.

Temperature changes alter the local gas density. According to the ideal gas law, $\Delta N/N = -\Delta T/T$ where N is the molecular number density and T is the temperature. The refractive index change accompanying this density change is found using the Lorentz-Lorenz equation

$$\frac{n^2 - 1}{n^2 + 3} = \frac{4\pi N}{3} \alpha \quad , \quad (B.1)$$

where n is the refractive index and α is the molecular polarizability. This equation can be expressed in a more convenient form

$$n^2 - 1 = \frac{4\pi N\alpha}{1 - (4\pi/3)N\alpha} \quad , \quad (B.2)$$

from which we find

$$\Delta n = \frac{(n-1)(n+1)(n^2+2)}{6n} \frac{\Delta N}{N} \quad . \quad (B.3)$$

Since $n \approx 1$ for gases,

$$\Delta n \approx (n-1)\Delta N/N = -(n-1)\Delta T/T \quad . \quad (B.4)$$

Using values of $(n-1)$ for hydrogen and methane yields

$$\Delta n = -8.4 \cdot 10^{-3} \Delta T/T \text{ (hydrogen)} \quad (B.5)$$

$$\Delta n = -2.6 \cdot 10^{-2} \Delta T/T \text{ (methane)} \quad , \quad (B.6)$$

where a pressure of 60 atm is assumed.

The RMS phase error σ resulting from the Δn is given by

$$\sigma^2 \sim ck^2 L L_0 \langle \Delta n^2 \rangle , \quad (B.7)$$

where c is a constant ~ 1 , $k = 2\pi/\lambda$, λ is the optical wavelength, L is the length of the medium, L_0 is the outer scale of the turbulence, and $\langle \Delta n^2 \rangle$ is the variance of the refractive index.

This expression can be derived by considering the random phase aberration $\Delta\phi$ due to a random refractive index fluctuation Δn

$$\Delta\phi = k \int_0^L dz \Delta n , \quad (B.8)$$

and finding the RMS σ by

$$\sigma^2 = \langle \Delta\phi^2 \rangle = k^2 \langle \int_0^L dz \Delta n(z) \int_0^L dz' \Delta n(z') \rangle , \quad (B.9)$$

where the brackets denote a time average. If the refractive index fluctuations have an exponential correlation function of the form

$$\langle \Delta n(z) \Delta n(z') \rangle = \langle \Delta n^2 \rangle \exp(-|z-z_0|/L_0) , \quad (B.10)$$

then

$$\sigma^2 \simeq 2k^2 L L_0 \langle \Delta n^2 \rangle . \quad (B.11)$$

Other correlation functions give the same functional dependence and numerical coefficients ranging from $\pi/4$ to $\pi/2$.³⁸ The phase error can now be calculated by substituting Eqs. (B.5)

³⁸L.A. Chernov, Wave Propagation in a Random Medium (Dover, NY, 1967), 75.

and (B.6) into (B.11), and using $L = 50$ cm, $L_o = 0.3$ cm (the outer scale is typically $\sim 0.1X$ the tube diameter, assumed to be ~ 2 cm). Considering first the laminar case, we calculated $\Delta T \sim 10^\circ K$, and

$$\sigma = 150 \text{ rad (hydrogen)} \quad (B.12)$$

$$\sigma = 470 \text{ rad (methane)} \quad (B.13)$$

For the turbulent case, ΔT was found to be $\sim 0.1^\circ K$, and the resulting phase errors are smaller than the above values by a factor of 100.

END
DATE
FILMED
MARCH
1988
DTIC